

Institut für Festkörperphysik

FRIEDRICH-SCHILLER-UNIVERSITÄT JENA



Annual Report 2009

Institut für Festkörperphysik

Friedrich-Schiller-Universität Jena

Annual Report 2009



Editors: Prof. Dr. Carsten Ronning
Uta Bornkessel

**Institut für Festkörperphysik
Friedrich-Schiller-Universität Jena
Max-Wien-Platz 1
D-07743 JENA**

Tel.: +49 (0) 3641 / 947300
Fax: +49 (0) 3641 / 947302
e-mail: carsten.ronning@uni-jena.de
home page: <http://www.ifk.uni-jena.de/>

Prof. Dr. Carsten Ronning
director
Tel.: +49 (0) 3641 / 947300, 947301
Fax: +49 (0) 3641 / 947302
e-mail: carsten.ronning@uni-jena.de
home page: <http://www.nano.uni-jena.de/>

Prof. Dr. Torsten Fritz
Tel.: +49 (0) 3641 / 947400, 947411
Fax: +49 (0) 3641 / 947412
e-mail: torsten.fritz@uni-jena.de
home page: <http://www.physik.uni-jena.de/~layer/>

Prof. Dr. Friedrich Huisken
Tel.: +49 (0) 3641 / 947354, 947301
Fax: +49 (0) 3641 / 947308
e-mail: friedrich.huisken@uni-jena.de
home page: <http://www.astrolab.uni-jena.de/>

PD Dr. Heinrich Metzner
Tel.: +49(0) 3641 / 947353
Fax: +49(0) 3641 / 947302
e-mail: heiner.metzner@uni-jena.de
home page: <http://www.physik.uni-jena.de/inst/exphys/>

Prof. Dr. Paul Seidel
Tel.: +49 (0) 3641 / 947410, 947411
Fax: +49 (0) 3641 / 947412
e-mail: paul.seidel@uni-jena.de
home page: <http://www.physik.uni-jena.de/~tief>

Prof. Dr. Werner Wesch
Tel.: +49 (0) 3641 / 947330, 947301
Fax: +49 (0) 3641 / 947302
e-mail: werner.wesch@uni-jena.de
home page: <http://www.physik.uni-jena.de/~exphys/>

Preface

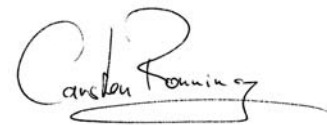
We like to take this annual report 2009 as an opportunity to thank a lot of people and organizations for their manifold support for our research at the Institute of Solid-State Physics at the Friedrich-Schiller-University Jena. Furthermore, this report, which is already the 14th in this series, is also addressed to the interested scientific community and to our colleagues within the university and from outside.

Special thanks go to the following organizations for their financial support:

- Deutsche Forschungsgemeinschaft – DFG
- Bundesministerium für Bildung und Forschung – BMBF
- Bundesministerium für Umwelt, Naturschutz und Reaktorsicherheit – BMU
- Bundesministerium für Wirtschaft und Technologie – BMWi
- Thüringer Ministerium für Bildung, Wissenschaft und Kultur – TMBWK
- Deutscher Akademischer Austauschdienst – DAAD
- Gesellschaft für Schwerionenforschung, Darmstadt – GSI
- Deutsches Elektron Synchrotron, Hamburg – DESY
- Several Industrial Partners

We like also to thank all our colleagues at other Universities and Institutes, which are collaborating with us, but the collaborative work has not been presented in the research articles of this report. Furthermore, we are very grateful for the work of our very motivated secretaries, technicians and the people in the mechanical and electrical workshops. All have contributed to our research in an outstanding way and, thus, to this report.

At this point, we like to mention only one highlight of 2009: we are very glad that Prof. Dr. Torsten Fritz from the Technical University of Dresden accepted the offer to take over a chair position in our Institute. He started his work in the “yellow House” in November 2009, and we all like to welcome him and wish him all the best in our solid-state community.

A handwritten signature in black ink, appearing to read 'Carsten Ronning', with a stylized flourish at the end.

Prof. Dr. Carsten Ronning

Contents

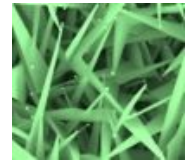
1. Departments of the institute	6
2. Scientific reports	
MD simulation of defect accumulation and amorphization in AlGaAs	12
Structural modification of swift heavy ion irradiated amorphous germanium layers	14
Structural modification of low temperature swift heavy ion irradiated amorphous germanium layers	16
Stress and plastic flow in germanium during amorphization by ion bombardment	17
Ultrathin membranes in x-cut lithium niobate	18
Photonic crystals in lithium niobate by ion-beam enhanced etching	19
Study of iodine diffusion in silicon carbide	20
Temperature dependence of damage formation in Ag ion irradiated SiC	22
New UV-VIS and FTIR spectrometer at the IFK	24
Cadmium Sulfide Nanowires: Growth	25
Cadmium Sulfide Nanowires: Lasing	26
Ion beam induced nanoscaled surface structures on TiO ₂	28
Biofunctionalization of ZnO nanowires and silicon nanoripples	30
Carbon-assisted growth and characterization of aligned ZnO-nanowires	32
Spatial resolved cathodoluminescence on semiconductor nanostructures	34
Four tip measurement station Süss EP6 DC	36
Photoluminescence investigations on polycrystalline cadmium telluride solar cells	38
Design of a high vacuum chamber for cadmium telluride evaporation and doping	40
Implementation of a new rapid thermal annealing furnace	42
Selenium vapour flux control by measuring the selenium beam equivalent pressure	44
Wide-band phase locking of intrinsic Josephson junctions in a resonator	46
Preparation and investigation of epitaxially grown CaRuO ₃ / SrTiO ₃ / CaRuO ₃ – structures	48
Nanocrystalline ferromagnetic materials at low temperatures and their use in a superconducting beam monitor	50
Size distribution and crystallographic properties of self-assembled gold nano particles in YBa ₂ Cu ₃ O _{7-δ} thin films	52
Numerical calculation of thermoelastic damping of vibrating bulk samples	54
Rotation course characterisation of air turbine for improvement of an HTSC-MRX system for measurement of Néel relaxation of superparamagnetic nanoparticles.....	56
Cryogenic Q-factor measurements on high purity silicon bulk material	58
Electrical transport in thin film iron pnictide junctions	60
Measurements of insulating structures for growth of carbon nanotubes	62

Electronic spectroscopy of polycyclic aromatic hydrocarbons isolated in solid neon	64
Oxidation Reactions in Helium Droplets at $T = 0.37$ K	66
X-ray photoelectron diffraction: A tool for the structure analysis of ultra-thin epitaxial layers	68
Optical differential reflectance spectroscopy of ultrathin epitaxial organic films	70
Line-on-line organic-organic heteroepitaxy of QT on HBC on Au(111)	72
3. Technical reports and equipment	
Operation of the ion-accelerators JULIA and the ion-implanter ROMEO	74
Cryogenic service	76
Equipment	77
4. Current research projects	80
5. Publications	
5.1 Publications in scientific journals	82
5.2 Invited talks and colloquia	87
5.3 Conference contributions	88
5.4 Theses	93
6. Cooperations, guests and colloquia at IFK	
6.1 Visiting scientists	96
6.2 Colloquia at Institute of Solid State Physics	96
7. Teaching activities	
7.1 Lectures	98
7.2 Seminars	98
7.3 Practica	99
8. Personnel	100

Departments of the institute

Experimental Physics / Solid State Physics

Prof. Dr. C. Ronning



- Synthesis, doping and functionalization of semiconductor nanowires
- Semiconductor physics: doping using ion beams
- Growth and functionalization of diamond-like materials
- Ion beam analysis

Recent work of the research group in the field of semiconductor nanowires focuses both on the growth of desired nanostructures as well as on the modification of semiconductor nanowires for the use as photonic and electronic devices. This includes in realization of light-emitting diodes and the observation of laser oscillations within single ZnO nanowires. The latter results have been realized in collaboration with the group of Prof. Dr. F. Capasso from the Harvard University – an fruitful exchange collaboration, which has been supported by DAAD in 2009.

In the area of semiconductor nanowires the group holds further successful collaborations within the SPP-Program “Nanowires and Nanotubes” of the DFG. This includes PL-investigations of H-treated single ZnO nanowires together with Dr. T. Voss (Uni Bremen), life-time measurements of ZnS:Mn nanostructures with Prof. Dr. W. Heimbrodt (Uni Marburg), the electrical doping of III-V-nanowires with Dr. W. Prost (Uni Duisburg), as well as the growth of desired nanostructures together with Prof. Dr. R. Adelung (Uni Kiel).

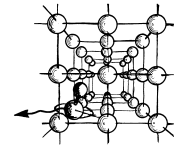
Besides those supported collaborations by funding agencies, the group works also on the electrical functionalization of Si nanowires for different kind of memory devices or solar cells together with Dr. A. Colli / Prof. Dr. A. Ferrari (University of Cambridge, UK) and PD Dr. S. Christiansen (IPHT Jena)

In the past year the group has successfully rebuild the equipment, which has been moved from Göttingen to Jena in 2008. Now the accelerator system Mr. JIM Stringer is used for the growth of diamond-like materials and their surface treatment. The biocompatibility and bioactivity of such thin films and the influence of both the structure and chemistry of the surface is currently investigated.

Finally, it is worth to mention that the group also on-going work in the area of ion beam doping of ZnO (in collaboration with Prof. Dr. M. Grundmann, Uni Leipzig), the ion beam analysis of thin high- k materials (Dr. C. Wenger, IHP Frankfurt/Oder), the SiN passivation films for solar cells (CIS Erfurt), an RBS-investigations of BN thin films (Prof. Dr. H.G. Boyen, Uni Hasselt).

Ion Beam Physics

Prof. Dr. W. Wesch



- Modification of solids by ion implantation and succeeding processes and ion beam analysis (RBS, PIXE, ERD, NRA)
- Ion beam synthesis of buried nanostructures
- Investigation of the effect of high electronic excitation on structural modification of crystalline and amorphous semiconductors
- Simulation of processes of ion-solid interaction

The *Ion Beam Physics* Group deals with problems of modification of solids and synthesis of buried nanostructures by means of ion beams and combined secondary processes. The studies cover fundamental processes of ion-beam induced structural modification in new semiconductors and insulators being relevant for future electronic, optoelectronic and photonic device technologies, as e.g. ternary III-V semiconductors, wide gap semiconductors and insulators (collaborations with the Australian National University Canberra, the University of Pretoria, South Africa and the University Lisboa, Portugal). The structural changes in Al-GaAs, Si and Ge caused by ion irradiation are also investigated by classical molecular dynamics computer simulations. At the same time the formation of ferromagnetic nanocrystals and layers in Si and GaAs by ion-beam induced non-equilibrium processes (collaboration with the University Aveiro, Portugal) and the specific modification of optical materials as LiNbO₃ and KTiOPO₄ as well as ion beam enhanced chemical etching to produce high aspect ratio microstructures for optical application of these materials (collaboration with the Institute of Applied Physics, Jena) are studied.

Beside these activities on materials modification utilizing ion beams with conventional energies (several 10 keV to several MeV), the effect of high electronic excitation under swift heavy ion irradiation (several 100 MeV) on structural modification of crystalline semiconductors (ion track formation) as well as on plastic deformation in amorphous semiconductors is studied in collaboration with the Australian National University Canberra (supported by the DAAD and the Australian Research Council).

Low Temperature Physics



Prof. Dr. P. Seidel

- Superconductivity within thin layers and layer systems
- Josephson effects, proximity effect, tunnel effects and quantum effects in superconducting devices
- DC-SQUID's and their application in measurement, e.g. biomagnetism, NDE, MRX
- cryogenic measurements on optical components (mechanical quality factor)
- Dynamics of superconducting Josephson arrays and qubits
- cryogenic engineering (cryocoolers, cryogenic storage)

The *low temperature physics* group works on the following fields:

- preparation, characterization, modelling and application of Josephson junctions and SQUIDs (precision and magnetorelaxation measurements with LTS SQUIDs, non-destructive evaluation and biomagnetism with HTS SQUIDs, intrinsic Josephson junctions)
- low temperature physics and cryogenic engineering (development of new kinds of pulse tube cryocoolers, investigations on a new concept for regenerators, cryogenic storage)
- experimental work within the SFB/TR on cryogenic measurements of the Q-factor of optical components including grating optics
- thin film technologies for insulators and other materials

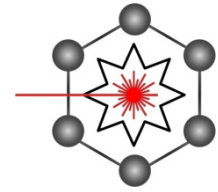
The research is carried out in cooperations with other research groups in Thuringia (TU Ilmenau, IPHT Jena, SQUID GmbH Jena, SUPRACON Jena, Polyoptik Bad Blankenburg, Innovent e.V. Jena). Within common activities the group works together with the Gesellschaft für Schwerionenforschung Darmstadt, DESY Hamburg, TARGET Systemelectronic GmbH Solingen and the Zentrum für Raumfahrttechnologie und Mikrogravitation Bremen.

With industrial partners there exist some research activities e.g. with Air Liquide (France), Northrop Gruman (USA), AEG Infrared Moduls GmbH Heilbronn and the TransMIT center for adaptive cryotechniques Gießen. A long tradition of cooperation exists with the Institute of Electrical Engineering (IEE) of the Slovak Academy of Sciences Bratislava, the Universities of Moscow (Russia), Kharkov (Ukraine), Glasgow (U.K.) and Vienna (Austria), the Tohoku University Sendai and the University of Osaka (both in Japan).

Laboratory Astrophysics/Cluster Physics

Prof. Dr. F. Huisken

- Photoluminescence studies of silicon and germanium nanocrystals produced by CO₂ laser pyrolysis
- Cavity ring-down spectroscopy of neutral and ionized polycyclic aromatic hydrocarbons (PAHs) in supersonic jets
- Study of astrochemical reactions in liquid helium nanodroplets

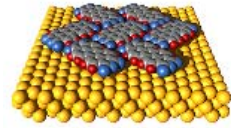


The Joint *Laboratory Astrophysics/Cluster Physics* Group at the Institute of Solid State Physics results from a cooperation between the Max-Planck-Institute for Astronomy, Heidelberg, and the Friedrich-Schiller-University, Jena. Inaugurated in February 2003, it is conducted by Prof. Dr. Thomas Henning and Prof. Dr. Friedrich Huisken.

The research of the Joint Laboratory Astrophysics and Cluster Physics Group is devoted to fundamental astrophysical questions that can be answered by laboratory experiments, with particular emphasis on spectroscopy. The electromagnetic radiation reaching us from stellar objects is modified in a characteristic manner by interstellar molecules and dust particles. Many of these “fingerprints” are still far from being understood. In order to determine the species causing the modification of the electromagnetic signals detected by telescopes and satellites, comprehensive laboratory studies are urgently needed.

The laboratory is equipped with modern molecular and cluster beam machines as well as laser systems to contribute to the clarification of such fundamental questions. For this purpose, the molecules, clusters, and nanoparticles of interest are prepared in vacuum chambers under conditions coming close to those encountered in the interstellar space (low temperature and low density).

Applied Physics / Solid State Physics



Prof. Dr. T. Fritz

- Preparation of highly ordered thin films of organic molecules by UHV-deposition (OMBE)
- Chemical vapor deposition and characterization of carbon nanotubes
- Growth of graphene and carbon nanotubes on silicon carbide
- *In situ* optical spectroscopy (DRS)
- Analyses of surfaces, layers and nanostructures using AES, XPS, LEED, RHEED, XPD, STM, AFM, and SEM

The group *Applied Physics / Solid State Physics* (formerly known as *Physics of thin films*-group) at the Institute of Solid State Physics is engaged in the research on nanostructures, solid surfaces and thin films of both organic and inorganic semiconductor materials.

Our main research interest lies in the discovery of structure-property-relations of structurally well defined ultrathin epitaxial layers, organic quantum wells and carbon nanotubes. The main target of our research is the development of basic principles for the use of nano materials in prospective devices.

For analyses of the chemical composition and bonding at surfaces and in thin films we use surface analysis methods like photoelectron spectroscopy (XPS, UPS) and Auger electron spectroscopy (AES). The crystalline structure can be determined by electron diffraction (LEED, XPD, and electron channeling). Scanning tunneling microscopy (STM), atomic force microscopy (AFM) and scanning electron microscopy (SEM) are used for high-resolution imaging of nanostructures and surfaces.

Our *in situ* optical spectroscopy, namely differential reflectance spectroscopy (DRS) is used to study organic (sub-)monolayers and heterostructures in terms of absorption spectroscopy to analyse the optical interaction between the molecules or between organic adsorbates and inorganic substrates.

We have also developed a computational method to calculate the inter- and intralayer potential energy and to predict epitaxial alignments for realistically large OMBE domains (comprising several thousands of molecules).

Carbon nanotubes have been produced on solid substrates by chemical vapour deposition (CVD) using methane and ethanol as precursor gas. Extensive characterization of the CVD samples by SEM, AFM and Raman spectroscopy revealed high-quality single-wall carbon nanotubes of diameters between 1 and 2 nm. The amount of residual catalyst and amorphous carbon species has been determined to be very low. Our long-time experience in silicon carbide research has been used to grow graphene as well as carbon nanotubes on single-crystalline SiC substrates.

Photovoltaics

PD Dr. H. Metzner



- Preparation and development of Cu(In,Ga)(Se,S)_2 - based thin film solar cells
- Preparation and development of CdTe-based thin film solar cells
- Investigation of epitaxially grown heterostructures for photovoltaics

The research of the *photovoltaics* group is directed to three different fields:

- Preparation and development of Cu(In,Ga)(Se,S)_2 - based thin film solar cells (CIGS). The research aims at a better understanding of the materials science of the CIGS chalcopyrite semiconductor and the improvement of existing and the development of novel cell concepts. To this end, a complete baseline on a form factor of $10 \times 10 \text{ cm}^2$ is available as well as various characterization tools including AM 1.5 solar simulation and spectral response.
- Preparation and development of CdTe-based thin film solar cells. The research aims at a better understanding of the materials science of the II-VI semiconductor CdTe and the improvement of existing and the development of novel cell concepts. To this end, a complete baseline on a form factor of $10 \times 10 \text{ cm}^2$ is available as well as various characterization tools including AM 1.5 solar simulation and spectral response.
- Investigation of epitaxially grown heterostructures for photovoltaics. The research aims at a better understanding of the materials science of heterostructures between silicon and CIGS and the development of novel cell concepts. To this end, a complete system for molecular beam epitaxy (MBE) is in operation which includes the *in situ* analysis by means of electron diffraction (RHEED).

The photovoltaics group collaborates with other university groups, research institutions, and the photovoltaic industry in numerous research projects.

The IFK photovoltaics group is member of the following institutions which include:

- **“Solar Input” e.V.**
a collaboration of photovoltaic industry and research institutions located in Thuringia,
- **“PV-Uni-Netz”**
a collaboration of photovoltaic research groups at 12 German universities.

MD simulation of defect accumulation and amorphization in AlGaAs

K. Gärtner, T. Clauß

The defect accumulation and amorphization in $\text{Al}_x\text{Ga}_{1-x}\text{As}$ due to ion irradiation has been widely investigated experimentally (e.g.[1-4]). In all cases it has been found that the irradiation resistance increases remarkably with increasing Al content x , especially, there is a sudden increase of the amorphization dose of about two orders of magnitude for $x > 0.9$ [2,4]. Different mechanisms of the defect accumulation and amorphization have been discussed, however, this behavior is not yet fully understood. Especially, the role of dynamic annealing is contradictorily discussed [1,3]

In this paper the damage production in $\text{Al}_x\text{Ga}_{1-x}\text{As}$ due to ion irradiation is investigated using computer simulation. Especially the dependence of the damage formation on the Al content x and the role of dynamic annealing are studied. The simulations are performed for the situation of the irradiation of $(001)\text{Al}_x\text{Ga}_{1-x}\text{As}$ with 200 keV Ar at 20 K, where experimental Rutherford backscattering (RBS) data for a wide range of the Al content x are available [2,4]. The simulation is performed in two steps. First, the generation of primary recoils is treated using the binary collision code TRIM and second, the evolution of the sub-cascades caused by the primary recoils is described by molecular dynamics (MD) simulations. The molecular dynamics simulations were done with a standard MD code using a modified Tersoff potential [5]. The ion irradiation is simulated by subsequently started primary recoils, each with an energy E_r . The deposited energy E_{dep} at a certain time is the sum of the energies E_r of the recoils started up to this time. For each value of E_{dep} the disorder n_{diso} is calculated which is introduced analogously to the relative number of displaced atoms obtained from the RBS results. For comparison with the experimental data, the deposited energy E_{dep} is transformed to the number of dis-

placements per atom n_{dpa} . The results for the disorder n_{diso} as a function of n_{dpa} are shown in Fig.1 for different Al contents x in comparison with the corresponding experimental data obtained by RBS.

Because the measured disorder for $x = 1$ needs a much larger n_{dpa} scale, the results for $x \leq 0.9$ and for $x = 1$ (and $x = 0$ for comparison) are presented separately in Figs. 1a and Fig. 1b. As can be seen, for $x \leq 0.9$ the simulated disorder agrees reasonable with the measured one, however, in the

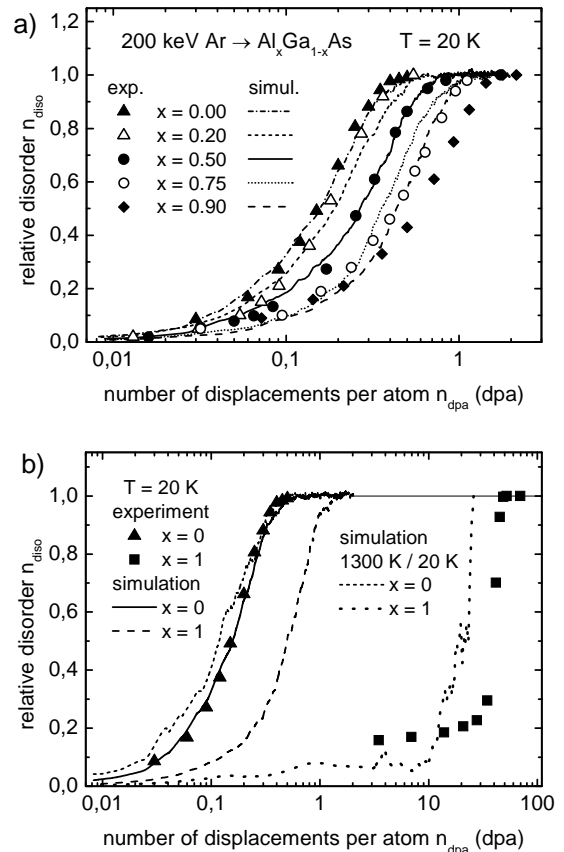


Fig. 1: The relative disorder n_{diso} generated in $\text{Al}_x\text{Ga}_{1-x}\text{As}$ by 200 keV Ar irradiation at 20 K as a function of the number of displacements per atom n_{dpa} for $0 \leq x \leq 0.9$ (a) and $x = 0$ and $x = 1$ (b). The experimental data are given by the symbols and the simulation results are presented by the lines. In (b) the simulation results for the irradiation at 1300 K are added.

case of $x = 1$ (Fig. 1b) the simulation result completely disagrees with the experimental data. The question arises whether the extreme behavior of the measured disorder for $x = 1$ (AIAs) is connected with long time annealing during the irradiation, which is not treated by the MD simulation. In order to check this, additional simulations have been performed estimating the influence of the long time annealing during the irradiation by an artificial acceleration of all thermal processes by using a temperature as high as possible, however, remarkably below the melting temperature (between 1530 K and 2030 K for different x). The results obtained for $x = 0$ and $x = 1$ using $T = 1300$ K during the irradiation are added in Fig. 1b. It is remarkable that for $x = 0$ there is no annealing effect at this high temperature (n_{diso} is even slightly larger) while for $x = 1$ the amorphization is drastically delayed by annealing. In order to estimate whether the thermal annealing in AIAs during the irradiation may play a role also at temperatures as low as 20 K, a sample with a disorder of about 0.5 has been relaxed at 20 K over 10 ns. The resulting rate for the change of the disorder is definitely negative and indicates that thermal annealing processes during the irradiation can exist in AIAs even at 20 K.

In order to get more information, the structure of the damage has been investigated. For this purpose, amorphous clusters were defined and their evolution has been studied for $T = 293$ K and 1300 K as well. The results show that the amorphous clusters can not only appear and grow but also shrink or disappear during the irradiation. The shrinking and disappearing (dynamic annealing) has been shown to play no remarkable role for $x = 0$ (even at $T = 1300$ K, that means there is also no long time annealing), but its influence increases with increasing Al content x . For $x = 1$ there is a strong long time dynamic annealing effect which can be observed with the MD simulation only by an artificial acceleration of these processes by using a high temperature (here $T = 1300$ K).

Summarizing, the process of the defect accumulation and amorphization can be understood as a result of the competition between the defect generation (appearance and growth of amorphous clusters) and the dynamic annealing (shrinking and disappearance of amorphous clusters) during the irradiation. As shown in Ref.[5], the rate of the defect generation decreases with increasing Al content x by a factor of about three. As found here, the dynamic (short time) annealing is negligible for $x = 0$ and it increases with increasing Al content x . The reasonable agreement of the simulation results with the experimental data in the case of $x < 0.9$ indicate that the damage accumulation and amorphization for $x < 0.9$ is correctly described by these two processes. However, the dynamic (short time) annealing does not explain the outstanding behavior of AIAs ($x = 1$). The results obtained using a high temperature during the irradiation show definitely that there must exist long time thermal annealing processes during the irradiation in AIAs which do not exist in GaAs. These processes are responsible for the extremely high irradiation resistance of AIAs.

References

- [1] H.H. Tan, C. Jagadish, J.S. Williams, J. Zou, D.J.H. Cockayne, A. Sikorski, *J. Appl. Phys.* 77 (1995) 87.
- [2] B. Breger, E. Wendler, Ch. Schubert, W. Wesch, *Nucl. Instr. and Meth. B* 148 (1999) 468.
- [3] B.W. Lagow, I.M. Robertson, L.E. Rehn, P.M. Baldo, J.J. Coleman, T.S. Yeoh, *J. Mater. Res.* 15 (2000) 2043.
- [4] A. Stonert, A. Turos, L. Nowicki, B. Breger, E. Wendler, W. Wesch, *Nucl. Instr. and Meth. B* 175-177 (2001) 219.
- [5] K. Gärtner, *Nucl. Instr. and Meth. B* 268 (2010) 149.

Structural modification of swift heavy ion irradiated amorphous germanium layers

T. Steinbach, W. Wesch, C.S. Schnohr,
 P. Kluth², Z.S. Hussain², L.L. Araujo², R. Giulian², D.J. Sprouster², A.P. Byrne², M.C. Ridgway²,
¹Department of Electronic Materials Engineering, Research School of Physics and Engineering,
 The Australian National University, Canberra ACT 0200, Australia

To study the effect of high electronic energy deposition on amorphous germanium (a-Ge) layers, crystalline germanium (c-Ge) wafers were amorphised by ion irradiation with various germanium ion energies and fluences at 80 K, resulting in a 3.1 μm thick amorphous layer. A grid of Au was evaporated on the sample surface which was then partly masked during the subsequent irradiation. The samples were irradiated with 89 and 185 MeV Au ions at room temperature with ion beam angles of incidence of 0°, 45° as well as 60° with respect to the surface normal. The Au ion fluence was varied between $2 \times 10^{12} \text{ cm}^{-2}$ and $2.2 \times 10^{14} \text{ cm}^{-2}$. The irradiated samples were analysed by optical microscopy, surface profilometry and scanning electron microscopy (SEM), which was used in plan-view as well as two different cross section geometries (XSEM).

Like in the case of amorphous silicon [1], SHI irradiation of amorphous germanium at room temperature shows a positive plastic flow as well, demonstrating that liquid polymorphism is common for these two semiconductors [2]. However, subsequent to irradiation, a change in sample surface colour from light brown to black accompanied by swelling of the amorphous layer was readily apparent with increasing ion fluence. This swelling is shown as a function of the implantation parameters in Fig. 1, where the mean step height Δy is depicted as a function of the ion fluence. As an example, the inset shows the elevation of an irradiated amorphous germanium layer as measured by the surface profilometer. The step height of the irradiated amorphous germanium layer increases with increasing ion fluence for all irradiation parameters used and indicates a linear dependence on the ion fluence, $\Delta y = \alpha N_I$, with a fit parameter α [3]. It is obvious, that the step height increases with increasing ion energy and

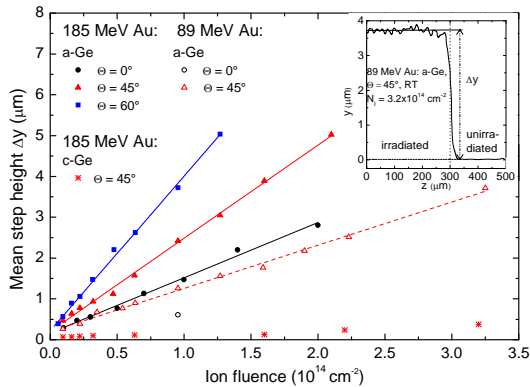


Figure 1: Mean step height Δy of the surface for amorphous germanium layers irradiated with different ion energies and different angle of incident as a function of the ion fluence Also shown is the data for crystalline germanium irradiated with 185 MeV Au under 45° as a reference sample. Data were fitted linearly (solid lines)

increasing angle of incidence. This can be attributed to the different electronic energy deposition ϵ_e . Hence, the step height and therefore the slope increase with increasing electronic energy deposition. XSEM investigations revealed the transformation of the initially homogeneous amorphous germanium layer into a sponge like porous structure with irregularly shaped voids thus establishing that the swelling was a consequence of void formation (cp. Fig. 3). However, in contrast to amorphous silicon in amorphous germanium the formation of voids begins at low ion fluence (10^{12} cm^{-2}).

In contrast to the amorphous samples, no significant swelling could be observed for the crystalline reference sample (cp. Fig.1). The measured step heights are less than 100nm up to an ion fluence of $1.6 \times 10^{14} \text{ cm}^{-2}$. With further irradiation a slightly increased step height was found which amounts to 350 nm for the highest ion fluence of $3.2 \times 10^{14} \text{ cm}^{-2}$. Furthermore, no change in reflectivity occurred in contrast to the amorphous samples.

As a consequence of the void formation a non linear plastic flow process is observed which is depicted in Fig. 2 [3]. The shift of the curves against each other reflects the dependence of the surface shift Δx on the incident angle Θ as well as the electronic energy deposition [4]. By means of cross section SEM (cross section parallel to the projection of the ion beam) it becomes apparent that within the a-Ge layer the voids do not appear to correspond to the direction of the ion tracks along which the energy is deposited into the electronic system of the amorphous germanium layer but rather reflect the ion beam induced plastic flow process in positive direction directly (see Fig. 3) [3].

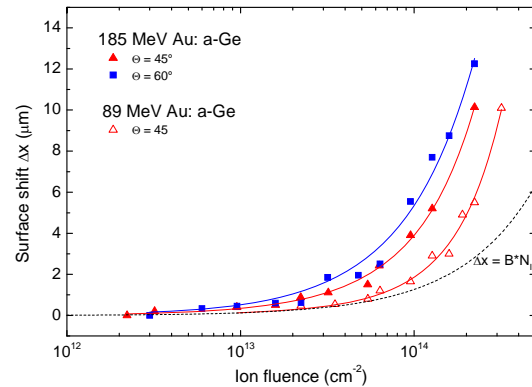


Figure 2: Surface shift Δx of the amorphous germanium layer as a function of the ion fluence for different non-perpendicular irradiation conditions. For comparison the dashed line represents a linear function.

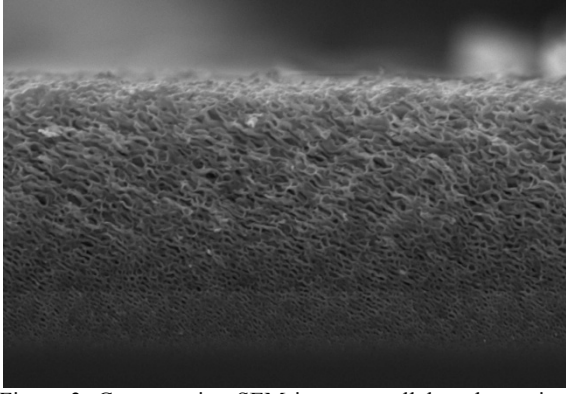


Figure 3: Cross-section SEM image parallel to the projection of the ion beam of an amorphous germanium sample irradiated at room temperature with 89 MeV Au ions under an angle of 45°.

In Fig. 4 the slopes α determined from Fig. 1 are depicted as a function of the electronic energy deposition ϵ_e . The slope increases linearly with increasing energy deposition. The extrapolation of the regression line yields an electronic energy deposition of about $\epsilon_e = (10.5 \pm 1.0) \text{ keV nm}^{-1}$ for a zero step height [3]. That means, for room temperature irradiation a threshold value of the electronic energy deposition can be determined above which the swelling, i.e. the formation of voids, begins. The existence of this threshold is also confirmed by the five mean step heights obtained after ion irradiation with a fixed ion fluence of $1.0 \times 10^{14} \text{ cm}^{-2}$ but at different values of ϵ_e , which are also included in Fig. 4 (right hand scale).

The threshold thus determined enables an explanation of the results achieved in case of the irradiation of crystalline germanium. As mentioned above, the swelling of the crystalline sample is constant over a wide range of ion fluences but increases significantly at high ion fluences (cp. Fig. 1). The reason for this becomes evident in the cross section SEM investigation [3]. Compared to the amorphous samples no porous layer can be seen at the surface, which is still crystalline and free of voids in accordance with the fact that no significant changes in reflectivity are observed. However, the formation of a buried porous layer causes the increased step height at high ion fluences. A similar buried porous layer next to the porous surface layer was ob-

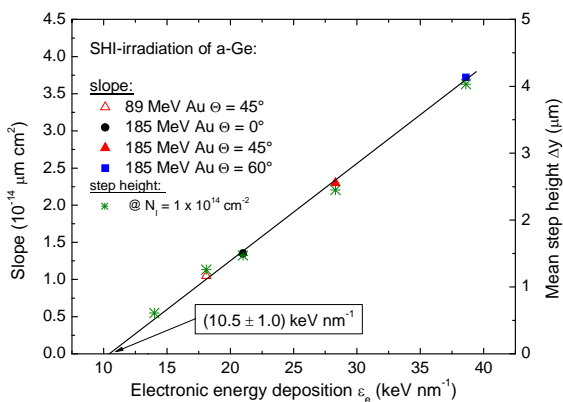


Figure 4: Slope α as well as the mean step height Δy for an ion fluence of $1.0 \times 10^{14} \text{ cm}^{-2}$ versus the electronic energy deposition for SHI irradiation of a 3.1 μm thick amorphous germanium layer.

served for irradiation of a germanium sample with a 3.1 μm thick amorphous surface layer under the same conditions (185 MeV Au and 45° angle of incidence) [2]. In both cases, the buried porous layer is located in a depth of approximately 6.5 μm referring to the initial surface. This depth corresponds to about two-thirds of the depth of the maximum nuclear energy deposition. Consequently, the formation of the buried layer cannot be attributed to the atomistic processes by which porosity is generated via nuclear energy deposition for low ion energies (see references in [3]), because obviously no voids are observed in the depth of the maximum of ϵ_n (approximately 10 μm). However, the electronic energy deposition does result in the formation of a buried damaged layer around the maximum of ϵ_n which broadens towards the surface with increasing ion fluence. The calculation of ϵ_e in a depth of about 6.5 μm for the corresponding irradiation conditions reveals a value of about 10.5 keV nm^{-1} which is in good agreement with the threshold of $(10.5 \pm 1.0) \text{ keV nm}^{-1}$ for void formation in amorphous germanium mentioned above. Thus a buried porous layer is formed in depths where ϵ_e exceeds the threshold value and where the initially crystalline material is amorphous due to nuclear energy deposition to allow ion beam induced void formation. This situation only occurs after irradiation of a sufficient high ion fluence which is the reason why the swelling of c-Ge remains constant over a wide range of fluence but then significantly increases above $N_1 \approx 2 \times 10^{14} \text{ cm}^{-2}$. Thus, the long-standing question concerning the formation depth of the buried porous layers during swift heavy ion irradiation of crystalline germanium [5] can be explained by the threshold value for void formation determined in the present experiment. Like the results of the crystalline germanium irradiation in our experiments, the authors in [5] report that all buried porous layers were formed in depth regions where the electronic energy deposition of the ions is about 10 keV nm^{-1} .

Based on these results, one may conclude that voids are formed in amorphous germanium if a specific threshold value of the energy deposited by electronic processes is exceeded.

References

- [1] Hedler A. et al. Nat. Mater. 3, 804, (2004).
- [2] Wesch W. et al., J. Phys. D: Appl. Phys. 42, 115402 (2009).
- [3] Steinbach T., Wesch W. et al. to be published.
- [4] Gutzmann A. et al. Phys. Rev. Lett. 74, 5072 (1995)
- [5] Huber H. et al. Mater. Sci. Forum 248-249, 301 (1997)

Work supported by DAAD, contract no. D/07/15034.

Structural modification of low temperature swift heavy ion irradiated amorphous germanium layers*

T. Steinbach, C.S. Schnohr¹, W. Wesch, M.C. Ridgway¹, D. Severin² and M. Bender²
¹ ANU, Canberra ACT 0200, Australia; ²GSI, Darmstadt, Germany

Swift heavy ion (SHI) irradiation of conventional glasses results in non-saturable plastic flow as a consequence of the ion hammering effect [1]. SHI irradiation of amorphous Si (a-Si) at non-perpendicular incidence also leads to unsaturated plastic flow, which shows a linear dependence on the ion fluence. The positive direction of flow suggests that a liquid phase of similar density to that of the amorphous solid must exist [2]. For room temperature irradiation of a-Si to a very high fluence ($\sim 2.5 \times 10^{15} \text{ cm}^{-2}$), the plastic flow is accompanied by swelling due to the formation of voids. Room temperature SHI irradiation of amorphous Ge performed at the ANU accelerator facility have shown a positive plastic flow as well, demonstrating that liquid polymorphism is common for these two semiconductors [3]. In contrast to amorphous Si, the formation of voids in amorphous germanium begins at a much lower fluence ($10^{12} \text{ ions/cm}^2$). As a consequence of the void formation, a non linear plastic flow process is observed. Figure 1 shows an optical micrograph image of the surface of the amorphous germanium layer with a thin quadratically shaped gold marker layer. By means of the gold squares on the samples surface the two effects, namely plastic deformation and swelling are clearly visible (see [3, 4] for more information).

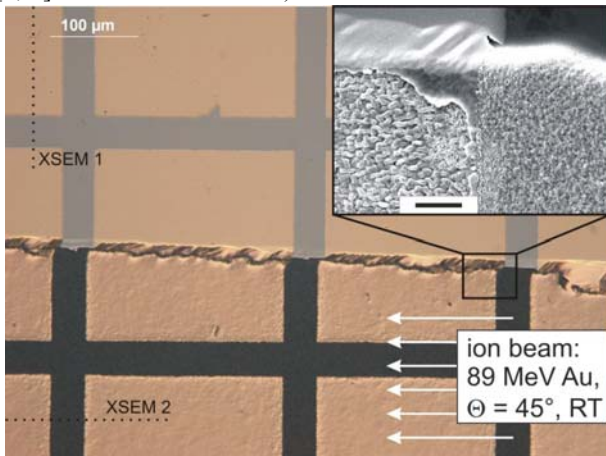


Figure 1: The optical micrograph shows plastic flow as well as swelling of an irradiated amorphous germanium layer. The irradiation was performed at room temperature using 89 MeV Au ions under an angle of $\Theta = 45^\circ$. The inset shows the corresponding SEM image with a higher magnification (scale bar: 5 μm).

In this project we investigated the effect of the irradiation temperature as well as the influence of higher electronic energy deposition on the void formation in a-Ge. The experiments were performed at the new M3-branch at the UNILAC. The sample was irradiated at cryogenic

temperature ($T = 45 \text{ K}$) with 1.4 GeV U-ions under 45° beam incidence. The ion flux was $4 \times 10^9 \text{ cm}^{-2} \text{ s}^{-1}$, the fluence ranged between 5×10^{12} and $1.5 \times 10^{14} \text{ cm}^{-2}$. This first low temperature irradiation of amorphous germanium shows that in contrast to a 77 K irradiation of Si (no voids over a wide fluence range up to $8 \times 10^{15} \text{ cm}^{-2}$), voids formation in a-Ge was observed at a rather low ion fluence of $\sim 10^{12} \text{ cm}^{-2}$.

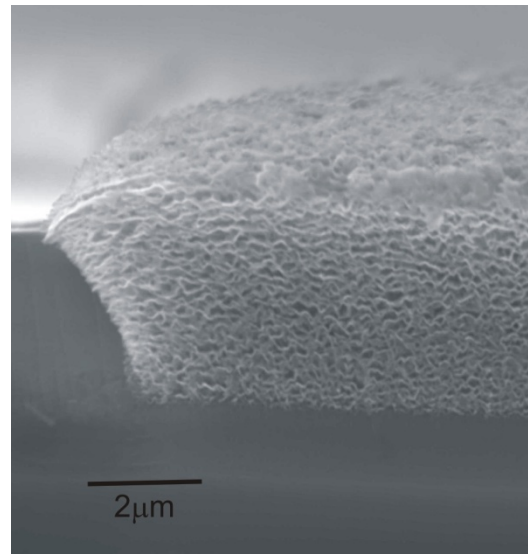


Figure 2: The cross section SEM (XSEM 1, cp. Fig.1) image shows the transformation of the homogeneous a-Ge layer into a sponge-like porous germanium layer after irradiation with 89 MeV Au ions (fluence: $2.3 \times 10^{14} \text{ cm}^{-2}$).

The mechanisms of void formation and the transformation into a sponge like structure are not yet understood and will be subject of further investigations. For this purpose, a new target holder was constructed allowing simultaneous irradiations at room and low temperature, which enables the comparison of both samples under same irradiation conditions.

References

- [1] S. Klaumünzer et al. Phys. Rev. Lett. 51 (1983) 1987.
- [2] A. Hedler et al. Nat. Mater. 3 (2004) 804.
- [3] W. Wesch et al., J. Phys. D: Appl. Phys. 42 (2009) 115402.
- [4] T. Steinbach, C.S. Schnohr, W. Wesch, to be published.

* Work supported by BMBF, contract no. 05KK7SJ1 and DAAD, contract no. D/07/15034.

Stress and plastic flow in germanium during amorphization by ion bombardment*

T. Steinbach, J. Wernecke, W. Wesch, D. Severin¹ and M. Bender¹
¹GSI, Darmstadt, Germany

This project investigates density changes and plastic phenomena in crystalline germanium (c-Ge, [100]) during the irradiation with swift heavy ion. By means of a new scanning laser reflection technique [1], the bending (curvature radius) of a freestanding germanium sample was measured as a function of ion fluence.

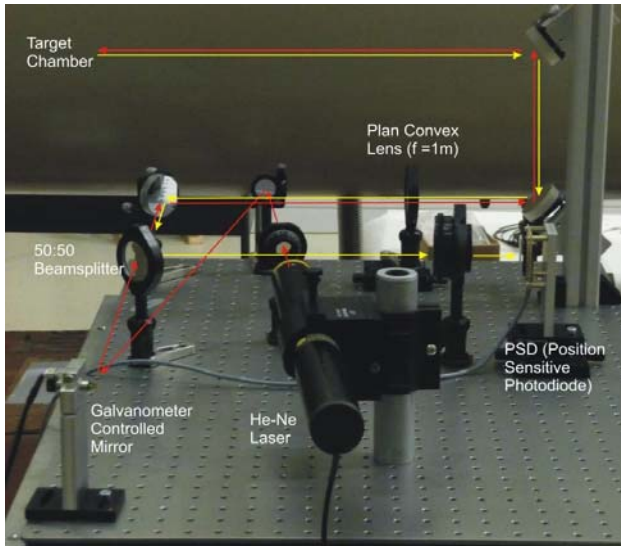


Figure 1: In-situ sample curvature measurements using a scanning laser reflection technique [1]: The image shows the horizontal path of the laser beam on the optical breadboard as well as the vertical deflection of the laser beam into the chamber. The red line indicates the primary beam, and the yellow line represents the beam reflected by the sample in the chamber.

The laser reflection system was recently installed at the newly established M3-beamline at the UNILAC (Fig. 1), providing in-situ stress measurements. The system was calibrated with a mirror of known curvature radius ($R_{\text{cal}} = 5 \text{ m}$). One side of the bar-shaped c-Ge crystals ($2 \times 10 \text{ mm}^2$, thickness $275 \mu\text{m}$) was mounted, in such a way that the sample were quasi freestanding (see inset Fig. 2). The irradiation was performed at room temperature with 1.4 GeV Xe ions under normal incidence. At this energy, the range of the Xe ions is $\sim 66 \mu\text{m}$. The beam flux was $2 \times 10^9 \text{ cm}^{-2} \text{ s}^{-1}$, and the fluence ranged between 1×10^{11} and $1 \times 10^{13} \text{ ions/cm}^2$. The curvature measurements were carried out in situ during short beam interruptions. These irradiation conditions lead to the formation of a buried damaged layer, i.e. stress build up in the sample due to defect creation in the nuclear stopping regime [2].

Figure 2 shows the ion beam induced change of the in-plane stress as a function of the ion fluence. The stress

state of the sample was calculated using the equation of Stoney [2]:

$$S = \int_0^{t_d} \sigma(x) dx = \frac{Y_0 t^2}{6R}, \quad (1)$$

where t_d denotes the thickness of the damaged area, $\sigma(x)$ is the local stress in depth x , Y_0 is the Young's modulus for c-Ge, t is the thickness of the sample and R is the radius of curvature.

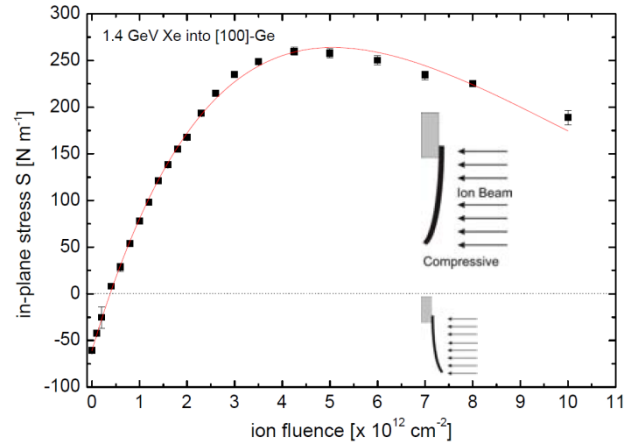


Figure 2: In-plane stress S versus ion fluence for room temperature irradiation of c-Ge with 1.4-GeV Xe ions. The inset illustrates the bending of the sample. Compressive stress ($S > 0$) corresponds to bending of the sample away from the ion beam.

The initial stress state of the sample was negative ($S < 0$). As a result of the defects formed during ion irradiation, the density is reduced leading to compressive stress ($S > 0$), i.e. the sample bends away from the ion beam. The curvature and thus the stress increases continuously with increasing fluence. For $5 \times 10^{12} \text{ ions/cm}^2$, the stress reaches a maximum of 264 N/m . With further irradiation, the compressive stress state slowly decreases due to incipient plastic deformations.

References

- [1] C.A. Volkert, J. Appl. Phys. 70, 3521 (1991).
- [2] G. Stoney, Proc.Roy. Soc. A 82, 172 (1909).

* Work supported by BMBF, contract no. 05KK7SJ1

Ultrathin membranes in x-cut lithium niobate

F. Schrempel*, Th. Gischkat, H. Hartung*, E.-B. Kley*, A. Tünnermann*, W. Wesch

**Institut für Angewandte Physik, A.-Einstein-Str. 15, 07745 Jena*

It is shown that ion-beam enhanced etching is well applicable to pattern lithium niobate (LN) with ultrathin, high-index contrast membranes, which is achieved by an air gap between membrane and substrate. A

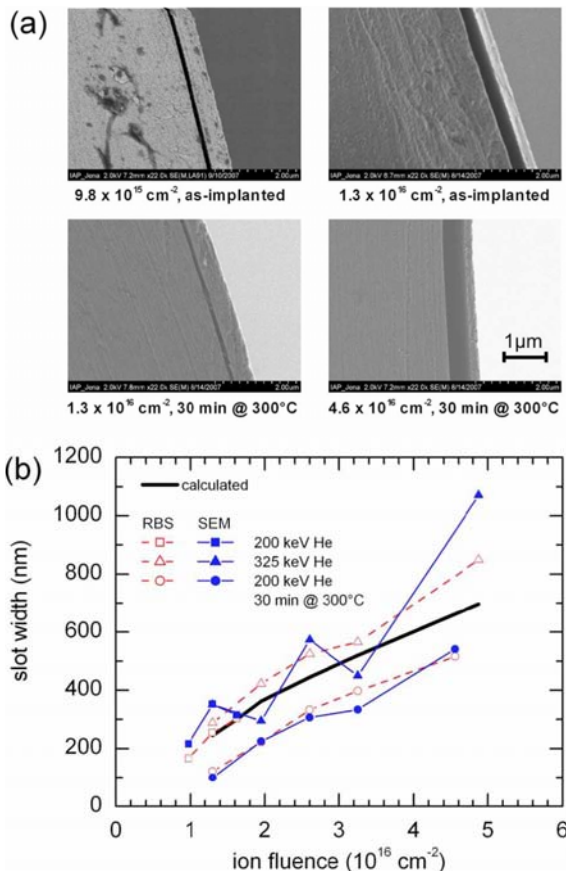


Fig. 1 (a) Side view SEM images of membranes fabricated in x-cut LN by irradiation with 200 keV He ions at 100 K. (b) Width of the air gap as a function of the ion fluence. Thermal treatment was applied at 300°C for 30 min, and etching was done in 3.7% HF solution at 40 °C.

buried amorphous layer, created by irradiation with ions, is removed by means of wet chemical etching in HF solution. In order to avoid surface damage, only light ions (e.g. He) can be used. In case of room-temperature irradiation, the surface layer is destroyed owing to crack formation. For irradiation with He ions at low temperatures,

gas bubble formation along with stress is suppressed, and membrane thicknesses down to 200 nm can be achieved.

Figure 1 shows scanning electron microscope pictures of membranes as well as the width of the air gap as a function of the ion fluence. The widths detected from the SEM images and those estimated from the damage profiles as well as from calculations are in good agreement. The slot thickness increases with increasing ion fluence. Accordingly, the membrane thickness drastically decreases until the surface of the membrane is attacked by the HF solution. Generally, the thicknesses of the membranes and the slots are uniform over the entire laterally etched area with respect to the crystal surface. Both the surface and the backside of the membranes are very smooth, having roughnesses of the order of optical grade polished LN. The widths of membrane and air gap can be adjusted independently over a wide range by proper adaptation of ion energy and fluence. Thermal treatment prior to the etching process increases contrast of the etch selectivity enabling the adjustment of slot and membrane widths with high accuracy. Although the low etch rates do not allow for the fabrication of large-area films, the process enables the 3D integration of advanced optical systems such as photonic crystal devices in bulk LN crystals. The achievable area depends on the configuration of apertures, which enables the access of the etchant.

Work was funded by the Deutsche Forschungsgemeinschaft under 1199/2-1.

For details and references see [F. Schrempel et.al., Opt. Lett. 34 \(2009\) 1426.](#)

Photonic crystals in lithium niobate by ion-beam enhanced etching

H. Hartung*, R. Geiß*, Th. Gischkat, F. Schrempel*, R. Iliew**, T. Pertsch*, F. Lederer**,
W. Wesch, E.-B. Kley*, A. Tünnermann*

**Institut für Angewandte Physik, A.-Einstein-Str. 15, 07745 Jena*

***Institut für Festkörpertheorie und -optik, Helmholtzweg 4, 07743 Jena*

A relatively simple Photonic crystal (PC) defect waveguide structure in a free standing lithium niobate (LN) membrane fabricated by means of ion-beam enhanced etching (IBEE) is presented. The periodic structure consists of a hexagonal array of air holes (period of 620 nm and a hole diameter of 350 nm) designed to have a band gap at 1550 nm wavelength for TE polarized light. The membrane thickness does not exceed 500 nm in order to guarantee confinement and single mode guiding in the vertical direction.

Figure 1 shows the calculated band structure of the PC defect waveguide consisting of three rows of missing holes (W3). The simulations were done using a 3D plane wave expansion method showing that the band gap of this structure is situated between 1494 and 1742 nm.

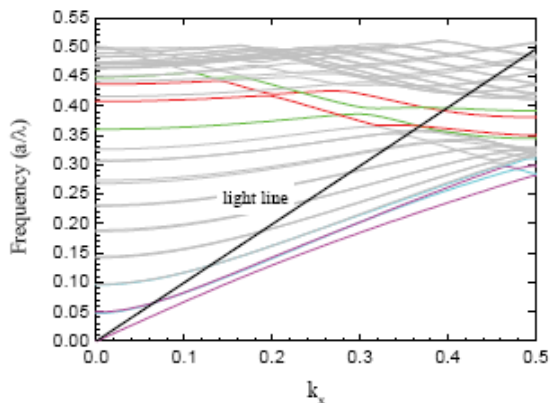


Fig. 1 Band diagram of the W3 photonic crystal waveguide. Colored lines represent waveguide modes inside the band gap (red and green) and index guided (blue and violet).

In the IBEE process the crystalline material is irradiated with high energetic ions to amorphize the original crystal structure, with a patterned layer of fused silica acting

as a mask. The amorphous regions are removed by wet etching in hydrofluoric acid. After removal of the mask a second irradiation is performed without any masking producing a confined amorphous region at a defined depth giving rise to an under etched area underneath the PC membrane (Fig. 2).

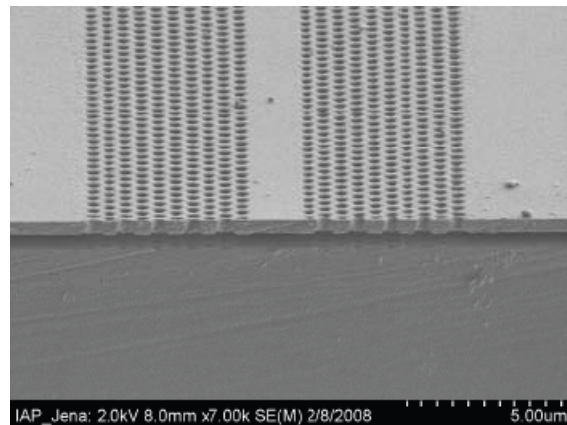


Fig. 2 Scanning electron microscope photograph of the polished end facet of a W3 PC waveguide in a freestanding LN membrane produced by IBEE.

Expected limitation for the usage of IBEE are PC geometries with periods of about 300 nm and hole diameters of up to 50 nm which in principle would allow for a band gap in the visible spectral range. Feasible membrane thicknesses range from 300 to 700 nm. Lateral lengths of several hundred micrometers are achievable. A potential device, for example, could be a microcavity optic parametric oscillator realized by confining light to a point defect in a hexagonal lattice of air holes.

Work was funded by the Deutsche Forschungsgemeinschaft under 1199/2-1.

For details and references see [H. Hartung et.al., IEEE/LEOS Winter Topical Meeting Series \(2009\) 64.](#)

Study of iodine diffusion in silicon carbide

E. Friedland^a, N.G. van der Berg^a, J.B. Malherbe^a, R.J. Kuhudzai^a, A.J. Botha^b
E. Wendler, W. Wesch

^a Department of Physics, University of Pretoria, Pretoria 0002, Republic of South Africa

^b Laboratory for Microscopy and Microanalysis, University of Pretoria, Pretoria 0002, Republic of South Africa

Fuel elements of modern high-temperature nuclear reactors (HTR) are encapsulated by four successive CVD-layers of low-density pyrocarbon, high-density pyrocarbon, silicon carbide (SiC) and high-density pyrocarbon, which serve as barriers to prevent fission product release. These so-called TRISO particles retained quite effectively most of the important fission products at core temperatures of almost 1000 °C in the first two experimental Pebble Bed Reactors commissioned in Germany during the second half of the last century. However, very little information is available on the fission product retention capability of silicon carbide at temperatures above 1000 °C.

The aim of this study is to obtain information on iodine diffusion through well-defined layers of polycrystalline and single crystalline SiC above 1000°C. Radio-active iodine isotopes, especially ¹²⁹I ($T_{1/2} = 15.7 \times 10^6$ y) and ¹³¹I ($T_{1/2} = 8$ d), are important fission products and of radio-ecological relevance because of their accumulation in the thyroid gland with a biological half-life of approximately 140 days.

Single crystalline hexagonal 6H-SiC and polycrystalline CVD-SiC were implanted with 360 keV ¹²⁷I⁺ to a fluence of 10^{16} cm⁻² at room temperature. The implanted wafers were vacuum annealed in a *Webb Red Devil*[®] graphite furnace for periods ranging from 5 to 120 hours at temperatures up to 1300 °C.

The microstructure of the samples was investigated by scanning electron microscopy (SEM) employing a *Zeiss Ultra 55*[®] instrument operating at an accelerating voltage of 2 kV. Depth profiles were obtained by Rutherford backscattering spectrometry (RBS) at room temperature using α -particles with energies between 1.4 and 1.8 MeV.

At first poly- and single crystalline samples were subjected to isochronal annealing cycles of 5 hours each for temperatures between 900°C and 1300°C. Iodine profiles of a CVD sample are shown in Fig. 1 after annealing cycles of 1000°C, 1200°C and 1300°C. At 1000°C no change was observed relative to the as-implanted sample.

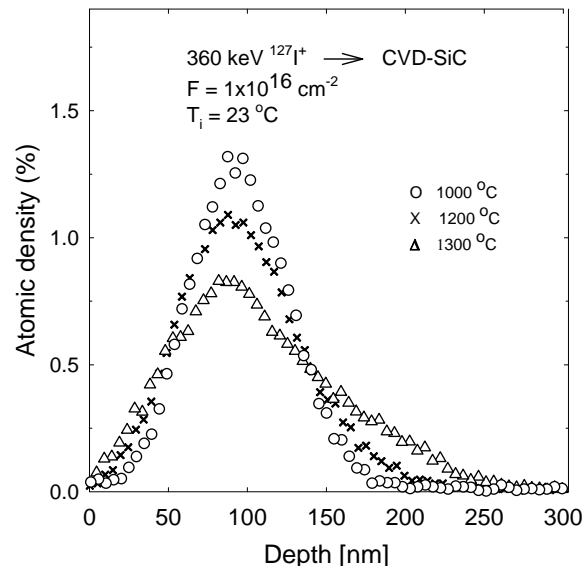


Fig. 1: Iodine depth profiles in CVD-SiC as a function of isochronal annealing. No broadening relative to an as-implanted profile is observed after the annealing cycle at 1000 °C.

As iodine transport becomes observable between 1100 °C and 1200°C, isothermal annealing studies were performed at these two temperatures. The widths of the iodine depth distribution as a function of annealing time were used to determine the following diffusion coefficients (for details see [1]):

$$D_{6H} = (0.6 \pm 0.4) \times 10^{-21} \text{ m}^2 \text{ s}^{-1} \text{ and}$$

$$D_{\text{CVD}} = (0.7 \pm 0.6) \times 10^{-21} \text{ m}^2 \text{ s}^{-1} \text{ at } 1100^\circ\text{C},$$

$$D_{6H} = (2.5 \pm 0.3) \times 10^{-20} \text{ m}^2 \text{ s}^{-1} \text{ and}$$

$$D_{\text{CVD}} = (5.7 \pm 0.5) \times 10^{-20} \text{ m}^2 \text{ s}^{-1} \text{ at } 1200^\circ\text{C}.$$

The results for 1100 °C, which are at the detection limit of RBS, can be accommodated with those in [2], who found no diffusion in a similar experiment after annealing at 1000°C for 30 minutes. The sudden increase by almost two orders of magnitude at 1200°C is unexpected and somewhat surprising. Such behaviour is rather unlikely to be due to Fickian diffusion, but is indicative of a different transport process becoming important in this temperature region. SEM pictures reveal a drastic change of the surface topography between 1100°C and 1200°C, which is not observed with un-

implanted SiC wafers at even much higher temperatures. Surfaces of as-implanted 6H-SiC and CVD SiC wafers are absolutely featureless due to the complete disorder of the lattice. Fig. 2 depicts surfaces of 6H SiC after 15 min annealing at 1100°C and 1200°C, showing long thin crystals growing in random directions from a growth centre, while the rest of the surface is densely covered with small crystals of irregular shape. The two images show similar structures after 15 min annealing except that the irregular crystals have grown significantly larger at the higher temperature. After 60 h annealing at 1100°C, the structure is fundamentally not much different from the one observed after 15 min annealing [1]. However, at 1200 °C large faceted crystals have grown, creating deep cavities in their neighborhood because of the resultant mass transport thereby exposing the implanted iodine. The observation that cavities cover roughly 20% of the surface while only 10% of the iodine is lost serves as a proof of its relatively strong binding to the lattice [1].

The general appearance of the surface structures is independent on whether single or polycrystalline samples are used. Iodine implanted 6H-SiC and CVD-SiC display similar crystallization phenomena at any particular annealing stage. Prolonged annealing at 1200 °C leads in both cases to the growth of large crystals. As no

crystallization effects are observed on un-implanted surfaces, these phenomena might be related to chemical reactions between the implanted iodine and the silicon carbide lattice at high temperatures.

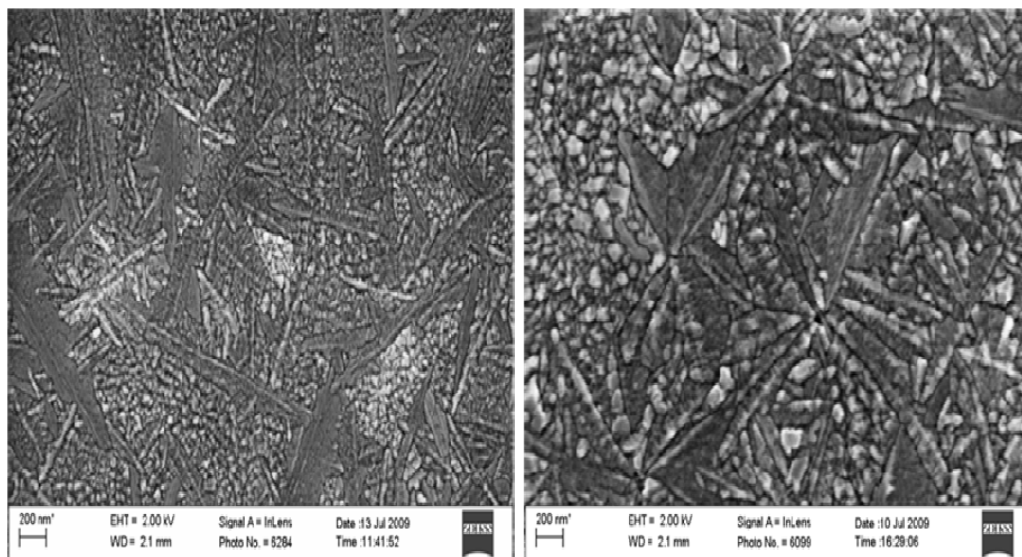
The results indicate that intact silicon carbide coatings of typically 35 µm thicknesses in fuel kernels should effectively prevent iodine release into the reactor's primary cooling system during their total resident time in the core at 1000°C. However, operating at higher temperatures, as envisaged in some advanced design studies, might be problematic if silicon carbide coated fuel particles are used. Fission produced iodine isotopes might chemically attack these coatings, leading to fuel element failure.

Acknowledgement

The work is supported by the BMBF (International Cooperation in Research and Education; Project-No. SUA 08/028) and by the National Research Foundation of South Africa.

References:

- [1] E. Friedland, N.G. van der Berg, J.B. Malherbe, R.J. Kuhudzai, A.J. Botha, Nucl. Instr. and Methods B, in press.
- [2] A. Audren, A. Benyagoub, L. Thomé, F. Garri-do, Nucl. Instr. and Meth. B 257 (2007) 277.



6H-SiC, T - 1100 °C, t - 15min

6H-SiC, T - 1200 °C, t - 15 min

Fig.2: SEM images of iodine implanted 6H-SiC surface after 15 min annealing at 1100 °C and 1200 °C. Similar images are obtained for implanted CVD-SiC surfaces.

Temperature dependence of damage formation in Ag ion irradiated SiC

E. Wendler, Th. Bierschenk, W. Wesch, E. Friedland¹, J. B. Malherbe¹

¹ Department of Physics, University of Pretoria, Pretoria 0002, Republic of South Africa

Modern high-temperature nuclear reactors are based on coated fuel particles. One coating component is SiC which acts as a main diffusion barrier for energetic fission products like e.g. iodine and silver (for details see e.g. [1]). Therefore, it is essential to know the structural changes of SiC during the irradiation with these fission products at elevated temperatures and the influence on the diffusion [1]. In the present paper damage production in SiC is studied applying 360 keV Ag ions at various temperatures. Our earlier investigations of high temperature ion implantation of SiC mainly focused on the determination of critical ion fluences necessary for amorphisation and less attention was devoted to processes occurring at lower fluences [2]. In this paper the ion fluence was varied over a wide range allowing a careful analysis of the defect formation with special emphasis on very low fluences and the shape of the defect profiles.

In this study $\langle 0001 \rangle$ oriented 4H-SiC samples were implanted with 360 keV Ag ions at a temperature of $T_1 = 15, 295, 375, 475, 625$ or 875 K. Depending on the temperature, the ion fluence N_1 varied between 1×10^{11} and 2×10^{16} cm^{-2} . Rutherford backscattering spectrometry in channelling mode is applied to measure the damage concentration after implantation, using 1.4 MeV He ions and a backscattering angle of 170° . The computer code DICADA [3] is applied to calculate the defect profiles from the Si part of the measured spectra. In particular, defect profile means the relative concentration of uncorrelated and randomly displaced lattice atoms, n_{da} , versus depth z . For comparison, the depth distribution of primary displacements and implanted ions were calculated with the computer code SRIM2008.04 [4].

The results obtained for the various temperatures can be divided into two groups [5]: (i) For irradiation temperatures between 15 and 475 K amorphisation of the implanted layers is reached for ion fluences between 7×10^{13} and 3×10^{14} cm^{-2} . The depth of maximum damage is constant, independent of the ion fluence ap-

plied, and agrees reasonably with the theoretical predictions of SRIM [5]. (ii) For irradiations performed at 625 and 875 K no amorphisation is found for ion fluences as high as 2×10^{16} cm^{-2} and the depth of maximum damage coincides with the depth of maximum ion concentration. As an example for the latter group Fig. 1 shows the energy spectra of backscattered ions measured for a target temperature of 625 K (upper part) and the resulting defect profiles (lower part).

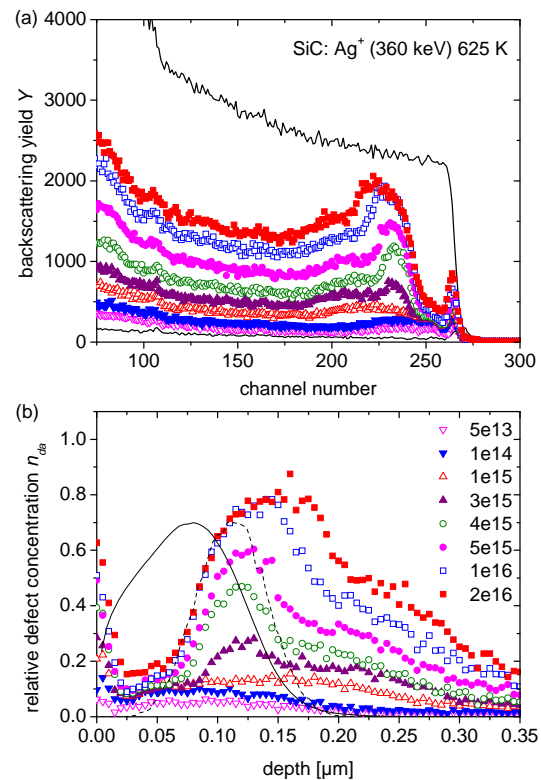


Fig. 1: (a) Energy spectra of He ions backscattered from Ag implanted SiC at 625K and for various ion fluences and (b) defect profiles resulting from the spectra in part (a) (for details see text). The ion fluences are given in cm^{-2} . For comparison the distribution of primary displacements and implanted ions are given by the solid and dashed line, respectively.

It is obvious from Fig. 1 (b) that - especially at higher ion fluences - the defect concentration does not reach zero behind the implanted layers

which extend to about $z \approx 0.23 \mu\text{m}$, and long tails occur. Such a shape of defect profiles indicates the existence of uncorrelated and correlated displaced lattice atoms due to the presence of both point defects/point defect clusters and extended defects - most probably - dislocations (for a detailed discussion see [6]). The onset of the damage peak at $N_1 \approx 1 \times 10^{15} \text{ cm}^{-2}$ occurs at the depth of maximum ion concentration and not at the depth of maximum displacements. This suggests that the implanted ions form seeds for the nucleation and growth of defects, especially for the growth of extended defects.

A summary of the results is given in Fig. 2 which plots the defect concentration in the maximum of the measured distribution, $n_{\text{da}}^{\text{max}}$, as a function of the ion fluence for all implantation temperatures applied. The curves are fitted to the experimental data using a defect-interaction and amorphisation model which comprises the generation, recombination and stimulated growth of defects (for a detailed discussion see [5, 7]).

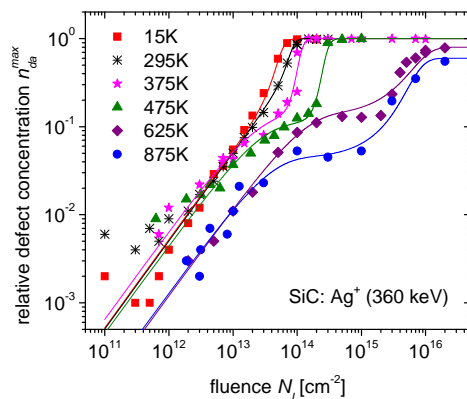


Fig. 3: Defect concentration in the maximum of the measured distribution, $n_{\text{da}}^{\text{max}}$, versus the ion fluence N_1 for 360 keV Ag ion implantation in SiC at various temperatures. The lines are calculated with a defect-interaction and amorphisation model (for details see [5, 7]).

In conclusion, the following picture can be designed for the damage formation in SiC ion-implanted at various temperatures. A significant change of the mechanisms of damage formation in 360 keV Ag implanted SiC occurs between 475 and 625 K. This range of temperatures coincides with that of annealing stages which may be attributed to the mobility of vacancies [5]. These mobile defects can promote the defect recombination within the collision cascades of individual ions, thus reducing the amount of damage remaining after implantation. At irra-

diation temperatures up to 475 K an almost equal over-all cross section of defect formation is obtained from the data at very low ion fluences for all temperatures in that range. This cross section involves the formation of point defects and amorphous clusters within a single ion impact. With rising temperature the transition to amorphisation shifts to higher ion fluences (see Fig. 1). This can be explained by a decrease of the relative amount of amorphous clusters within single ion impacts in crystalline SiC and by a reduced growth of already existing amorphous clusters [5]. Contrary, at temperatures of 625 and 875K only point defects are produced. With rising ion fluence the balance between formation and recombination of point defects causes a plateau of the defect concentration over a wide range of fluences. A second step of damage formation is related to the increasing concentration of implanted ions in the implanted layer. A complicated defect structure, consisting of clusters of point defects and extended defects - most probably dislocations, starts to grow, which is supported by the mobility of intrinsic defects.

Acknowledgement

The work is supported by the BMBF (International Cooperation in Research and Education; Project-No. SUA 08/028) and by the National Research Foundation of South Africa.

References

- [1] E. Friedland, J.B. Malherbe, N.G. van der Berg, T. Hlatshwayo, A.J. Botha, E. Wendler, W. Wesch, *J. of Nucl. Mater.* 389 (2009) 326.
- [2] E. Wendler, A. Heft, W. Wesch, *Nucl. Instr. and Methods B* 141 (1998) 105.
- [3] K. Gärtner, *Nucl. Instr. and Solids B* 227 (2005) 522.
- [4] J.F. Ziegler, J.P. Biersack, U. Littmark, *The Stopping and Ranges of Ions in Solids*, Pergamon, New York, 2003; www.srim.org.
- [5] E. Wendler, Th. Bierschenk, W. Wesch, E. Friedland, J. B. Malherbe, *Nucl. Instr. and Methods B*, in press.
- [6] E. Wendler, O. Bilani, K. Gärtner, W. Wesch, M. Hayes, F.D. Auret, K. Lorenz, E. Alves, *Nucl. Instr. and Methods B* 267 (2009) 2708.
- [7] E. Wendler, *Nucl. Instr. and Methods B* 267 (2009) 2680.

New UV-VIS and FTIR spectrometer at the IFK

S. Geburt, T. Bierschenk, E. Wendler, W. Wesch, C. Ronning

In October 2009, the old spectrometers at the IFK have been replaced by new UV-VIS and FTIR spectrometers.

The UV-VIS spectrometer Varian Cary 5000 [1] is sensitive from 175 to 3300 nm ($57000 - 3000 \text{ cm}^{-1}$) without spectral gap.

The configuration of the system is completely computer controlled and allows easy and fast experiments with scanning speeds up to 600 nm/min. For high resolution experiments, the minimal spectral bandwidth can be reduced below 0.01 nm. Due to the high sensitivity of the detectors and electronics, light intensity over more than 7 orders of magnitude can be detected. The standard sample holder allows transmission and absorption measurements. An additional sample holder for reflection measurements (incidence angle of 12°) is available; an Ulbricht sphere enables the measurement of direct and diffuse scattered light.

The Varian 640-IR Fourier-transformed IR (FTIR) [1] spectrometer is sensitive in the range between 400 to 6000 cm^{-1} (25000 - 1670 nm). The system allows the acquisition of the whole spectral range within seconds and a high resolution down to 0.25 cm^{-1} . In addition to the standard sample holder for transmission and absorption, a holder for reflection measurements (incidence angle of 10°) is available.

The two new spectrometers have a spectral overlap from 1670 to 3000 nm, therefore wide range measurements from 175 to 25000 nm ($57000 - 400 \text{ cm}^{-1}$) can be performed. This was tested on first experiments measuring the transparency of irradiated SiC samples.

Polished 4H-SiC pieces were irradiated with thermal and fast neutrons at the BER II reactor in Berlin for different times. The transmission of the samples was measured

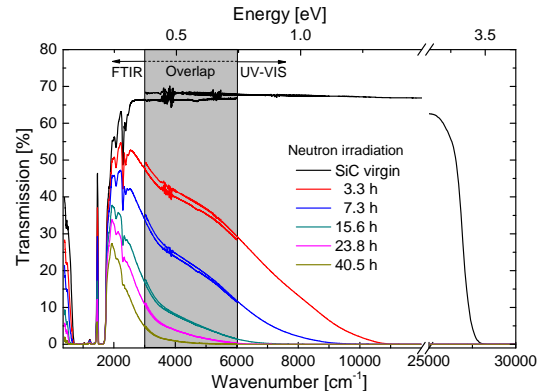


Fig. 1 Transmission spectra of neutron irradiated 4H-SiC recorded with the UV-VIS and FTIR spectrometers. The virgin SiC sample is transparent between 2200 and 27000 cm^{-1} . Upon neutron irradiation, the transparency decreases due to the formation of displaced lattice atoms.

from 400 to 30000 cm^{-1} using both spectrometers (Fig. 1). The spectra show a good overlap with a maximum shift of 3%. Further tests reduce the shift of the transmission spectra.

The virgin SiC sample shows a good transparency between 2200 and 27000 cm^{-1} . Upon irradiation, the transparency decreases significantly and vanishes nearly completely for an irradiation time of 40.5 hours.

The origin of the transparency loss is related to an increased fraction of displaced lattice atom which was confirmed by RBS channelling experiments. Although the relative fraction of displacements is still low ($\sim 2\%$) at the highest irradiation time, the effect on the transmission is strong. The reason can be found in the neutron irradiation itself: whereas ion implantation usually induces lattice damage in a layer close to the surface, which is usually small compared to the sample thickness, the irradiation with neutrons damages the material along the complete sample depth.

[1] see Handbook or www.varianinc.com

Cadmium Sulfide Nanowires: Growth

A. McDonnell, M. Kozlik, C. Borschel, S. Geburt, C. Ronning

Introduction

The aim of this work was to grow high quality CdS nanowires for later use in optical lasing experiments*.

Experimental

CdS nanowires were grown in a horizontal tube furnace via the vapor-liquid-solid (VLS) mechanism [1]. The CdS source powder was heated to 700°C and the sublimated material was transported by Ar carrier gas towards the growth substrates, covered with a sputtered Au catalyst layer. The substrates were kept at temperatures from 450 to 700 °C and the growth was investigated at different gas pressures between 5 and 200 mbar.

Characterization of the growth products was performed by scanning and transmission electron microscopy (SEM, TEM), X-ray spectroscopy (EDX), and cathodoluminescence (CL) spectroscopy.

Results and Discussion

Depending on growth pressure and temperature, different nanostructures were observed to grow, as illustrated schematically in figure 1. Long and straight nanowires with typical diameters of about 50-300 nm are obtained at growth temperatures around 650°C and pressures of about 30-100 mbar. The SEM image in figure 2 illustrates typical straight nanowires. In the TEM image, the remaining gold cap can be seen showing that the nanowires grow indeed via the VLS-mechanism. EDX measurements in the TEM confirm that the NW consist of stoichiometric CdS while the tips consist of

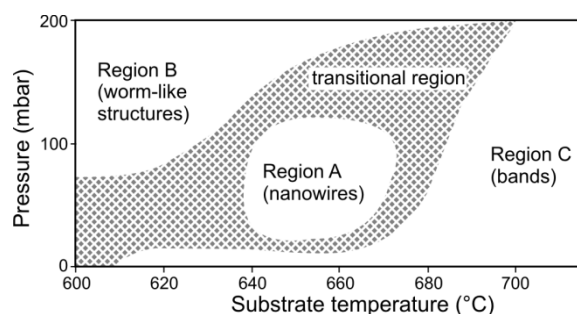


Fig. 1: Schematic phase diagram of CdS nanostructure growth. In different regions A-C, different nanostructures grow. In the transitional region multiple structures are found.

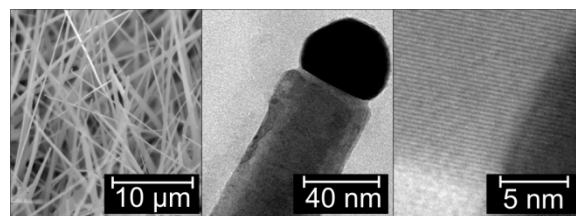


Fig. 2: Left to right: SEM image of CdS nanowires, TEM image of a single wire with gold tip, high resolution TEM image showing crystal planes.

gold. The HR-TEM image indicates the good crystal quality of the nanowires.

The CL spectra taken of the CdS NW (not shown here) mainly show band-edge emission. The emission from defects is at least two orders of magnitude lower, indicating good quality for optical experiments.

Conclusion

The growth of CdS nanostructures was investigated and the optimum parameters for nanowire growth were determined. Highly crystalline nanowires grown via the VLS mechanism can be obtained.

References

1. R.S. Wagner and W.C. Ellis, Appl. Phys. Lett. 4, 89 (1964)

* see corresponding article in this report for a more detailed motivation.

Cadmium Sulfide Nanowires: Lasing

C. Borschel, K. Sunter*, F. Capasso*, C. Ronning

* School of Engineering and Applied Sciences, Harvard University, Cambridge, USA

Introduction

Lasing activity has been observed in semiconductor nanowires of different materials [1,2]. The nanowires (NW) act as the optical cavity with their end facets working as partial mirrors due to the difference in refractive index compared to air/vacuum. At the same time, the nanowires act as the gain medium. In most experiments, the nanowires were pumped optically by a focused laser beam with above-band edge energy. Due to their small size, NW lasers feature highly localized monochromatic light sources, and are therefore very interesting to study coupling to other nanophotonic elements.

CdS is a semiconductor with a direct band gap of 2.42 eV (at RT), corresponding to light emission at 512 nm. This wavelength is interesting to study the coupling of lasing modes within the nanowires to plasmonic nanostructures: the cut-off diameter for waveguiding in CdS NW is about 150 nm. Ag or Cu nanoparticles (NP) with about the same diameter have plasmon resonances close to the CdS band gap.

It has been shown, that lasing in CdS nanowires is possible [3].

Experimental

CdS nanowires were grown in a horizontal tube furnace via the vapor-liquid-solid (VLS) mechanism.* The CdS nanowires grow in a high density with random orientation. In order to locate and address single NW for the lasing experiments, clean substrates were gently pressed face-down onto

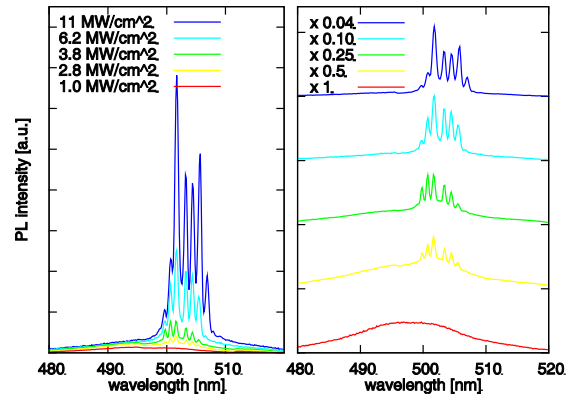


Fig. 1: PL spectra of a single CdS nanowire at different excitation power densities. Left: linear scale. Right: offset and stretched with indicated factors.

the growth substrates, resulting into the transfer of a small number of nanowires. The new substrate was covered with markers and a coordinate system allowing to locate the same nanowires in the optical setup and the electron microscope.

For optical pumping, a frequency-tripled pulsed Nd:YAG laser was employed (355 nm, 7 ns pulse length, <2 mJ pulse energy, 500 Hz repetition rate). Using a micro photoluminescence (μ -PL) setup, the laser beam was focused to a spot of a few μm^2 , allowing the excitation of selected single NW with very high power densities. The emitted photoluminescence spectra around the band gap were recorded as a function of excitation power. During the experiments, the samples were cooled down to temperatures between ~ 8 and 20 K.

Electron microscopy images of the same NW were taken in order to determine their length and size.

Results and Discussion

A series of near band edge PL spectra from a single CdS nanowire is illustrated in fig-

* For details see the article about CdS NW growth within this report.

ure 1. At low excitation density, a comparatively broad, featureless peak is observed

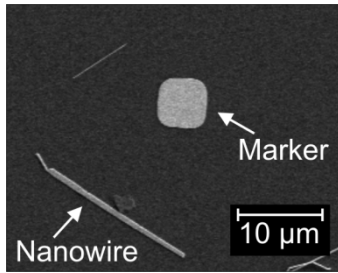


Fig. 2: SEM image of the nanowire of which the PL spectra in figure 1 are recorded.

(red line), originating from charge carrier recombination and corresponding near band edge emission. With increasing pump power, sharp lines emerge from the broad peak due to the excitation of Fabry-Pérot (FP) modes in the nanowire cavity. The fraction of light emitted within the sharp lines increases with respect to the underlying peaks and at very high power almost all light is in the FP modes.

The length of the nanowire is $\approx 20 \mu\text{m}$ as determined from the SEM image illustrated in figure 2. The mode spacing is consistent with the nanowire length and possible values for the refractive index and dispersion. However, an exact verification is not possible since the refractive index as well as the dispersion strongly change close to the band edge and are not known exactly for the experimental temperatures at the spectral position.

The output power of the nanowire cavity is measured by integrating the PL spectra. Figure 3 shows the output power of a single nanowire as a function of excitation power. At low excitation powers, the output power increases linearly. Above a threshold of approximately 2 to 3 MW/cm^2 , the output power is linear again but with an increased slope, which indicates lasing activity within the nanowire above this threshold. From figure 1 it can be seen that the Fabry-Pérot

modes start emerging in the PL spectra above this threshold.

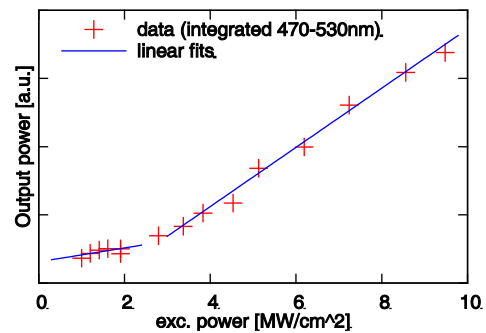


Fig. 3: Integrated PL spectra (\propto output power) of a single nanowire as a function of excitation power.

Conclusion

Fabry-Pérot modes are observed to be excited in single CdS nanowires upon intense optical pumping. The dependency of the output power from the pump intensity indicates the onset of lasing in the nanowires about a threshold of approximately 2~3 MW/cm^2 . These experiments show that the optical quality of the nanowires is sufficient for further experiments on coupling to plasmonic nanostructures.

Acknowledgement

For financial support, the authors thank the DFG (grant Ro1198/7-3), the DAAD (PPP travel grant), and the NSF (grant PHY 06-46094).

References

1. M.A. Zimmler, F. Capasso, S. Müller, and C. Ronning, *Semicond. Sci. Technol* 25, 024001 (2010)
2. S. Gradečak, F. Qian, Y. Li, H.-G. Park, and C. M. Lieber, *Appl. Phys. Lett.* 87, 173111 (2005)
3. R. Agarwal, C.J. Barrelet and C.M. Lieber, *Nano Lett.* 5, 917 (2005)

Ion beam induced nanoscaled surface structures on TiO₂

M. Fravventura, J. Sommerfeld, R. Niepelt, C. Ronning

Introduction

Titanium oxide (TiO₂) is well known as a basic material in medical and mechanical engineering. The coaction of roughening and smoothing during ion sputtering leads to characteristic nanopatterns on top of initially flat TiO₂ surfaces, thus giving an ability of tuning the physical properties of the surface without changing the chemical configuration. There have not been any reports of ion patterning on TiO₂ surfaces so far; in this article we will present ion beam patterned TiO₂ and demonstrate that the structuring process works in accordance to theory as well as other materials.¹

Experimental

TiO single crystalline and polycrystalline samples have been irradiated with 10 keV Xe⁺ ions under varying incident angles and fluences using the low energy implanter LEILA. The surface evolution has been investigated ex situ via AFM measurements.

Results and Discussion

As expected, the surface evolution depends strongly on the irradiation parameters. With the sputtering theory of P. Sigmund² and the constructive work of R. Bradley and J. Harper³ it is possible to understand and forecast the topography evolution of the surface with respect to the incidence angle and the ion fluence. For shallow incident angles, the theory predicts a 90° change in structural orientation. In figure 1 an angular dependent irradiation series at a fixed ion fluence is shown. For incidence angles of 70° and 75° ripple structures orientated perpendicular to the ion beam direction evolved. At 80° the surface presents elliptic grains with long axes perpendicular to the ion beam direction. Theory predicts that these structures are typically formed at an incident angle slightly below the critical angle where the orientation changes.

The fluence dependence of the surface evolution was investigated with irradiation series at fixed incident angles and fluences

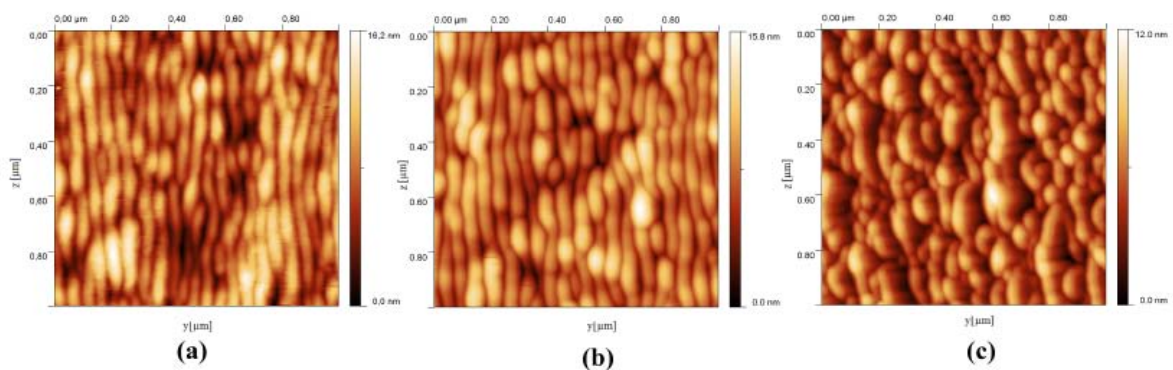


Figure 1: AFM images of TiO₂ samples sputtered at room temperature with 10 keV Xe⁺ ions and a fixed fluence of $\Phi = 3 \times 10^{17}$ ions/cm². Moving from the left to the right, the sample surfaces irradiated at 70°, 75° and 80° with respect to perpendicular incidence are shown. The direction of the incoming beam is indicated by the arrow in picture (c).

between 3×10^{17} and 7×10^{17} ions/cm². The theory predicts an exponential increase of the surface roughness for lower fluences and a power law scaling increase of the roughness and the wavelength above $\Phi \sim 10^{16}$ ions/cm². The surface roughness obeys a power law relation $RMS \sim \Phi^\beta$ with $\beta = 0,34$ (not shown here). In figure 2 the ripple wavelength evolution as a function of fluence is shown. The wavelength increases with soaring fluence; thus following a power law function $l \sim \Phi^\gamma$ with $\gamma = 0,19$. This behavior is in accordance to theory as well as sputtering studies on oth-

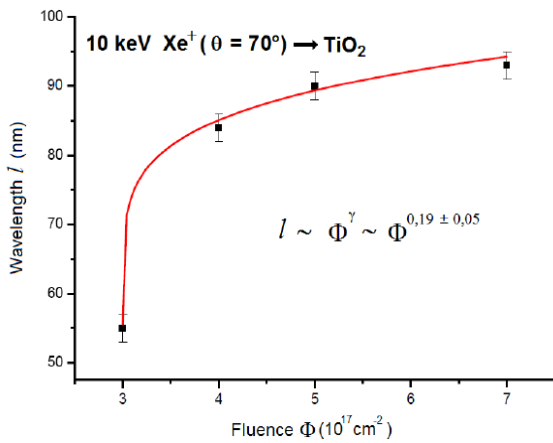


Figure 2: Plot of the ripple wavelength as a function of the ion fluence. The TiO₂ samples have been irradiated at room temperature at a fixed ion energy of 10 keV and a fixed incidence of angle 70°. The wavelength increases following a power law function $l \sim \Phi^\gamma$ with $\gamma = 0,19$.

er materials like silicon^{4,5}.

Conclusion

Patterning of TiO₂ via low energy ion sputtering was shown. The surface development is in accordance to theoretical predicts and experimental studies on other materials like Si, Ge and graphite.

References

1. M. Fravventura, *Ion-beam induced ripples on Si, TiO₂ and Ti surfaces*, Master thesis, Politecnico di Milano 2009
2. P. Sigmund, *Physical review*, 184, 383-416 (1969)
3. R. M. Bradley and J. M. E. Harper, *Journal of Vacuum Science & Technology A*, 6 (4), 2390-2395 (1988)
4. K. Zhang et.al., *Surface & Coatings Technology*, 203 (17-18), 2395-2398 (2009)
5. T. K. Chini et.al., *Journal of Physics: Condensed Matter*, 21, 1-22 (2009)

Biofunctionalization of ZnO nanowires and silicon nanoripples

J. Hönig, U.-C. Schröder, T. Schüler*, R. Möller*, J. Sommerfeld, C. Ronning

* *Institut für Photonische Technologien, Albert-Einstein-Straße 9, 07745 Jena*

Introduction

It is well known that nano sized structures and modified surfaces made their way into life sciences. Especially nanowires are widely discussed to be very suitable for biosensor applications.

To investigate the possibility to establish zinc oxide (ZnO) nanowires as well as ion beam modified silicon (Si) wafers for biomedical applications, we attached DNA on appropriate samples.

Experimental

The ZnO nanowires were grown via vapor liquid solid (VLS) mechanism [1] on Si in a high temperature furnace at 1350 °C, 150 mbar. The nanowires were transferred to a clean Si wafer by imprint. Their diameter, determined by scanning electron microscopy (SEM), was in the range of 200 nm at a length of 20 µm.

To create nanoscaled ripple nanopattern, Si wafers have been irradiated with 10 keV xenon ions under an angle of 70 ° (with respect to the surface normal) using the accelerator LEILA. The ripple formation is described elsewhere [2]. Via AFM the wavelength of the ripples was determined to be 60 nm.

After cleaning the samples by argon etching followed by an oxygen plasma activation of the dangling bonds at the surface, the wafers with the nanowires and the ripples were silanized in a toluene solution containing glycidyloxypropyl-trimethoxysilane (GOPS). Due to the use of catcher DNA the dye molecule

fluorescein isothiocyanate (FITC, $\lambda_{\text{ex}} = 495 \text{ nm}$) was attached which is necessary in order to control the connection of the DNA with the surface. For the fluorescence measurements we used a Carl Zeiss Axio Imager with a CCD camera. We took fluorescence pictures as well as dark field images of the same surface region and compared them. The ripple surface roughness measurements and cross sections were done with a Veeco Multi-Mode AFM with a Nanoscope 3 controller.

Results

In Fig. 1 the dark field image (a) of ZnO nanowires as well as the fluorescence image (b) are presented. The green and orange markings show three nanowires with intense fluorescence, whereas the blue ring indicates nanowires for which no luminescence could be observed. Due to the last point it can be concluded that the ZnO nanowires don't show luminescence by themselves. Consequently we assume that the DNA with the dye molecule actually attached to the green and orange labeled nanowires. Since the substrate was treated too, the background also exhibits some luminescence. However, according to Dorfman et al. [3] ZnO nanoplattforms increase the intensity of the emitted light of biomolecules. Therefore, we can clearly distinguish between substrate and nanowires.

Since there is no difference in the fluorescence images between the ripple structure surface and the background we

performed AFM measurements to receive evaluable results.

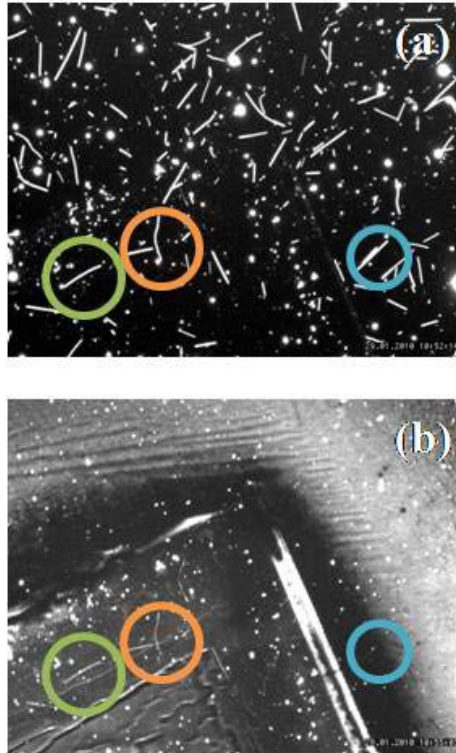


Fig. 1: Imprints with ZnO nanowires on a Si wafer. (a) shows the dark field image whereas (b) shows the fluorescence picture of the same position. The orange and green rings mark nanowires that show luminescence. No luminescence could be observed for the blue labeled nanowires.

The cross sections and roughness measurements of the ripples on Si wafers are shown in Fig. 2. The pictures (a) and the respective cross section (b) have been taken of the sample before biochemical treatment. The roughness is about $R_a = 0.1$ nm. Picture (c) and (d) show the same sample after the procedure. The cross section already indicates an increased roughening, which is confirmed by $R_a = 0.5$ nm. Because of the DNA strings connected to the dye molecules a roughening of the surface was expected. Therefore, we can conclude that the attachment of the DNA on the surface was again successful. Unfortunately the influence of the ripples could not be investigated up to now.

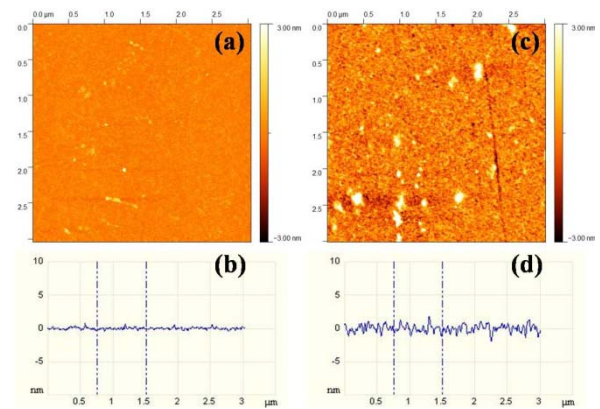


Fig. 2: AFM pictures of the same Si sample before (a) and after (c) biochemical treatment. (b) and (d) show the referring cross sections. Due to the attached DNA with the dye molecules on the surface the roughness clearly increased.

Conclusion

It appears as though it is possible to attach DNA on ZnO nanowires as well as on ion beam modified Si surfaces. Control experiments without DNA and only with the dye molecule on our samples are already in process. To clarify the intensity of the observed fluorescence, the occurrence of the DNA attachment and the influence of ripple properties, further investigations are projected.

References

- [1] R. S. Wagner und W. C. Ellis: *Vapor-Liquid-Solid Mechanism of Single Crystal Growth*, Applied Physics Letters, **4**, 89-90 (1964).
- [2] R. M. Bradley und J. M. E.: *Theory of ripple topography induced by ion bombardement*, Journal of Vacuum Science & Technology A, **6**, 2390-2395 (1988).
- [3] A. Dorfman, N. Kumar und J. i. Hahm: *Highly Sensitive Biomolecular Fluorescence Detection Using Nanoscale ZnO Platforms*, Langmuir, **22**, 4890-4895 (2006).

Carbon-assisted growth and characterization of aligned ZnO-nanowires

M. Kozlik, C. Borschel, C. Ronning

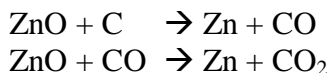
Introduction

Zinc oxide nanowires (ZnO NW) are promising candidates for usage in many applications [1,2]. Due to its wide band gap (ca. 3.4 eV) and the large exciton binding energy (63.1 meV) ZnO is an interesting material for light emitting diodes (LED) [3]. In ZnO NW, at high pumping energies lasing can be observed [4]. Aligned ZnO NW would be preferred for lasing applications because the emitted light is guided to the end of the wire [5] where oriented emission could be investigated.

It is known that hexagonal ZnO NW grow along the c-axis [6]. Therefore aligned epitaxial growth should be possible on substrates with lattice constants matching the ZnO a-lattice constant (3.25 Å).

Experimental details

The ZnO NW synthesis took place in a horizontal 3-zone-tube-furnace via VLS-mechanism [7]. The source material was placed on a crucible in the centre of the furnace at a temperature of 1050°C. The material consists of a stoichiometric mixture of ZnO powder (Alfa Aesar: 99.99 %) with carbon (Alfa Aesar: 99.99 %) for carbon-assisted growth (CAG) [8]. The aim of CAG is to reduce the sublimation point by the reduction of ZnO (sublimes at 1800°C) to Zn (Boiling point at 907°C):



The samples were placed at a distance of 25 cm downstream from the source at a temperature of ca. 500°C. After cleaning in an ultrasonic acetone bath, rinsing with isopropyl and drying in flowing dry nitrogen, a 5 nm thin gold layer acting as catalyst was

deposited on the substrate via sputter coating. Different substrates were used, representing different lattice mismatches. The growth time was 30 min. at a pressure of 7 mbar and a gas flow of approx. 20 sccm (10 sccm Ar⁺ 10 sccm O₂).

Results and discussion

The ZnO NW were characterised in TEM (see Fig. 1). High resolution TEM

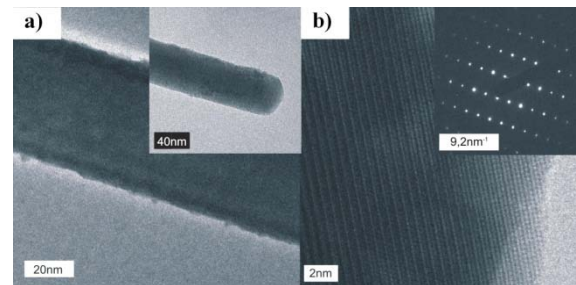


Fig. 1: The bright field TEM-image (a) shows the diameter of the ZnO NW. The HRTEM (b) and the SAED (inset) illustrate the crystalline structure. The scanned region is single crystalline and the spot distances prove growth along the c-axis.

(HRTEM) and selected area electron diffraction (SAED) show the high crystalline structure. The distances between the spots in the SAED prove the growth along the c-axis. In connection with the energy dispersive x-ray spectroscopy (EDX, see Fig. 2) the nanowires consists of single crystalline hexagonal and stoichiometric ZnO.

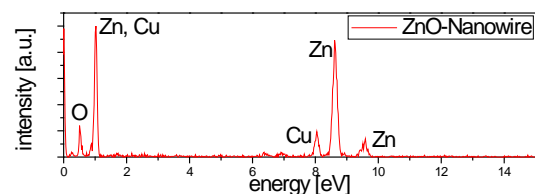


Fig. 2: The EDX-spectrum taken in the TEM shows that the nanowire consists of zinc and oxygen. The copper signal originates from the grid holder.

The scanning electron microscope (SEM) images show the orientation of the ZnO NW in respect to the substrate. The lattice

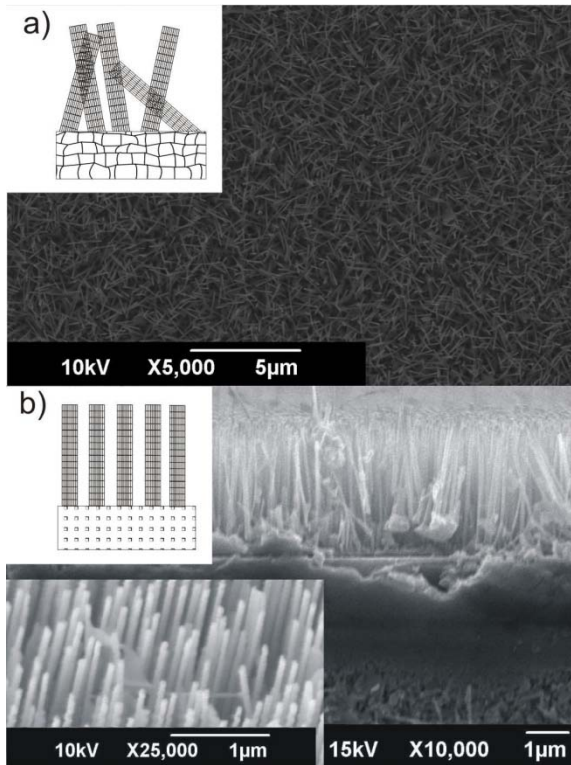


Fig. 3: The SEM images show ZnO-nanowires grown on Si (a) and on 6H-SiC (b). The schemes in the insets illustrate the growth on substrates with large (a) and small (b) lattice mismatch

mismatch between ZnO and Si is quite large ($f_{Si} = 40.1\%$). This fact yields to diffuse oriented ZnO-NW (see Fig. 3a). Substrates with a small lattice mismatch like 6H-SiC ($f_{6H-SiC} = 5.2\%$) show epitaxial grown ZnO NW with an orientation perpendicular to the substrate surface (see Fig. 3b).

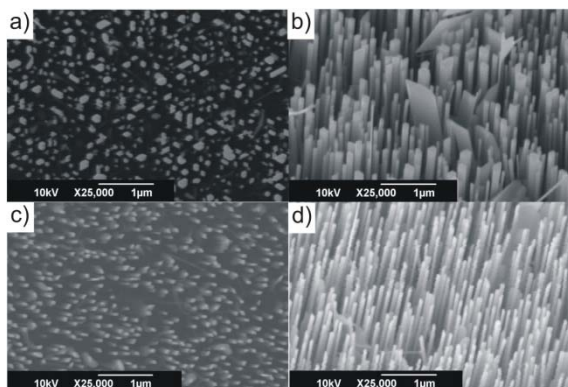


Fig. 4: The SEM images show ZnO-nanowires grown on AlN (a: top view, b: 25° tilted) and on 6H-SiC (c: top view, d: 25° tilted). Due to the small lattice mis-match, synthesis of well aligned ZnO-nanowires is possible.

The alignment of ZnO NW could be observed both on 6H-SiC as well as on AlN (see Fig. 4). In top view there are just spots, representing the head of the wires (see Fig. 4a and 4c). The wires turn up by tilting the sample (see Fig. 4b and 4d). The parallel orientation shows clearly that all wires grow in the same direction perpendicular to the substrate.

Conclusion

The CAG-equipment could be used for synthesis of epitaxial aligned ZnO-NW. TEM-investigations proved the growth along the c-axis. Therefore substrates not matching the a-lattice constant of ZnO yield in diffuse nanowires growth. Whereby substrates, with a lattice mismatch around 5 %, yield in vertical aligned ZnO NW.

References

- [1] M. Kaur et al., Journal of Nanoscience and Nanotechnology **9** (2009) 5293–5297.
- [2] C.-H. Chen et al., Chem. Phys. Lett. **476** (2009) 69–72.
- [3] X.-M. Zhang et al., Adv. Mat. **21** (2009) 2767–2770.
- [4] M. A. Zimmler et al., Appl. Phys. Lett. **93** (2008) 0511011–0511013.
- [5] T. Voss et al., Nano Lett. **7** (2007) 3675–3680.
- [6] K Black et al., Nanotech. **21** (2010) 045701.
- [7] R.S. Wagner et al., Appl. Phys. Lett. **4** (1964) 89.
- [8] J. Wang et al., Mater. Lett. **59** (2005) 2710.

Spatial resolved cathodoluminescence on semiconductor nanostructures

S. Geburt, C. Borschel, M. Gnauck, C. Ronning

The JEOL JSM-6490 scanning electron microscope was upgraded with a Gatan MonoCL3+ cathodoluminescence system [1], which provides unique possibilities for spatial resolved luminescence experiments on nanostructures and solar cells.

The electron beam interacts with the sample in various ways: The secondary electrons are used for imaging of the sample surface. In suitable samples like semiconductors, light is emitted upon electron beam irradiation (cathodoluminescence, CL). The light is collected by a parabolic Al mirror above the sample and guided into the entrance slit of a 300 mm Czerny-Turner-Monochromator. The photons are dispersed at the grating and focused on the exit slit. A 1200 l/mm grating sensitive in the UV-VIS range is installed as standard, the second grating on the turret can be exchanged to suit the spectral range and the resolution needed for the experiments. The wavelength separated photons are detected either by a high sensitive photomultiplier (250-900 nm) or by a wide range IR photomultiplier (300-1650 nm). For fast spectra acquisition, a flip mirror is inserted in the monochromator and the photons are detected by a back-illuminated CCD camera (200-1100 nm). The minimum resolution of the CL system is below 0.1 nm (< 1 meV).

A liquid helium cooled cryostage is available to realise sample temperatures between 7 K and room temperature. A vacuum transfer system allows fast sample exchange even at deep temperatures. A fast electron beam blanker is installed at the electron column and will provide the possibility for time resolved CL measurements in the future.

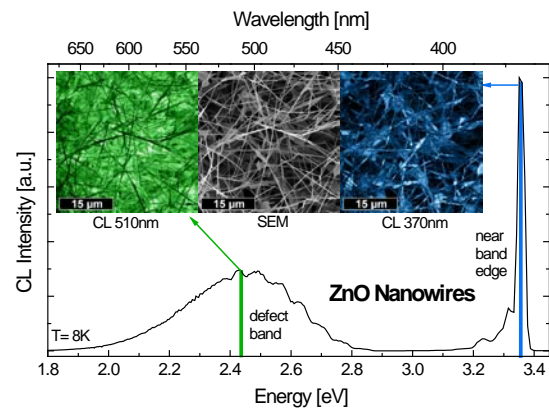


Fig. 1: Cathodoluminescence (CL) spectrum of as-grown ZnO nanowires. The insets show the SEM image and monochromatic CL images at 370 nm and 510 nm. The ZnO nanowires show an intense near band edge luminescence around 370 nm. At 510nm, the nanowires appear dark, therefore the defect band luminescence originates from the underlying nanostructures.

Experiments

The great possibilities of the CL system are used for the optical analysis of semiconductor nanowires. An example is shown in Fig.1. The spectrum shows the cathodoluminescence of an as-grown ZnO nanowire sample. The intense near band edge luminescence was recorded at 3.37eV [2]. Between 2.0 to 2.8 eV, the emission of the green defect band [3] could be detected. The ZnO nanowires usually have a very high crystal quality confirmed by TEM measurements [4], therefore the intense emission of the defect band is unusual. On the monochromatic CL images recorded at 370 nm (see Fig. 1 inset), it could be found that the nanowires show an intense emission of the near band edge luminescence. At 510 nm, the nanowires appear dark, but the underlying ZnO structures show a bright emission. Therefore, the defect band luminescence originates from the ZnO structures underneath the nanowires.

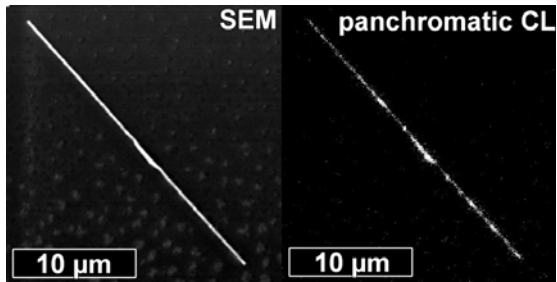


Fig. 2: SEM and panchromatic CL image of a Europium implanted ZnO nanowire. After implantation and annealing, the nanowire still shows an intense light emission upon electron beam irradiation.

ZnO nanowires from an as-grown sample were transferred to a clean Si substrate and doped with Europium by ion implantation. A homogenous concentration of 3 at% was realised up to a depth of 70 nm, the maximum implantation depth of 150 nm matches the diameter of the nanowires. The implantation damage was reduced by annealing at 700°C in air for 30 min. Fig. 2 shows the SEM and the panchromatic CL image of an implanted nanowire. In the panchromatic mode, the light is guided directly to the detectors and the overall intensity is measured. The nanowires show a bright light emission even after the ion implantation.

The high sensitivity of the CL setup enables the measurement of single nanowires as shown in Fig. 3. The plot shows the normalised CL spectra of an unimplanted ZnO nanowire, an Europium doped nanowire and the implanted Si substrate. The luminescence of the unimplanted nanowire is characterised by the intense near band edge luminescence around 3.37 eV and a very low defect emission. The band edge luminescence of the Europium implanted nanowires is lower and broader compared to the unimplanted wires. The low defect luminescence demonstrates the effective implantation damage recovery by annealing. At 2.0 eV, the intra-4f-luminescence of Eu^{3+} (${}^5\text{D}_0 \rightarrow {}^7\text{F}_2$) [5] appears in the spectra

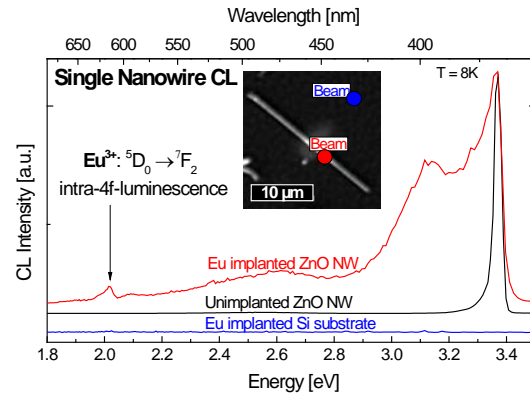


Fig. 3: CL spectra of single ZnO nanowires demonstrate the outstanding sensitivity of the CL system. The unimplanted ZnO nanowires show an intense and sharp near band edge luminescence. The doped nanowires show intra-4f-luminescence of Europium.

revealing the successful optical activation of the dopant.

The implanted substrate does not show any CL signal, therefore it is confirmed that the Eu-intra-4f-luminescence originates from the doped nanowires.

Conclusion

ZnO nanowires could be successfully doped with Europium. The nanowires are optical active after implantation. CL spectra of single nanowires show the intra-4f-luminescence of Europium.

Acknowledgements

The cathodoluminescence setup was financed by the Thüringer Ministerium für Bildung, Wissenschaft und Kultur under Project B 715-08010. The CCD camera upgrade was financially supported by the Federal government within the Konjunkturpaket II, Oct 2009.

References

- [1] www.gatan.com
- [2] Meyer et al., Phys. Stat. Sol. (b) 241 (2001), p. 231-260
- [3] Müller et al., J. Appl. Phys. 104 (2008), p. 123504
- [4] S. Müller, Masterthesis, University of Göttingen, 2005
- [5] Geburt et al., JNN 8 (2008), p. 244-251

Four tip measurement station Süss EP6 DC

S. Milz, M. Gnauck, R. Niepelt, C. Ronning

A new analytical probe system for electrical DC measurements has been set up at the IFK. It allows electrical characterization and failure testing via contacting samples with up to 4 precisely controllable metal tips (tip radius: $7\mu\text{m}$). The probe station EP6 from Süss MicroTec (Fig. 1) is equipped with an optical stereo microscope. Samples of up to 150mm in diameter can be loaded and fixed via vacuum. The sample holder can be rotated along the z-direction and shifted in x-, y-direction in a range of $\pm 150\text{mm}$. The height adjustment range is 10mm. The probehead platen can be moved about 40mm in z-direction and has a contact/separation stroke of 0,2mm. The four PH110 probeheads can be moved in any direction with an accuracy of some μm [1].

An electromagnetic shield was built at the workshop. The metallic box can be placed on the table covering the whole probe station and allowing low noise measurements in the pA-range. The sample and the tip positions can easily be changed after opening the door of the shield. Apart from measuring low currents, the shield can also be used to measure samples without any light.



Fig. 1: Süss EP6 DC probe station with stereo microscope (magnification: 15x-100x, fiber optical light ring, 1,3MPixel USB-CCD-camera).

For electrical measurements, the setup displayed in Fig. 2 can be used. I-V-characteristics can be measured with the Keithley SMU 237 in two- or four-point geometry. The range of the source-measure-unit is 0,1mV-1100V and 10fA-100mA, allowing resistance measurements up to a few T Ω at a moderate voltage. A gate voltage can be applied with the Keith-

ley 230 Programmable Voltage Source and small currents can also be measured with

A software written in Labview allows convenient data recording, visualization and export.



Fig. 2: Electrical measurement setup consisting of source-measure-unit, nanovoltmeter, programmable voltage source and picoammeter. All devices can be controlled with Labview via the IEEE-interface.

the Keithley 485 Picoammeter.

References

- [1] SUSS MicroTec, COMPLETE DC PROBING PACKAGE EP6 DC, Data Sheet, 2008.

Photoluminescence investigations on polycrystalline Cadmium Telluride Solar Cells

C. Kraft, M. Hädrich, U. Reislöhner, H. Metzner, P. Schley^a and R. Goldhahn^a

^a*Institut für Physik, Technische Universität Ilmenau, PF 100565, 98684 Ilmenau, Germany*

Polycrystalline cadmium telluride (pc-CdTe) is a promising material for low-cost photovoltaic power generation. Conversion efficiencies of more than 20% are predicted by either increasing or decreasing the low intrinsic doping level of about $2 \times 10^{14} / \text{cm}^3$ [1]. Hence, knowledge about the defect structure of CdTe is very important. To learn more about certain defects of pc-CdTe, PL measurements are a common method. Much research has been done in the last decades especially on single crystal CdTe, but the PL-spectra of pc-CdTe are still not well understood.

A typical CdTe-PL spectrum can be separated into 3 regions: (i) the 1.59 eV band which is correlated to excitonic transitions, (ii) the 1.55 eV band which originates from free to bound transitions and (iii) the 1.45 eV band and which is believed to originate from a complex of V_{Cd} and a donor at a tellurium site, e.g. chlorine (Cl_{Te}) [2]. However, the 1.45 eV peak often appears in as-grown samples described in the literature [2, 3].

Chlorine is a common element to react with CdTe for solar cell applications. A significant increase of the conversion efficiencies can be achieved by heating them in an ambient of chlorine containing compounds such as cadmium chloride (CdCl_2). This process is not understood in detail and has previously been investigated by PL-measurements on pc-CdTe for solar cell application [2, 3] and for the case of HCl in [4] but the role of chlorine in CdTe has not been solved satisfactorily.

We measured the PL of an untreated sample to identify the energetic positions and the origins of the most prominent transitions and analysed the changes that occur in samples that are annealed with and without a chlorine containing compound. In this context gaseous HCl and non-toxic NaCl as alternatives for a treatment with CdCl_2 were investigated.

The samples were produced by the close space sublimation method in our baseline as a $10 \times 10 \text{ cm}^2$ TEC-7/FTO/CdS/CdTe layer system as described in [5].

After the thermal treatment, the PL measurements were performed in a helium cryostat. The temperature was varied between 5 and 80 K; the laser power was varied between 2 and 200 mW. A laser energy of 1.7 eV was chosen, which is shortly above the band edge of CdTe (1.606 eV at 5 K). Figure 1 shows the PL spectra of the differently treated samples at 5K.

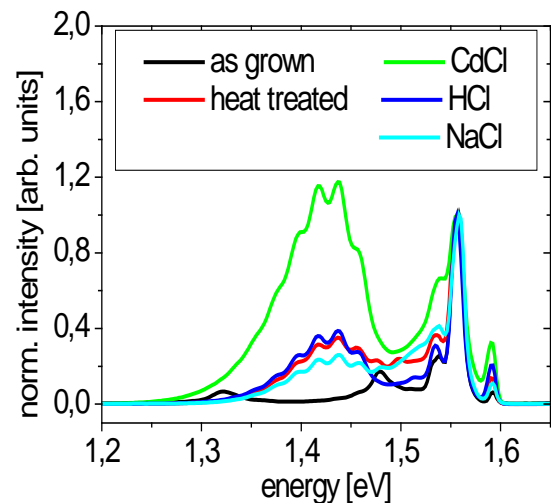


Fig. 1: PL spectra of the differently treated samples

The spectra are normalised to the 1.56 eV-peak. The 1.45 eV-peak can be clearly seen in all samples except for the untreated one. It is accompanied with several phonon replica indicating a good crystalline quality. Our measurements show that the PL-intensity in the 1.45 eV region, in contrast to other measurements on polycrystalline CdTe, is close to zero at the as-grown sample. In contrast to the latter, the PL of samples with post-deposition treatment shows an intensive peak, even when no chlorine was involved, which proves the assumption, that it is not from an intrinsic defect.

The peak at 1.55 eV can be divided into two separate peaks at 1.553 and 1.559 eV at a higher resolution. A dramatic decrease of this band with increasing temperature is observed wherein the 1.559 eV-peak is decreasing stronger. Based on the results of power and temperature dependent measurements, we can propose that both peaks are in principle transitions between free and bound states with different defect concentrations, since they show a different behaviour with respect to the varied measurement parameters.

Finally, the excitonic band which can be clearly seen at 1.59 eV has been analysed for the different post-growth treatments. One result is shown in Fig. 2.

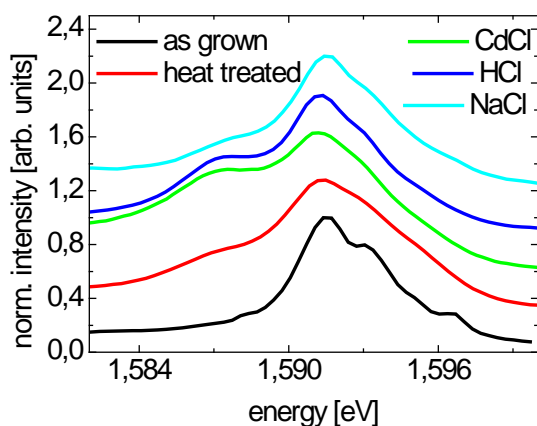


Fig. 2: Excitonic band of differently treated samples (spectra are shifted for clarity)

Obviously the spectra can be separated into several different peaks, especially in the case of the untreated sample. They are believed to be related to the transition of a free exciton at 1.596 eV, a donor bound exciton at 1.593 eV, and an acceptor bound exciton at 1.591 eV, which would be in good agreement with measurements on single crystal CdTe [6].

By analysing our results, we were able to propose a defect model which is containing two intrinsic donor and acceptor states. Our measurements are the first to present a PL spectrum of an as-grown polycrystalline CdTe sample for solar cell applications in without a peak at 1.45 eV. This proves that this peak is due to post deposition treatment. The kind of post-deposition treatment has no influence on the energy of the measured PL band and the occurrence of the 1.45 eV defect band but is strongly affecting its intensity, especially in the case of the CdCl₂ treatment.

This work was supported by the Bundesministerium für Umwelt, Naturschutz und Reaktorsicherheit (BMU).

References

- [1] J.R. Sites, J. Pan, *Thin Solid Films*, 515 (2007), 6099.
- [2] D.P. Halliday, J.M. Eggleston, K. Durose, *Journal of Crystal Growth* 186 (1998) 543-549.
- [3] D.P. Halliday, J.M. Eggleston, K. Durose, *Thin Solid Films* 322 (1998) 314-318.
- [4] M.A. Hernandez-Fenollosa, D.P. Halliday, K. Durose, M.D. Campo, J. Beier, *Thin Solid Films* 431-432 (2002) 176-180.
- [5] M. Hädrich, N. Lorenz, H. Metzner, U. Reislöhner, S. Mack, M. Gossila, W. Witthuhn, *Thin Solid Films* 515 (2007) 5804-5807.
- [6] P. Horodysky, R. Grill, P. Hlidek, *Phys. Stat. Sol.* 243 (2006) 2882-2891

Design of a High Vacuum Chamber for Cadmium Telluride Evaporation and Doping

C. Kraft, M. Hädrich, U. Reislöhner and H. Metzner

Cadmium telluride (CdTe) solar cells are known to have a theoretical limit of 30% conversion efficiency, if one considers the band gap of about 1.5 eV only. Under realistic conditions efficiencies of more than 20% have been simulated by increasing the p-type doping level of about $2 \times 10^{14} / \text{cm}^3$ up to more than $10^{17} / \text{cm}^3$ [1]. This doping could be accomplished with group-V or group-I elements on a tellurium or a cadmium site, respectively. Thus, the open-circuit voltage which is directly proportional to the efficiency of a solar cell could exceed 1000 mV. Compared with the current world record of 845 mV [2], the conversion efficiency could be increased relatively by more than 20%. However, the doping of CdTe is difficult. For example: i) the dependence of the electronic properties of highly mobile atoms on their position in the crystal lattice, ii) the limitation of the doping efficiency by self compensation processes or iii) short circuits due to grain boundary diffusion in the polycrystalline material.

By calculations [3] it was predicted, that the group-V elements nitrogen, phosphorus, arsenic, antimony and bismuth on a tellurium site act as shallow acceptors with energy levels of 10 to 300 meV above the valence band (increasing with the atomic number). According to Ref. [3], the doping should be done in non-equilibrium processes such as ion implantation. No compensating defects should limit this way of p-doping (as long as no annealing occurs).

Nitrogen and phosphorus are regarded as the best candidates for p-type doping of CdTe. Layers which were grown by mo-

lecular beam epitaxy were already successfully doped by those and other group-V elements [4-6]. However, a confirmation of the doping effects appears to be missing in most cases.

As non-equilibrium process, ion implantation is indeed an excellent method for doping of CdTe, but for an industrial application it may be too expensive. The existing close space sublimation (CSS) method which has been used so far [7] is not suitable for this purpose as well, since it seems impossible to apply the required doping sources between crucible and substrate. The development of a new evaporation system based on both the well-known configuration of our existing CSS chambers and molecular beam epitaxy sources was chosen as an alternative.

The specification of the new system should contain a high rate of layer growth, a high yield of the evaporated material and a high homogeneity of the CdTe material on the substrate. Furthermore, besides the deposition of the CdTe the adding of cadmium for creating tellurium vacancies (and vice versa) and the evaporation of the doping material should be possible simultaneously. High homogeneity and a high material yield are conflicting conditions. According to the Knudsen model and a geometry which could be realised in the desired chamber, a material yield of 5.9% and homogeneity over the substrate of 88.6% (at the edges of the substrate) can be calculated. To avoid both the low material yield and the low homogeneity, a cone-shaped top on the Knudsen cell is proposed in order to get a

higher homogeneity and material yield. The proposed design is shown in figure 1.

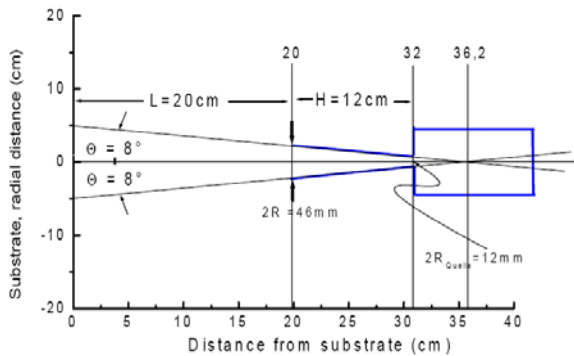


Fig. 1: Exemplary design for an evaporation source with a cone-shaped top

The calculation of the homogeneity profile of a conical source is shown in figure 2.

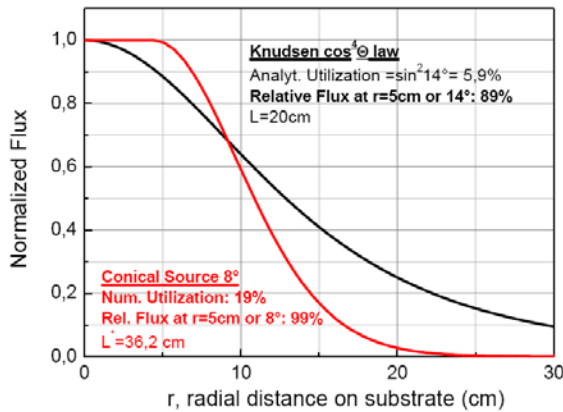


Fig. 2: Calculated evaporation profiles without (black) and with (red) a cone-shaped top

We expect that the conical top can reach a material yield which is three times as high as with an ideal Knudsen cell, while the homogeneity on the substrate is excellent, too. Additionally, the absolute rate of evaporation, which in cylindrical geometries is limited by the Clausing factor, is important. The Clausing factor can be understood as the probability that a molecule passes the aperture and is proportional to the relation of the length to the radius of the crucible. For our configuration it is difficult to make concrete statements for the Clausing factor, but an ideal lower aperture radius of the conical crucible could be estimated to about 9mm. For reliable values

concerning homogeneity, material yield and absolute evaporation rate, detailed Monte Carlo simulations for a certain source geometry were available. Our geometry arranges 6 doping sources around a central CdTe source, in which the central source aims perpendicular to the substrate and the doping sources have an off-axis angle of 20°. The central source is configured as a dual filament source which evaporates the CdTe base material. The doping sources provide the elements nitrogen (by using a plasma source), phosphorous, arsenic and antimony as group-V doping material as well as cadmium and tellurium to vary the stoichiometry of the CdTe. The doping chamber allows us to incorporate those elements during the growth of the CdTe layer in a co-evaporation process.

In this way, the new CdTe doping chamber (CATDOC) is designed to produce group-V doped CdTe layers in an industrially realisable process.

The described setup was funded by the Bundesministerium für Umwelt, Naturschutz und Reaktorsicherheit (BMU) as part of the project „CdTe Solarzellen hoher Effizienz für eine verbesserte Modul-Produktionstechnologie.“

References

- [1] J.R. Sites, J. Pan, *Thin Solid Films*, 515 (2007), 6099.
- [2] X. Wu, J.C. Keane, R.G. Dhere, C. DeHart, D.S. Albin, A. Duda, T.A. Gessert, S. Asher, D.H. Levi and P. Sheldon, *17th European Photovoltaic Solar Energy Conference, Munich, Germany, 22-26 October 2001, Proceedings* (2001), p. 995.
- [3] Su-Huai Wei, B.S. Zhang, *Phys. Rev. B* 66 (2002) 155211.
- [4] T. Baron, K. Saminadayar, N. magnea, J. Fontenille, *Journal Applied Physics* 83 (1998) 1354.
- [5] H.L. Hwang, K.Y.J. Hsu, H. Y. Ueng, *Journal Crystal Growth* 161 (1996) 73.
- [6] Y. Hatanaka, M. Niraula, A. Nakamura, T. Aoki, *Applied Surface Science* 175-176 (2001) 462.
- [7] M. Hädrich, N. Lorenz, H. Metzner, U. Reislöhner, S. Mack, M. Gossila, W. Witthuhn, *Thin Solid Films* 515 (2007) 5804-5807.

Implementation of a new rapid thermal annealing furnace.

C. Wolf, L. Hentschel, M. Oertel, H. Metzner

In 2009 a furnace for rapid thermal processing from LPT-Thermprozess GmbH was installed at the Institute of Solid State Physics at the Friedrich Schiller University Jena. Fig. 2. shows this Furnace. The device was acquired in order to accomplish annealing procedures under certain atmospheric conditions (e.g. inert gas atmosphere or vacuum) and to perform thermal processes with high heating rates up to 100 K/s or even up to 250 K/s for thinner substrates. For example a non-vacuum selenization of CIS-solar cells with high heating rates is particularly attractive for industrial implementation, as it would cause much lower investment costs for a manufacturer because expensive vacuum pumps are not necessary and cycle times of the production can be kept short.

Another important application is the post-growth activation of CdTe layers for solar cells in chlorine atmosphere.

Fig. 1 shows a sketch of the furnace chamber. The process chamber (1) consists of 8-mm-thick quartz glass which is suitable for high temperature processes. The chamber has a width of 13 cm and a height of 2.5 cm which allows processes on substrates with



Fig. 1: The RTP sintering furnace TM100BT: In the lower part the reaction chamber and the gas flow controller, in the upper part the Eurotherm is arranged.

an area of up to 10 x 10 cm². At the rear of the chamber a Pfeiffer full range pressure sensor, a pressure relief valve and the exhaust pipe are mounted on a small flange (2). The front end of the chamber is sealed by a water-cooled lockable door using a rubber gasket (3). The door (4) also serves as a charger, since it is held in the substrate holder (5) with a pinch seal. The entire substrate holder is made of quartz glass and can be easily exchanged in order to perform experiments on other substrates. Two encapsulated thermocouples are led out of the chamber. They can be positioned anywhere on the sample and below the substrate holder, and thus allow a relatively direct temperature measurement in the chamber.

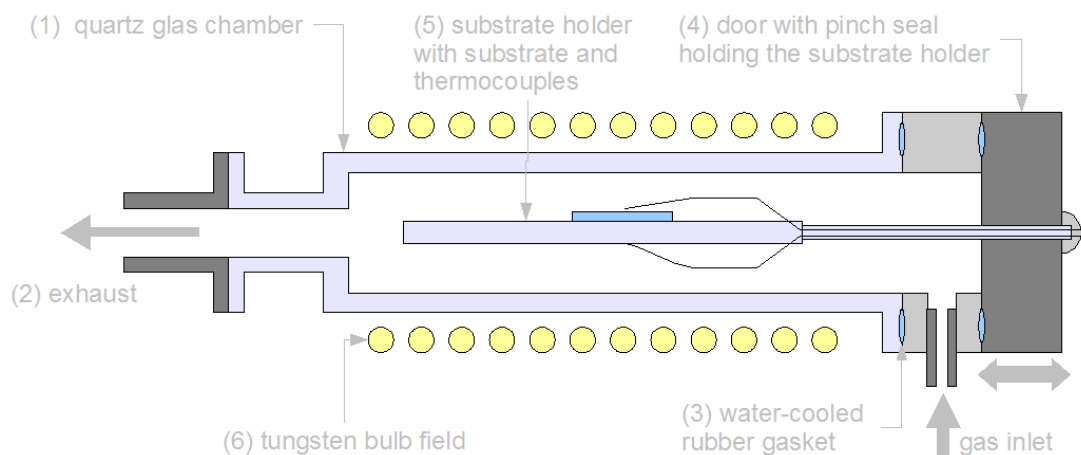


Fig. 2: Sketch of the chamber of the TM100BT

The high temperature ramps are achieved by separately adjustable bulb fields (6) above and below the chamber with 12 tungsten halogen lamps of type Osram 1500 W, which can be replaced separately in case of a defect. The bulb fields and the chamber design allows a homogeneous heating of the substrate up to a temperature of 1200°C. To achieve the desired temperature, the power is controlled by a Eurotherm controller (type 3504). Temperatures can be regulated precisely in a range of about ± 0.5 K with the actual configuration. The assignment between the bulb control and the temperature measurement can be changed in the Eurotherm. Thus, the bulb fields can e.g. also be regulated in accordance with the respective opposite thermocouple.

The processing in the furnace can be carried out either in vacuum or under a controlled inert gas atmosphere. To evacuate the chamber, a diaphragm pump is connected in order to create a vacuum with a residual pressure of 3 mbar in the chamber. The pump is chemically resistant and is thus not corroded by any remaining material in the exhaust. A stainless steel water-cooled condenser and an activated carbon filter in the exhaust pipe reduce the contamination of the pump to a minimum. A throttle valve between the pump and the condenser allows to reduce the pumping power. So, with the flow regulator, a controlled pressure in the chamber can be achieved. But even without a constant flow, an atmospheric pressure can be maintained over a certain period of time in the chamber.

The high heating rate is of particular interest for the selenization of CuIn-precursors to CuInSe₂ absorbers for thin film solar cells. High heating rates are necessary to avoid volatile indium-selenides in a temperature range from 350 to 400°C, leading

to a wrong stoichiometry and defects in the absorber. This effect is described in [1]. So, in a first experiment series in the new furnace, a selenization process of CIS solar cells in a non-vacuum process similar to the one described in [2], was reproduced. Therefore CuIn precursors, which were prepared with conventional sputtering techniques in our Pfeiffer sputter coater (installed in 2008 [3]), were annealed in a selenium containing atmosphere under continuous argon flow. First absorbers for CIS thin film solar cells were produced. Homogeneity and stoichiometry were checked with a scanning electron microscope (SEM) and energy dispersive X-Ray spectroscopy (EDS). The analysis indicated that there is still need for improvement in homogeneity. The desired stoichiometry (Cu/In/Se = 1/1/2) has already been achieved.

Compared to the selenization procedures in the ULS400 (described in [3]) we are now able to perform selenizations in inert gas atmosphere with steeper heating ramps.

In further experiments absorbers of CdTe solar cells will be thermally post-treated in the furnace. Compared to the activation described in [4], especially the high heating rate and the defined atmosphere (e.g.: N₂) will be in the focus of the investigations.

References

- [1] V. Alberts, J. H. Schön and E. Bucher; Journal of applied physics (1998) Vol84 #12
- [2] F. Kurdesau, M. Kaelin, V.B. Zalesski, V.I. Kovalewsky, Journal of Alloys and Compounds 378 (2004) 298–301
- [3] M. Oertel, J. Haarstrich, C. Wolf, T. Hahn and H. Metzner; Institute of solid state physics annual report 2008
- [4] C. Löffler, M. Hädrich, C. Kraft, H. Metzner, U. Reislöhner, W. Witthuhn; Institute of solid state physics annual report 2007

Selenium vapour flux control by measuring the selenium beam equivalent pressure

M. Oertel, J. Haarstrich, C. Wolf, J. Cieslak, H. Metzner, and W. Wesch

In terms of reproducibility and improvement of the performance of Cu(In,Ga)Se₂-thin film solar cells, it is absolutely necessary to control the selenium amount provided during the absorber growth process [1,2]. Also, in terms of specific band gap engineering, promising results were achieved by controlling the selenium flux during different states of the absorber layer growth [3,4].

Evaporating selenium in a high vacuum system with an evaporation cell is a common technique to provide a desired selenium amount [5]. In theory, the cell temperature determines the selenium vapour pressure and so the selenium flux. Unfortunately, due to geometry and inhomogeneities in temperature of the cell, in practice, the flux depends on the charging level of the cell. So, especially in long term evaporation, the flux has to be controlled and adjusted during the process.

Our sequential CIGS absorber layer process is described elsewhere in principal [6]. For selenization we now use a high vacuum chamber with an evaporation source. Hence, we control the selenium rate by beam equivalent pressure. To this end, we

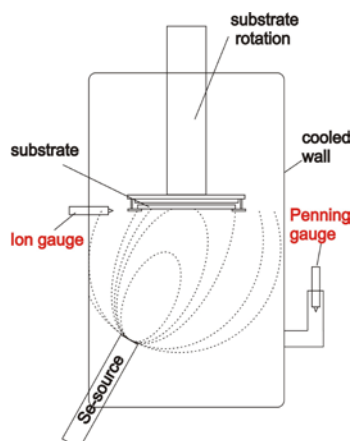


Fig. 1: sketch of the high vacuum gauge arrangement for measurement of the beam equivalent pres-

use an arrangement of two high vacuum gauges in the chamber as shown in Figure 1. Due to its position the ion gauge measures a pressure proportional to the selenium vapour flux added to the background pressure. The penning gauge only measures the background pressure. By subtracting the penning gauge measurement from the ion gauge measurement we obtain pressure Δp which is proportional to the selenium flux. As shown in Figure 2, using Δp , we can directly measure the selenium vapour rate.

By the use of this method we determined the absorber layer process window relating to the minimal and maximal Se vapour rate allowed for the process.

To this end, we did a series of experiments with CuIn- as well as CuIn_{0,75}Ga_{0,25}-alloys called precursors on molybdenum coated soda lime glass using a typical temperature profile for the selenization process as shown in Figure 3. Only Δp was changed between each run. The samples were analysed by scanning electron microscopy (SEM) and energy dispersive x-ray spectroscopy (EDX).

The lower process limit at a Δp of $1,0 \cdot 10^{-5}$ mbar is characterised by an loss of indium during the selenization, which

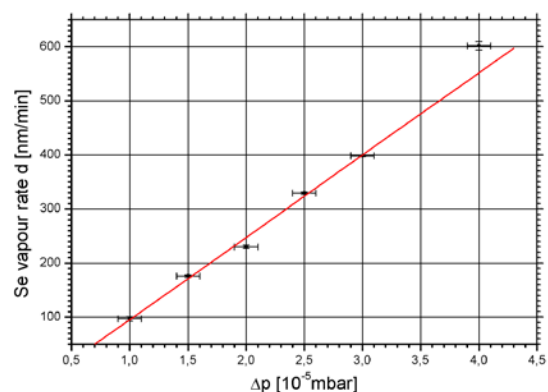


Fig. 2: Correlation between Δp and the selenium vapour rate

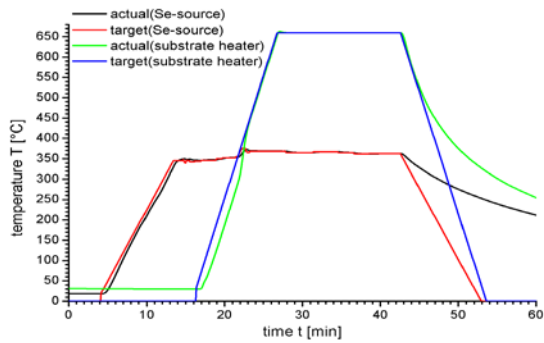


Fig. 3: Typical temperature profile of the selenization process

is higher in $\text{CuIn}_{0,75}\text{Ga}_{0,25}\text{Se}_2$ -absorbers than in pure CuInSe_2 -absorbers. This is explained by a shift of the reaction equation to volatile InSe -compounds at low selenium partial pressures. Also, this loss of indium comes along with the creation of pinholes in the absorber films (Figure 4).

The upper process limit is characterised by a peeling off of the absorbers from the molybdenum coated soda lime glass. CuInSe_2 -absorbers peel off at $3,5 \cdot 10^{-5}$ mbar. $\text{CuIn}_{0,75}\text{Ga}_{0,25}\text{Se}_2$ -absorber peel of at $2,5 \cdot 10^{-5}$ mbar. So also for the upper limit there is a difference in the behaviour of the absorbers with and without gallium.

In summary Figure 5 shows a graph of the cation elemental ratios of the absorbers in the whole Δp -range. The ascertained process limits are also given.

In conclusion, this experiment underlines the necessity of an accurate control of the selenium flux during the selenization process to stay in between the process limits and for further optimization of the process. The

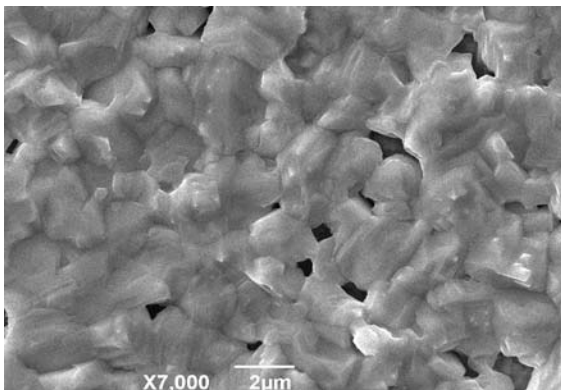


Fig. 4: SEM-image of a $\text{CuIn}_{0,75}\text{Ga}_{0,25}\text{Se}_2$ -absorber selenized at $1,0 \cdot 10^{-5}$ mbar

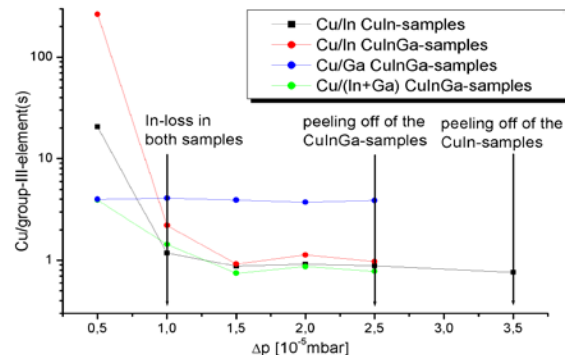


Fig. 5: Copper to group-III-element ratios of the CuInSe_2 - and the $\text{CuIn}_{0,75}\text{Ga}_{0,25}\text{Se}_2$ -samples with ascertained process boundaries

possibility to realize this control by measuring the beam equivalent pressure with the introduced method is demonstrated.

References

- [1] J. López-García and C. Guillén, Phys. Status Solidi A 206, No. 1, 84-90 (2009)
- [2] Miguel A. Contreras, Ingrid Repins, Wyatt K. Metzger, Manuel Romero, Daniel Abou-Ras, Phys. Status Solidi A 206, No. 5, 1042-1048 (2009)
- [3] V. Alberts, Semicond. Sci. Technol. 19 (2004) 65-69
- [4] J.R. Botha, S.A. Schumacher, A.W.R. Leitch, V. Alberts, Thin Solid Films 511-512 (2006) 316-319
- [5] N.G. Dhere, K.W. Lynn, Solar Energy Materials and Solar Cells 41/42 (1996) 271-279
- [6] M. Oertel, T. Hahn, H. Metzner, W. Witthuhn, Phys. Status Solidi C 6, No. 5, 1253-1256 (2009)

Wide-band phase locking of intrinsic Josephson junctions in a resonator

Alexander Grib¹ and Paul Seidel

¹ Physics Department, V. N. Karazin Kharkiv National University, 61077 Kharkiv, Ukraine

Recently, there was shown experimentally that BSCCO mesa structures of more than 500 intrinsic Josephson junctions can produce ac power up to 5 microwatt at frequencies 0.85-2.5 THz [1–4]. This creates the opportunity to build very compact sources of THz radiation. The structure acted as a strip resonator and the coherent radiation was registered in regions of cavity resonance frequencies appeared on the hysteretic branches of IV-curves. Most of the contemporary theoretical calculations of the emitted radiation from these systems are based on equations which take into account coupling between superconducting layers in the mesa [5–7]. Admitting usefulness of this approach, we would like to note that the chain of junctions interacting only by means of the common ac current (which is increased in a resonator) reveals also resonant steps of the IV-curves. The review of the earlier investigations on this topic is given in Ref. [8] and the modification of this model containing numerical calculations of resonant steps in the hysteretic region of the IV-curves was made in Ref. [9]. Therefore, the main features of the radiating system can be reproduced in this simple model too. We adopt here the representation of the resonator as the consecutive connection of the effective inductance (L) and the effective capacitance (C_{res}) [8]. In Ref. [10] we have shown that at certain parameters of the resonator the intrinsic junctions act not only as the sources of radiation but also as a part of the resonator. This dual action can lead to a new effect. The region of strong synchronization which is usually observed only in the vicinity of the resonance steps of IV-characteristics, becomes for the system with the dual action of junctions so broad that it can cover the whole hysteretic region below the resonant frequency. We found the condition of this wide-band coherent emission and analyzed

the origin of strong synchronization by means of the method of slowly varying amplitudes (SVA) and then proved our conclusions by means of numerical modeling.

The high frequency scheme of the chain of N junctions loaded by the resonance LC -contour is shown in Fig. 1. The Josephson junction in the extended resistively shunted model [8] is the parallel connection of the Josephson current I_{cn} , the resistance R_n and the capacitance C_{jn} , where $n = 1, 2, \dots, N$. In Fig. 1 we formally attached the capacitances of junctions to the external load [11].

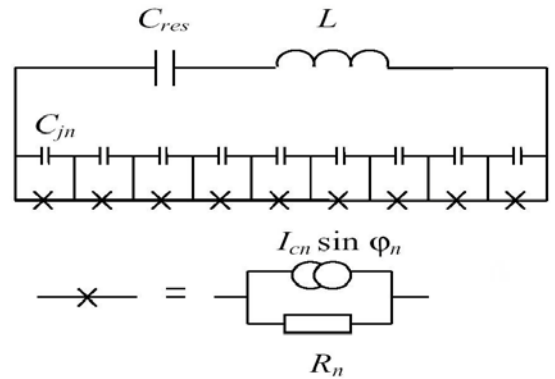


Fig. 1 High-frequency scheme of the system.

In the paper [10] we have shown the condition for synchronization of junctions by means of the SVA method. The analysis shows that there is a resonance of the parallel type in the resonator contour which is formed by all the capacitances of the junctions and the inductance of the resonant load. In this case capacitances of junctions become a part of the resonator. For this C_{res} must be larger than the value of the total capacitance of the whole array C_j/N . Then the impedance of the capacitance of the resonator (which is proportional to $1/C_{res}$) is small and the capacitive part of the impedance becomes defined completely by the capacitances of the junctions. Thus, C_{res} can

be arbitrary large providing the condition $C_{res} > C_j/N$ is fulfilled. This conclusion is new compared to other models [5–7].

To check our suppositions, we modeled the system shown in Fig. 1 at first for the chain of two junctions ($N = 2$) loaded by the resonator. We investigated two cases $C_{res} \ll C_j/N$ (the case 1) and $C_{res} > C_j/N$ (the case 2) which provided the same resonance frequency of the system at the proper choice of the system parameters. Synchronization of radiation in the system of two junctions depends on the value of the imaginary part of the connection coefficient $\text{Im}(y)$ of currents in the circuit [8,11]. For $N=2$ this coefficient can be calculated analytically [11]. We showed that synchronization appeared only at the resonance steps in the case 1 because values of $|\text{Im}(y)|$ were large only in the vicinity of steps. To the contrary, in the case 2 values of $|\text{Im}(y)|$ were large in the broad region of voltages that provided synchronization almost in the whole hysteretic region.

We investigated also synchronization in the chain of $N=350$ junctions loaded by the resonator. We made the Gaussian distribution of critical currents of junctions about 5%. We calculated IV-characteristics of the system and power of emitted radiation for the case $C_{res} > C_j/N$. Results of calculations are shown in Fig. 2.

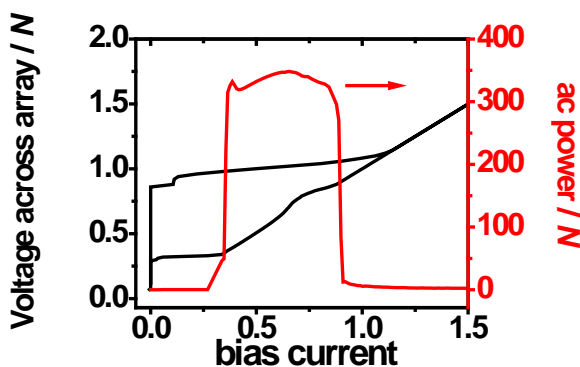


Fig.2 IV characteristics and emitted ac power for 350 junctions with 5% Gaussian spread.

It is seen that junctions are synchronized in the almost whole hysteretic region.

In conclusion, we found that the chain of junctions acts both as the source of radiation and as a part of the superconducting resonator when the effective capacitance of the resonator is larger than the total capacitance of all junctions. At this condition junctions are synchronized in-phase not only at the resonance steps but also in the whole hysteretic region of IV-characteristics below the resonant frequency (see Fig. 2). The maximal allowable spread of critical currents for this effect is about 5 to 10%.

Our results can be used to calculate parameters of the superconducting resonator which provides the described wide-band coherent emission. Because the penetration depth of electromagnetic waves is larger than the thickness of the mesa, the additional large effective capacitance of the resonator could be built below the mesa. The use of an adapted substrate with a high permittivity can also force this effect.

References

- [1] L. Ozyuzer et al., Science 318, (2007) 1291
- [2] K. Kadowaki et al., Physica C 468 (2008) 634
- [3] C. Kurter et al., IEEE Trans. Appl. Supercond. 19 (2009) 428
- [4] K. E. Gray et al., IEEE Trans. Appl. Supercond. 19 (2009) 886
- [5] M. Tachiki, S. Fukuya, and T. Koyama, Phys. Rev. Lett. 102 (2009) 127002
- [6] T. Tachiki, A. Sugawara, T. Uchida, Physica C 469 (2009) 1604
- [7] T. Koyama, H. Matsumoto, M. Machida, and K. Kadowaki, Phys. Rev. B 79, (2009) 104522
- [8] K. K. Likharev, Dynamics of Josephson junctions and Circuits (Gordon and Breach, Philadelphia, 1991)
- [9] E. Almaas and D. Stroud, Phys. Rev. B 65 (2002) 134502
- [10] A. Grib and P. Seidel, Phys. Status Solidi RRL 3, (2009) 302-304
- [11] A. N. Grib, P. Seidel, and J. Scherbel, Phys. Rev. B 65, (2002), 094508

Preparation and investigation of epitaxially grown CaRuO₃ / SrTiO₃ / CaRuO₃ – structures

J. Fischer, V. Grosse, F. Schmidl and P. Seidel

Ferroelectric films e.g. made of SrTiO₃ (STO) are needed for microwave tuneable applications [1]. The obtained layer system were investigated regarding to the crystal structure (measured by XRD) and the dielectric constant as a function of the film thickness, the temperature and an external electrical field. Furthermore, I-V characteristics were measured.

Our samples were grown on LaAlO₃ single crystal substrates, which show a good lattice match to CaRuO₃ and limit stray capacitances due to their low dielectric constant. First, a negatively processed photoresist mask was applied and a thin Au layer was deposited onto the substrate. After the lift-off these pads act as the connection to the bottom electrode and lower contact resistance to the bonding wires. Then a trilayer system of CaRuO₃/SrTiO₃/CaRuO₃ was grown by pulsed laser deposition. CaRuO₃ (CRO) is a conductive oxide showing a perovskite structure with a small lattice mismatch of about 1.4% compared to STO [2]. The insulator was deposited at 973 K, an oxygen pressure of 10 Pa and a laser energy density of 1.1 J/cm².

Subsequently, a positive mask for the bottom electrode was applied. The unprotected trilayer was removed by ion beam etching and filled with RF-sputtered SiO₂. After the second lift-off the positive mask for the top electrode (mask for bottom electrode, but rotated by 90°) was applied and Au was dc-sputtered to contact the top electrode with the pads, see figure 1.

Since the lattice constant of CRO in the a-b plane is smaller than that of STO the STO layer is compressively strained, which increases its the c-axis lattice parameter up to 0.9 % [2]. In figure 2 one can see the exponential behaviour of the relative c-axis with the film thickness d.

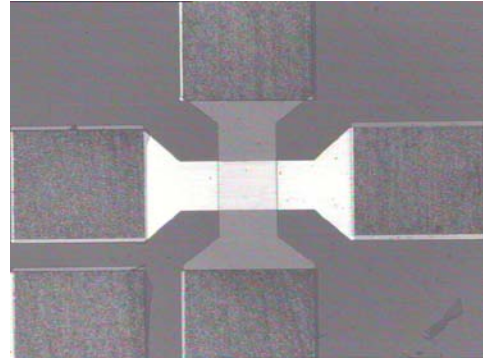


Fig. 1: Capacitor structure with pads for bonding.

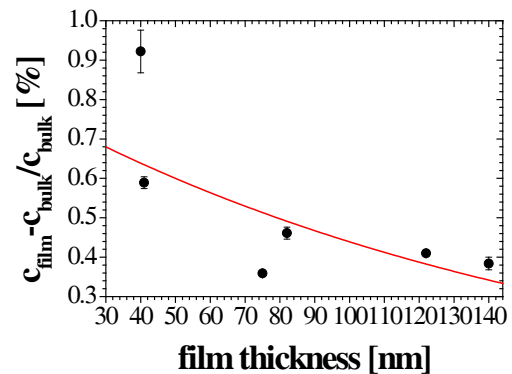


Fig. 2: Exponential relaxation of the c-axis of the STO layer with film thickness.

Metallic conductivity in the CRO layers can only be obtained in a narrow deposition parameter range. We used a laser energy density of at least 2.5 J/cm², a deposition temperature of 1023 K and an oxygen pressure of at least 10 Pa. The temperature dependence of the resistivity for an number of samples was measured to ensure metallic behaviour. The results are shown in figure 3. First capacitance measurements in the range from 4.2 K to 290 K were done using the Agilent E4980A LCR meter. In a parallel plate capacitor-like structure the dielectric constant ϵ is given by $C \cdot d / (\epsilon_0 \cdot A)$, where C is the capacitance, d the insulator thickness, ϵ_0 the vacuum permittivity and A the area of

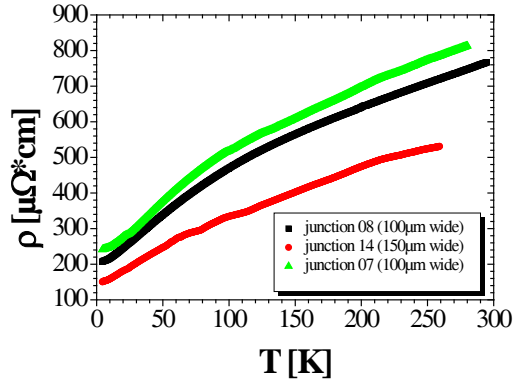


Fig.5: Temperature dependence of the resistivity of CRO.

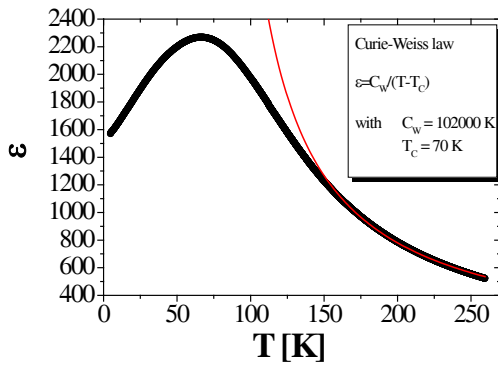


Fig.6: Temperature dependence of the dielectric constant.

the plates (fig. 4). On the right-hand side of the maximum ≈ 65 K) one can see the classical behaviour of a paraelectric material which is consistent with the Curie-Weiss law. The dielectric constant reaches values up to 2270. This is one order of magnitude smaller than the bulk value. This discrepancy and the decrease on the left-hand side of the maximum could be induced from the mechanical strain in the layers and existing fields. In accordance with Hemberger's quantum mechanical model [3] a depression of the dielectric constant caused of electric fields is predicted and also with high mechanical strain the maximum in the temperature dependence measurement is be explained by Palova et al. [4].

Additionally, we applied an external voltage at 4.2 K and a maximum near zero – it means low internal fields – appeared (see figure 5), as was expected by Hemberger's model.

In the last figure 6 one can see an I-V characteristic, which shall give an

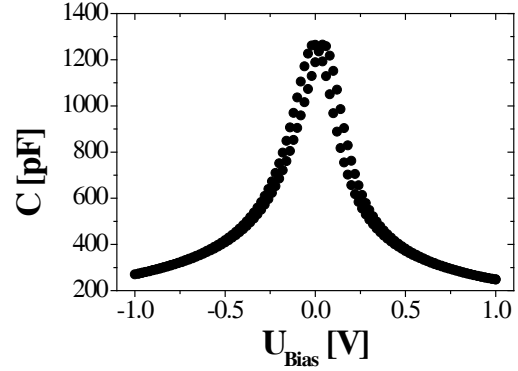


Fig. 4: Capacitance as a function of an external voltage @ 4.2 K

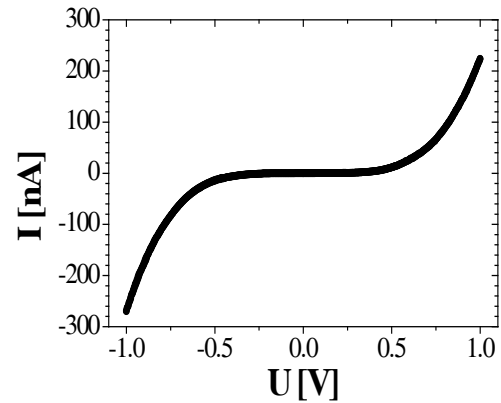


Fig. 3: I-V characteristic of the structure @ 4.2 K

explanation about the conduction mechanisms in the STO. But in this case additional investigations are necessary.

References:

- [1] Tagantsev AK, Sherman VO, Astafiev KF, Venkatesh J and Setter N 2006 *Journal of Electroceramics* 11 5-66
- [2] Kennedy R J, Madden R and Stampé P A 2000 *Journal of Physics D: Applied Physics* 34 1853-1861
- [3] Hemberger J, Lunkenheimer P, Viana R, Böhmer R and Loidl A 1995 *Physical Review B* 52 13159-62
- [4] Palova L, Chandra P and Rabe KM 2007 *Physical Review B* 76 014112

Nanocrystalline Ferromagnetic Materials at Low Temperatures and Their Use in a Superconducting Beam Monitor

R. Geithner, R. Neubert, W. Vodel and P. Seidel

For the upcoming FAIR (Facility for Anti-proton and Ion Research) project [1] at GSI Darmstadt an improved LTS SQUID based cryogenic current comparator (CCC) for non-contact beam monitoring should be developed.

In the CCC, an ion beam current I_{Beam} , which flows through a superconducting hollow cylinder is transformed via a superconducting toroidal pickup coil with a ferromagnetic core and a matching transformer into a current which is fed through the input coil of the readout DC SQUID $UJ III$ [2], [4]. The sensitivity ultimately depends on the pickup coil. It was demonstrated [3] that the use of a ferromagnetic core leads to a possible optimization for better noise performance using materials with a high μ_r , as

$$\frac{I_s}{I_n} \propto \sqrt{\mu_r}. \quad (1)$$

Because the signal to noise ratio I_s / I_n is proportional to the permeability of the core, magnetic materials with high permeability, especially nanocrystalline materials such as Nanoperm [6], may permit further noise reduction [4].

For this reason, the magnetic properties of further samples of the above-mentioned material Nanoperm were characterized in a temperature range from 4.2 K up to room temperature and a frequency range from 20 Hz to 2 MHz [4].

The following evaluation is limited to the magnetic properties at 4.2 K, the working point of the CCC. The maximum relative permeability μ_r of our samples varied between 50,000 for Nanoperm M074 and 30,000 for Nanoperm M033 (see Fig. 1). In addition, the frequency dependence of Vitrovac 6025F [5] and Vitroperm 500F [5] is also plotted in Fig. 2. Both, Nanoperm M033 and M074 showed only small variations over a wide frequency range from 20 Hz to 10 kHz (see Fig. 1). Whereas, the permeability of Vitroperm 500F and Vitro-

vac 6025F strongly depended on the frequency.

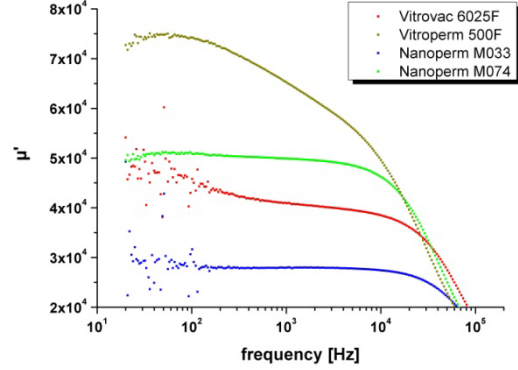


Fig. 1: Relative permeability of different toroidal cores with one superconducting winding at 4.2 K

The noise measurements were carried out as described in the annual report 2008 [4].

The intrinsic noise level of the SQUID system, measured with shunted input coil, shows no frequency dependence down to 0.5 Hz (see black line in Fig. 2).

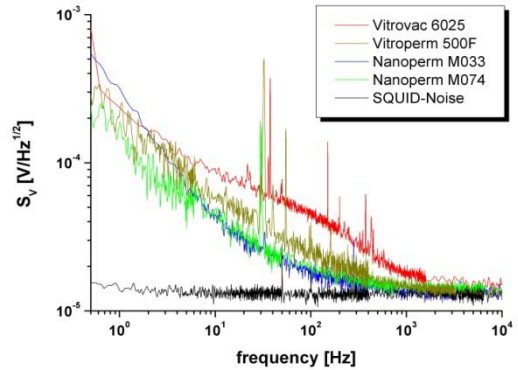


Fig. 2: Voltage noise of different toroidal cores with one superconducting winding at 4.2 K

All illustrated materials had a $1/f$ noise behavior with different slopes up to corner frequencies of 200 Hz for Nanoperm M033 and 1 kHz for Vitrovac 6025F (see Fig. 2). In the frequency range of 1 Hz to 1 kHz the Nanoperm samples M033, M074 showed a significantly less total noise compared to the VAC samples Vitrovac 6025F and Vitroperm 500F.

For the total noise of the CCC you have to

pay attention to the noise contribution of the matching transformer. This transformer is necessary to adapt the inductance of the pickup coil ($> 20 \mu\text{H}$) to the inductance of the SQUID input coil of $0.8 \mu\text{H}$. The current sensitivity will also be increased due to the winding ratio of the transformer and the different inductances of the CCC.:

$$\frac{I_{SQ}}{I_{Beam}} = \frac{n_{TP}}{n_{TS}} \cdot \frac{1}{1 + \frac{L_{SQ}}{L_{TS}}} \cdot \frac{1}{1 + \frac{L_{TP} \cdot L_{SQ}}{(L_{TS} + L_{SQ}) \cdot L_{Pick}}} \quad (2)$$

I_{Beam} is the beam current, I_{SQ} the current through the input coil of the SQUID, n_{TP} and n_{TS} are the numbers of windings of the primary, and respectively secondary coil of the transformer. L_{TP} and L_{TS} are the appropriated inductances.

The core material of the matching transformer has to fulfill different requirements. The inductances of the coils and therefore the relative permeability of the core should be frequency independent to achieve a broadband transmission. Furthermore, the noise contribution of the coil should be negligible, resulting in a better signal to noise ratio caused by the gain of current sensitivity. Vitrovac 6030 [5] was chosen as core material for the matching transformer because it showed only little frequency dependence up to 100 kHz. (see Fig. 3).

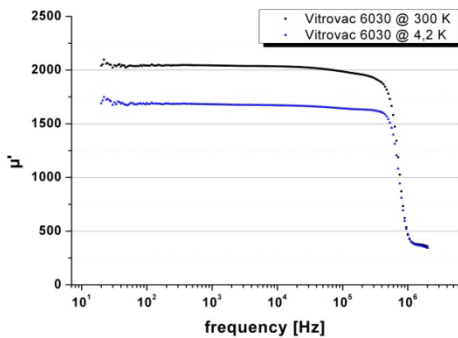


Fig. 3: Relative permeability of the core material Vitrovac 6030 of the matching transformer at different temperatures of 300 K and 4.2 K

The noise contribution of the matching transformer to the total noise is shown in Fig. 4. Although the noise is shifted upwards the noise contribution of the matching transformer seems to have little 1/f noise because of the parallel shift. So, Vi-

trovac 6030 is the ideal material for this application.

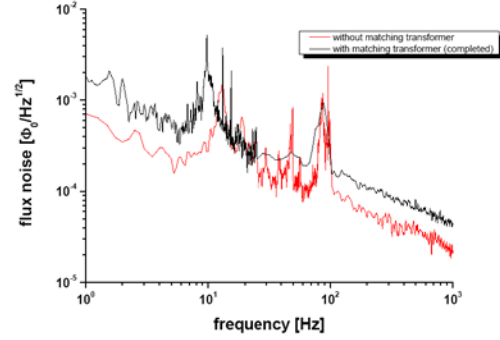


Fig. 4: Noise of the CCC from the former DESY-project with and without a matching transformer made out of Vitrovac 6030

The properties of the ferromagnetic core material set the fundamental limits for noise reduction in a CCC. According to our measurements the nanocrystalline material Nanoperm presents significant advantages for the CCC due to the high permeability over a wide frequency range and low noise level at liquid helium temperatures. Now, we need to negotiate with Magnetec to get customized cores of Nanoperm that meet our specifications regarding dimensions and high relative permeability. Furthermore, some changes of the construction are planned to facilitate the welding of the pickup coil and the meander shaped shielding. Some further investigations are necessary to minimize disturbing influences such as microfonic effects.

References

- [1] Facility for Antiproton and Ion Research (FAIR), homepage. Available: <http://www.gsi.de/fair/>.
- [2] W. Vodel, K. Mäkinieni, *Meas. Sci. Technol.*, vol. 3, pp. 1155-1160, 1992.
- [3] A. Steppke, R. Geithner, S. Hechler, R. Nawrodt, R. Neubert, W. Vodel, M. Schwickert, H. Reeg, and P. Seidel, *IEEE Trans. Appl. Supercond.* 19 (2009) 768.
- [4] R. Geithner, A. Steppke, R. Neubert, W. Vodel and P. Seidel, *annual report IFK*, 2008
- [5] VACUUMSCHMELZE GmbH & Co. KG, Gruener Weg 37, D-63450 Hanau, Germany.
- [6] MAGNETEC GmbH, Industriestrasse 7, D-63505 Langenselbold, Germany.

Size distribution and crystallographic properties of self-assembled gold nano particles in $\text{YBa}_2\text{Cu}_3\text{O}_{7-\delta}$ thin films

V. Grosse, S. Engmann, F. Schmidl, A. Undisz*, M. Rettenmayr* and P. Seidel

**Institut für Materialwissenschaften und Werkstofftechnologie, Friedrich-Schiller-Universität Jena, Löbdergraben 32, D-07743 Jena*

The mobility of flux vortices in high temperature superconductors in general, and $\text{YBa}_2\text{Cu}_3\text{O}_{7-\delta}$ (YBCO) thin films in particular, is an essential limiting factor determining the performance of superconducting devices, such as Josephson junctions and magnetic field sensors. Flux noise properties and critical current density can be improved by adding artificial defects serving as pinning centers. An easy and effective technique is decorating the substrate with prefabricated nano particles before YBCO film deposition. A number of materials, such as CeO_2 [2], Y_2O_3 [3, 4] as well as MgO , BaZrO_3 and Ir [5–7], have successfully been tested in this regard.

The aim of this work is to analyze the size distribution and crystallographic properties of gold (Au) nano particles, which were formed by self-assembling during the deposition of YBCO thin films.

Prior to the growth of the YBCO films a thin gold layer was deposited on SrTiO_3 single crystal substrates under high vacuum conditions ($p_0 < 5 \cdot 10^{-4}$ Pa). For layer thicknesses up to 20 nm this was accomplished by pulsed laser deposition using a KrF excimer laser at a repetition rate of 10 Hz. Under these conditions the growth rate was 4.4 nm/min. Thicker Au layers were grown by dc-sputtering to limit deposition time.

Subsequently, the substrate was heated to 750°C. Using again a KrF excimer laser a 150 nm thick YBCO film was then grown in an atmosphere of pure oxygen ($p_{\text{O}_2} = 50$ Pa). The repetition rate was set to 5 Hz. During film growth the Au layer disintegrates and small particles evolve. The size of these particles mainly depends on the thickness of the initial gold layer.

TEM images show that particles having diameters much smaller than the YBCO film thickness preferentially grow at the YBCO surface or at the interface between YBCO and the substrate. A significantly smaller number can be found within the YBCO layer. Greater particles are surrounded by the YBCO matrix and reach from the substrate to the YBCO surface.

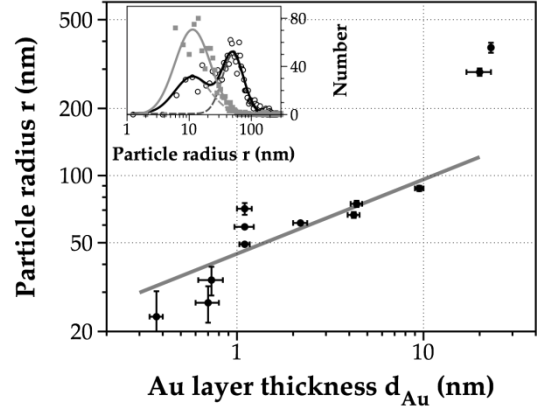


Fig. 1: Particle radius r vs. initial Au layer thickness d_{Au} . The gray line is a $r \propto d_{\text{Au}}^{1/3}$ fit to the data in the range of 1 nm to 10 nm. The inset shows a typical histogram of the size distribution of particles on the surface of pure YBCO (gray) and of Au decorated YBCO (black).

To analyze the size distribution of the particles we investigated the surface of our samples by atomic force microscopy. The AFM images were analyzed using the GWYDDION tool [8] to identify and count the particles. A typical histogram of the distribution of particle radii is shown in the inset of figure 2. The data is best characterized by two lognormal distributions. The first at radii around 10 nm describes the size distribution of outgrowths of the YBCO film. The same characteristic can be found on the surface of pure YBCO. The second lognormal distribution at higher radii describes the distribution of the gold nano particles.

We compared the size distribution of the gold nano particles for different initial gold layer thicknesses. The results are plotted in figure 2 where the mean of the radius' natural logarithm is taken to be the typical size of the particles. For gold layer thicknesses between 1 nm and 10 nm we observed a distinct dependence of $r \propto d_{\text{Au}}^{1/3}$, whereas the number density reaches a maximum and can be considered constant in this range. This result suggests an independent particle formation with no interactions between particles.

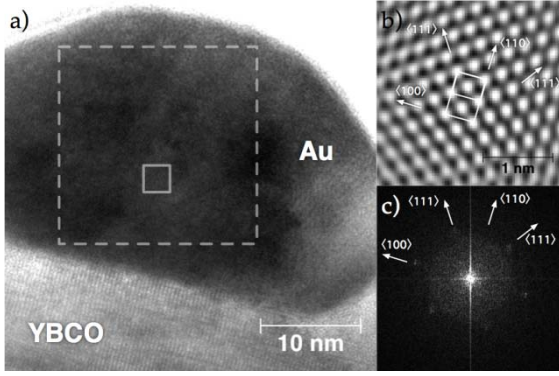


Fig. 2: a) High resolution TEM image of a single crystalline Au particle at the YBCO surface. From the dashed square in a) we reconstructed the lattice structure by FFT filtering. A detail of this reconstruction is shown in b) (from the area represented by the solid square). c) Corresponding FFT spectrum.

The total volume of the Au layer transforms into spherical particles. The same behavior should apply for thinner gold layers. The observed deviations from the $r \propto d_{\text{Au}}^{1/3}$ dependence can, however, be explained by considering an incomplete Au coverage of the substrate after deposition.

From crystallographic analysis, we found all Au particles smaller than approximately 50 nm to be single crystalline. θ - 2θ -diffraction patterns only show the $(111)_{\text{Au}}$ reflection besides the YBCO reflections. However, in high resolution TEM images we also observed particles having the $(110)_{\text{Au}}$ direction parallel to the $(110)_{\text{YBCO}}$ direction, see figure 2. We can not exclude that there exist particles with other orientations even though we did not find them in the present TEM images.

Rocking curve widths of the $(111)_{\text{Au}}$ reflection do not exceed 0.4° for a thickness of the initial gold layer of less than 30 nm suggesting an epitaxial relation between Au and YBCO, see figure 3. This is a somewhat surprising result since the lattice of a (111) or (110) oriented Au particle does not fit properly on an YBCO a-b surface. In the c-direction, on the other hand, one finds a good lattice match by assuming multiples of the $(110)_{\text{Au}}$ and $(111)_{\text{Au}}$ plane spacing:

$$4 \times d_{(110)\text{Au}} = 0.988 \times d_{(001)\text{YBCO}}$$

$$5 \times d_{(111)\text{Au}} = 1.009 \times d_{(001)\text{YBCO}}$$

The relative in-plane lattice mismatch for an epitaxial growth of $(001)_{\text{Au}}$ parallel to the $(001)_{\text{YBCO}}$ or $(001)_{\text{SrTiO}_3}$ direction is 5.0% or 4.3%, respectively. Orientation of the particles is thus coupled rather to the YBCO c-axis than to

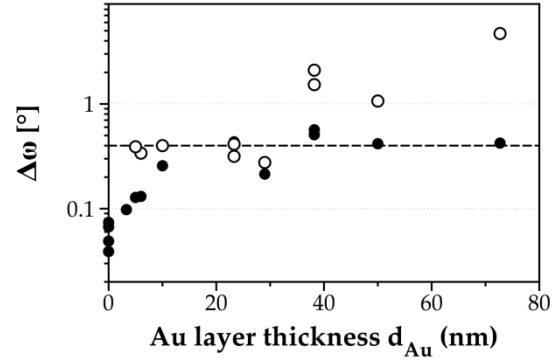


Fig. 3: Rocking curve widths $\Delta \omega$ of the YBCO thin film (solid circles) and Au particles (open circles) in dependence on Au layer thickness.

the a-b plane, whereas high strains evolving from the in-plane lattice mismatch could be the origin for the tendency of Au to form islands and small particles at high temperatures.

Though it is not yet proven, strain fields emanating from these particles are likely to increase flux pinning. In upcoming experiments we will demonstrate the influence of Au particles on the performance of superconducting interference devices.

References

- [1] L. Krusin-Elbaum, J. R. Thompson, R. Wheeler, A. D. Marwick, C. Li, S. Patel, and D. T. Shaw, *Appl. Phys. Lett.* **64**, 3331 (1994).
- [2] J. C. Nie, H. Yamasaki, H. Yamada, Y. Nakagawa, K. Develos-Bagarinao, and Y. Mawatari, *Supercond. Sci. Tech.* **17**, 845 (2004).
- [3] K. Matsumoto, T. Horide, A. Ichinose, S. Horii, Y. Yoshida, and M. Mukaida, *Jap. J. App. Phys. Part 2 – Letters & Express Letters* **44**, L246 (2005).
- [4] P. Mele, K. Matsumoto, T. Horide, O. Miura, A. Ichinose, M. Mukaida, Y. Yoshida, and S. Horii, *Physica C* **445**, 648 (2006).
- [5] T. Aytug, M. Paranthaman, K. J. Leonard, K. Kim, A. O. Ijaluola, Y. Zhang, E. Tuncer, J. R. Thompson, and D. K. Christen, *J. Appl. Phys.* **104**, 043906 (2008).
- [6] T. Aytug, M. Paranthaman, K. J. Leonard, S. Kang, P. M. Martin, L. Heatherly, A. Goyal, A. O. Ijaluola, J. R. Thompson, D. K. Christen, R. Meng, I. Rusakova, and C. W. Chu, *Phys. Rev. B* **74**, 184505 (2006).
- [7] F. J. Baca, P. N. Barnes, R. L. S. Emergo, T. J. Haugan, J. N. Reichart, and J. Z. Wu, *Appl. Phys. Lett.* **94**, 102512 (2009).
- [8] GWYDDION, SPM data visualization and analysis tool by D. Necas *et al.*, <http://gwyddion.net>

Numerical calculation of thermoelastic damping of vibrating bulk samples

D. Heinert, C. Schwarz, R. Nawrodt¹, S. Kroker², A. Grib³,
W. Vodel, A. Tünnermann² and P. Seidel

¹*Institute for Gravitational Research, University of Glasgow, G12 8QQ Glasgow, Scotland*

²*Institut für Angewandte Physik, A.-Einstein-Str. 15, 07745 Jena*

³*Physics Department, Kharkov National University, 61077 Kharkov Ukraine*

Many fields in modern science demand highly sensitive instruments. Among them is the direct detection of gravitational waves. To successfully detect gravitational waves instruments capable to resolve a relative length change of 10^{-21} are necessary [1]. Reaching such resolutions clearly affords minimizing noise in all parts of the detector. In the case of an interferometric gravitational wave detector a strong noise contribution results from the mechanical motion of the optical components. Besides the temperature this displacement noise is linked to the mechanical losses of the substrate materials via the fluctuation-dissipation-theorem [2]. Thus, achieving low noises affords the search for materials showing low mechanical loss at low temperatures.

Typical setups for an experimental determination of mechanical losses use the principle of resonant excitation. Our setup [3] uses an electrostatic excitation of a cylindrical bulk sample to resonant motions. Then the electric field is switched off and the vibrational decay is recorded optically. The decay time τ specifies the $1/e$ decrease of the amplitude. The loss ϕ as a measure of dissipated energy is then given by $\phi = (\pi f \tau)^{-1}$ with the frequency f of the vibration. The whole setup is placed in a cryostat to allow measurements at cryogenic temperatures from 5 K to 300 K. Finally a loss spectrum is obtained as the superposition of all occurring loss mechanisms. Typical mechanisms are, e.g., phonon-phonon-damping, defect induced damping and thermoelastic damping (TED)

[4, 5]. In this report we concentrate on the effect of TED as a severe limitation of the mechanical loss in crystalline materials.

TED is caused by volume changes of different parts in the substrate under vibrations. These volume changes result in an introduction or removal of heat energy. Consequently, the regions' temperature will change and heat currents appear within the sample. The heat flow leads to an increase of entropy and to the dissipation of energy, which can be observed by the decay of the mechanical oscillation.

We start with the calculation of the mode shape of the resonance using the FE software COMSOL yielding the mechanical stress tensor σ_{ij} . Subsequently we calculated the temperature distribution within the sample. For an isotropic body this results from the equation of heat transfer,

$$\mathbf{C} \frac{\partial}{\partial t} \mathbf{T} - \lambda \Delta \mathbf{T} = -\alpha \frac{\partial}{\partial t} \left(\sum_{i=1}^3 \sigma_{ii} \right) \mathbf{T}, \quad (1)$$

with the specific heat per volume \mathbf{C} , the thermal conductivity λ and the coefficient of linear thermal expansion α . As the resulting temperature changes are expected to be small, the temperature on the right side can be replaced by the mean temperature T_0 . This approximation dramatically simplifies the numerical calculation and is valid for small deformations, an approximation which is fulfilled for vibrating bulk samples. In a third step the energy dissipated in one cycle ΔE is given by Eq. 2, where the time integration is performed over one cycle and the spatial integration over the sample volume.

$$\Delta E = \frac{1}{T_0} \iint \lambda \sum_i \left(\frac{\partial}{\partial x_i} T \right)^2 dV dt \quad (2)$$

Finally, the mechanical loss ϕ is obtained with the total strain energy E_{tot} via

$$\phi = \frac{1}{2\pi} \frac{\Delta E}{E_{\text{tot}}} \quad (3)$$

We tested our numerical code on an analytical solution for TED of an isotropic body with a vanishing Poisson's ratio ν . With the material's density ρ Braginsky therefore yields [6]

$$\phi = \frac{\lambda T \alpha^2 \rho \omega}{C^2} \quad (4)$$

This analytical model appears to be correct only for longitudinal modes, which are similar to standing waves in a one dimensional rod.

For all calculations we used a calcium fluoride sample 76.2 mm in diameter and 75 mm in length. Thermal properties of CaF_2 were taken from the literature and Young's modulus was assumed as $Y=138$ GPa and temperature independent. Fig. 1 compares our numerical with the analytical approach. It shows an excellent agreement between both solutions.

We then used the numerical code to investigate the influence of the mode shape (open circles in Fig.1) and Poisson's ratio (triangles in Fig. 1) on the mechanical loss spectrum. While the characteristic temperature behavior does not change in any parameter set we obtained a significant change in the mechanical loss. Both effects are capable of changing the amount of TED by a factor of up to 10. Thus, it is important to choose the vibration mode as well as Poisson's ratio in a deliberate way to minimize TED. The necessary variation of parameters can be realized by a change of the measuring frequency or a change of the crystalline orientation of the substrate, respectively.

The exact knowledge and minimization of TED allows a subtraction from the measured loss spectrum and is, thus, important to obtain reliable information about the remaining internal loss processes. This characterization will help to control the influ-

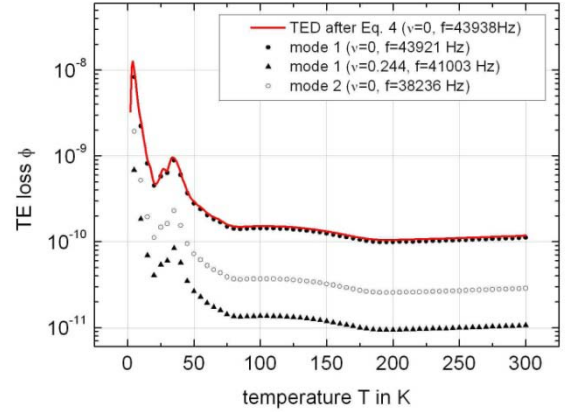


Fig. 1 The diagram shows TED of a cylindrical CaF_2 sample from 5 K to 300 K. The red line represents the analytical expression after Eq. 4, while the points show numerical results (see text). Simulated frequencies f and used Poisson's ratios ν are given in the legend.

ence of these loss mechanisms on future detectors and lead to an increase of detectors' sensitivity.

The presented numerical calculation of TED appears to be a valuable tool for investigation of loss processes in arbitrarily shaped bulk samples. Consequently, it will support efforts of minimizing thermal noise in future interferometric gravitational wave detectors [7] as well as in the fields of atomic force microscopy or the stabilization of optical cavities [8, 9].

This work was supported by the German science foundation under contract SFB TR7.

References

- [1] R. Saulson, *Fundamentals of gravitational wave detectors*, World Scientific, Singapore 1994.
- [2] H. B. Callen, T. A. Welton, *Phys. Rev.* 83 (1951), 34.
- [3] R. Nawrodt et al., *Eur. Phys. J. Appl. Phys.* 38 (2007), 53.
- [4] A. Grib et al., *J. Appl. Phys.* 107 (2010), 013504
- [5] A. Zimmer et al., *Rev. Sci. Instrum.* 78 (2007), 063905
- [6] V. B. Braginsky, V. P. Mitrofanov, V. I. Panov, *Systems with Small Dissipation*, University of Chicago Press, Chicago/London 1985
- [7] M. Punturo et al., submitted to *Class. Quantum Grav.* (special edition for AMALDI 8), *Third Generation of Gravitational Wave Observatories and their Science Reach*
- [8] S. Prabhakar, S. Vengallatore, *J. Micromech. Microeng.* 17 (2007), 532
- [9] J. Hofer, A. Schliesser, T. J. Kippenberg, <http://arxiv.org/abs/0911.1178> (2009)

Rotation course characterisation of air turbine for improvement of an HTSC-MRX system for measurement of Néel relaxation of superparamagnetic nanoparticles

R. Kockrick, C. Becker, K. Höfer, A. Steppke*, F. Schmidl and P. Seidel

* Max Planck Institute for Chemical Physics of Solids, Nöthnitzer Straße 40, 01187 Dresden, Germany

Introduction:

Superparamagnetic Nanoparticles (MNP) with dimension of 1-100 nm have applications from data processing across contrast media for magnetic resonance tomography and drug targeting [1] up to neoplasm treatment so called hyperthermia where the MNP with special shells docking on the afflicted cell tissue and get destroyed by the heat that is produced by the MNP as response to an alternating magnetic field [2].

This wide and increasing area of applications yields to the necessity of characterisation of MNP. Concerning to the medicine field and non-destructive (NDE) measurements it is essential to use high temperature superconducting (HTSC) sensors on account of thin cryostat walls to decrease the distance of probes and lower cost for refrigeration with liquid nitrogen than the low temperature superconducting (LTSC) setups cooled with liquid helium.

Measurement setup:

Our magnetic relaxation measurement system (MRX) to survey the Néel relaxation of MNP uses HTSC flip-chip SQUID gradiometers. To improve the noise of the SQUID signal we apply an air turbine to rotate the MNP using a dynamic lock-in treatment. Néel relaxation has a half-value period in range of 1s and decay in form of $m \propto \ln(1 + \frac{t_{mag}}{t})$ [3], at which m is the measurable magnetic signal and t_{mag} the time in the homogeneous magnetic field before the measurement starts. Furthermore after the half-value period the signal is still in the noise of the measurement, so that it is important to get the measured values at the beginning as exact as possible.

That also concerns to the frequency of the rotation because of the direct relationship. This rotation course is measured optically with a laser, a hole in the gyration cylinder and a phototransistor that counts the frequency [Fig. 1] with a slew rate up to 99,5kV/s.

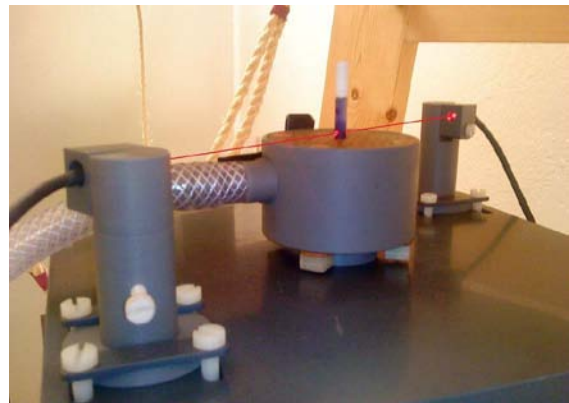


Fig. 1 - Optical rotation course receiver

By determination of an “effective shot right through angle” that depends on the speed it is possible to add more breakpoints [Fig. 2].

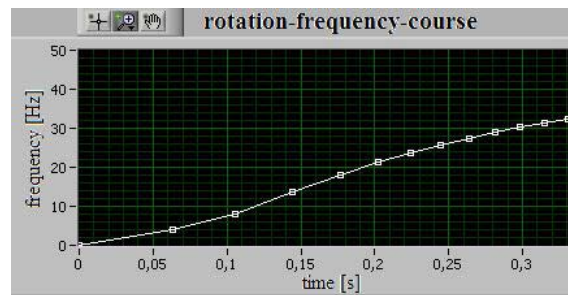


Fig. 2 - Frequency course with double breakpoints

This frequency course depends on the theory of linear approximation and fits the original course to 99,5% verified by simulations except the first two points with a deviation of 24% or 8% respectively.

To get the correct course at the beginning (first half turn – two measured values) there

was installed a rotating mirror instead of the MNP top adapter which reflect the laser on an accordant scaled marker [Fig. 3].

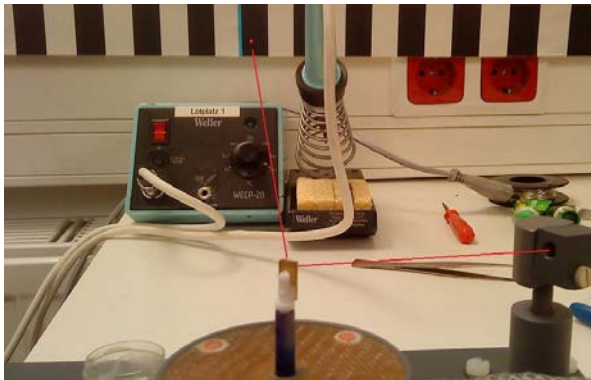


Fig. 3 - Rotating mirror setup

The resulting laser point on the scale was filmed with a high-speed camera with up to 1000 frames per second (fps). In addition there was installed a led parallel to the circuit of the electro valve and as reference to the computer.

Results:

The computer controlled led was turned on for 40 ms and the film offered exact 40 pictures with illuminated led, which authenticates the congruence between picture time distance and real time.

The measurement shows a delay from the opening of the electro valve till the beginning of the rotation not depending on the usual used air pressures of 31 ± 1 ms.

The laser point was filmed with 420 fps for approximation (bigger quadrats) and 1000 fps for fine measurement (smaller circles). According the results in the graph the frequency course shows not quadratic or cubic but a totally linear behaviour at the beginning after the delay.

Fig. 4 shows a frequency course linear in velocity so constant in acceleration, which comes from the constant pressure of the air valve. That shows that fluctuations of pressure by opening the valve, pressure decrease by rotation as well as friction effects have no influence.

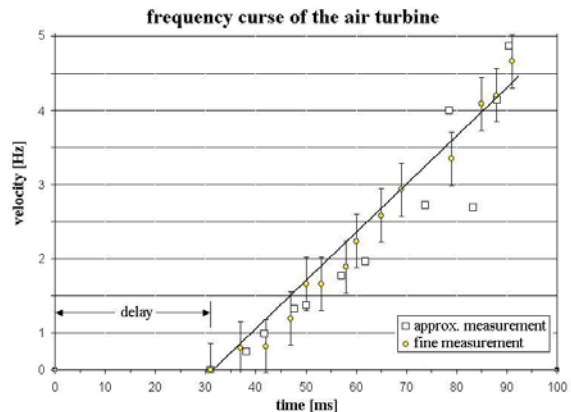
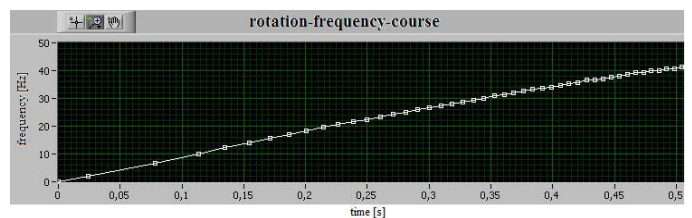


Fig. 4 - High-speed measurement of frequency course with delay

After all the frequency is the quotient from angle and time with considering on the delay with an accuracy of over 99%. Fig. 5 shows the new frequency course with program embedded delay (rotation starts at zero). The little fluctuations in the frequency that derive from a little asymmetry of the laser hole, does not affect the measurement because of the continuous course in conjunction with the retroactively fit of the frequency course.

Fig. 5 - Frequency course with embedded delay



References:

- [1] Andreas S. Lübke, M.D. Ph.D. Christoph Alexiou, Christian Bergemann, Clinical Applications of Magnetic Drug Targeting, *Journal of Surgical Research* **95**, 200 – 206 (2001)
- [2] T. Goetze, C. Gansau, N. Buske, M. Roeder, P. Görnert and M. Bahr: Biocompatible magnetic core/shell nanoparticles, *Journal of Magnetism and Magnetic Materials* **252**, 399-402 (2002).
- [3] F. Ludwig, E. Heim, and M. Schilling: Characterization of superparamagnetic nanoparticles by analyzing the magnetization and relaxation dynamics using fluxgate magnetometers, *JOURNAL OF APPLIED PHYSICS* **101**, 113909 2007

Cryogenic Q-factor measurements on high purity silicon bulk material

C. Schwarz, R. Nawrodt**, D. Heinert, S. Kroker*, R. Neubert, M. Thürk, W. Vodel,
A. Tünnermann*, and P. Seidel

* *Institut für Angewandte Physik, A.-Einstein-Str.15, 07745 Jena*

** *Institute of Gravitational Research, University of Glasgow, G12 8QQ, United Kingdom*

Current gravitational wave (GW) detectors are operating at their design sensitivity. An increase in sensitivity is planned by going to so-called 2nd generation detectors (or advanced detectors). Here, the infrastructure of the 1st generation detectors will be reused and modern techniques implemented in order to obtain a sensitivity enhancement. A further increase in sensitivity of a factor of 100 compared to the 1st generation is proposed for the 3rd generation detectors. Here, a radical change in the infrastructure, optics, lasers and test mass material is needed. It is planned to run these detectors at cryogenic temperatures [1]. Previous investigations revealed that fused silica cannot be used due to its large mechanical loss at low temperatures [2]. This mechanical loss is directly linked to the Brownian thermal noise of the component by means of the fluctuation-dissipation-theorem [3, 4]. Silicon seems to be one of the most promising bulk material candidates [5]. A detailed investigation of the intrinsic loss mechanisms of silicon is thus needed in order to be able to find the optimum operational point of such a cryogenic mirror. The mechanical loss at a resonance is given by the reciprocal of its mechanical Q-factor.

The investigated silicon single crystal was grown by the Czochralski process known for low dislocation densities. The sample is p-type boron doped with a resistivity of $10^4 \Omega \cdot \text{cm}$. Both end faces of the silicon crystal (diameter 110 mm, length 200 mm), with the [100] axis parallel to the cylinders axis, were polished to optical quality. The barrel remained in crystal growth condition

to minimize micro scratches and dislocations in the surface layer.

In order to determine the mechanical Q-factor the silicon sample was suspended as a pendulum by a $150 \mu\text{m}$ thick tungsten wire (see fig. 1) to reduce seismic disturbances. The probe chamber was evacuated to a pressure lower than 10^{-3} Pa to minimize any additional damping due to the presence of residual gas. The setup is placed in a special built cryostat with an operational temperature from 5 to 325 K [6]. Different resonant vibrations have been excited by a multistrip electrostatic actuator mounted in parallel to one end face. The vibration of the sample was sensed by means of a commercial laser vibrometer. After exciting the vibration the electric field was switched off and the recording of the free decay of the amplitude started. The Q-factor is given by:

$$Q = \pi f_0 \tau, \quad (1)$$

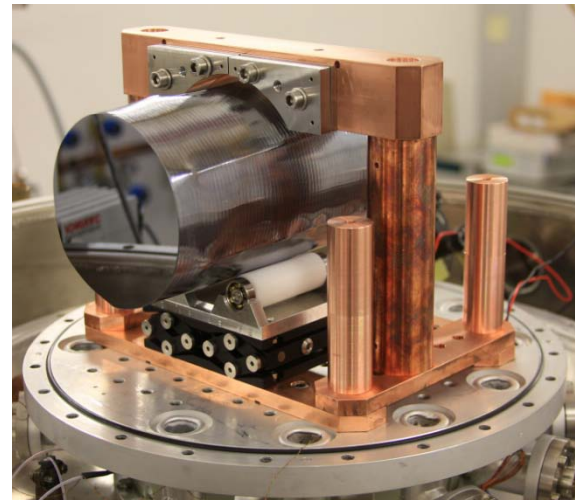


Fig. 1 Photograph of the open probe chamber with the suspended silicon sample.

with the resonant frequency f_0 and the characteristic ring-down time τ which corresponds to an amplitude decay to e^{-1} compared to the initial value.

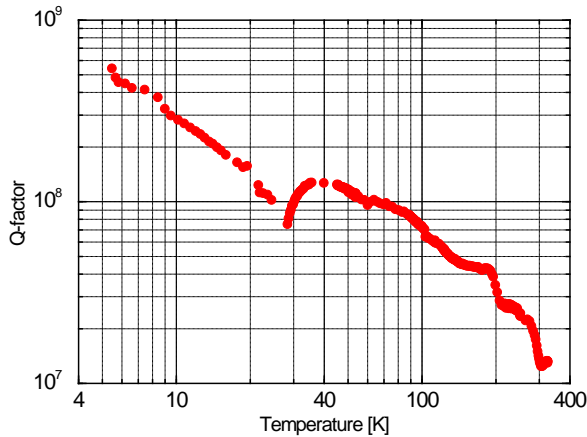


Fig. 2 Cryogenic Q-factor measurement of a drum mode at 22.3 kHz.

Fig. 2 shows the Q-factor dependence of temperature between 5 and 325 K. The log-log-scale diagram was chosen to emphasize the increase of the Q-factor below 30 K. Each dot represents a ringdown between 200 s at room temperature and roughly 8000 s at minimum temperature. Thus, the measurement of several modes lasts up to 6 weeks for a whole temperature cycle of one substrate. Recently measured but unpublished data of all side polished silicon substrates showed more than one order of magnitude higher Q-factors at room temperature. One possible reason might be the structure of the substrates' barrel. Due to the grooves (from the crystal growth process) around the surface it was not possible to support the sample by the tungsten wire exactly below the samples' centre of mass. This usually yields to a slight tilt of the substrate in horizontal orientation which causes additional friction to the resonant vibrations between the sample and the suspension wire. Thus, the suspension seems to limit the Q-factor above 100 K.

The 22 kHz mode showed a minimum at around 28 K (see fig. 2) which is probably

associated with crystal imperfections. Several other resonant modes between 13 kHz and 54 kHz showed similar dips. One of them (see fig. 3 for details) could be identified as a resonant coupling between the mode and the suspension wire.

Close to minimum temperature of (5.5 ± 0.2) K the Q-factor exceeded 6×10^8 with a ringdown time τ of 7700 s.

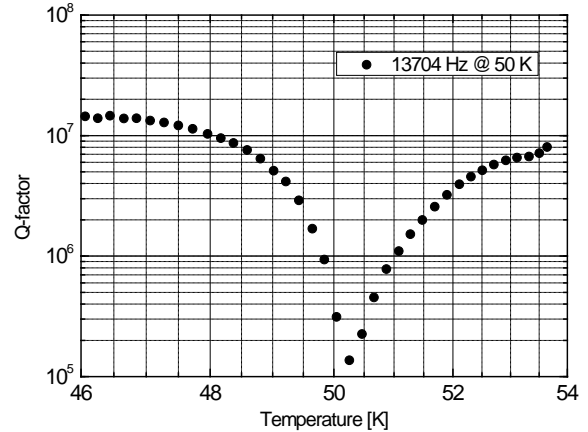


Fig. 3 Narrow dip of the temperature dependent Q-factor of the 13 kHz mode due to a match of the samples and the suspension wires resonant frequency at 50.2 K.

A high mechanical Q-factor measurement at low temperature was presented. Q-factors as high as 6×10^8 have been achieved at low temperatures. These values are used as a starting point in a design study for a 3rd generation detector in Europe [1] with an improved sensitivity of a factor of 100 compared to initial detectors.

This work was supported by the German science foundation under contract SFB TR7.

References:

- [1] www.et-gw.eu
- [2] Strakna, Phys. Rev. 123, 6 (1961) 2020
- [3] Callen et al., Phys. Rev. **83**, 34 (1951)
- [4] Levin, Phys. Rev. D, 57 (1998) 659
- [5] Rowan et al., Phys. Lett. A, 347(1-3) (2005) 25
- [6] Nawrodt, Cryogenics 46 (2006) 718

Electrical transport in thin film iron pnictide junctions

P. Seidel , F. Schmidl , V. Grosse , S. Döring , S. Schmidt, M. Kidszun* , S. Haindl* , L. Schultz* , B. Holzapfel*

* *IFW Dresden, Institute for Metallic Materials, Helmholtzstrasse 20, 01069 Dresden, Germany*

The experimental investigation of the electronic properties of the just discovered Fe-based superconductors (pnictides) [1] is a helpful tool to investigate the nature of superconductivity in these materials. Tunnelling junctions and Josephson junctions offer ways to measure the energy gap and the symmetry of the order parameter as fundamental properties. If the symmetry of pairing differs from conventional s-wave the behaviour of these junction will change. There exist some theoretical works comparing different types of symmetry and the resulting properties like density of states of the quasiparticles, Andreev bound state, magnetic field dependence of Josephson current etc.

There are a lot of tunnelling junctions, mostly Andreev point contacts to study the iron-based superconductors, see e.g. [2] and references therein. Experimental results of point-contact Andreev-reflection (PCAR) on La-1111 ($T_c \sim 27\text{K}$) single crystals [3] clearly indicate the existence of two gaps of 3 and 8 meV, respectively. While the temperature of the larger one follows conventional s-wave behaviour the small one depends very unusual. For Sm-1111 ($T_c \sim 51\text{K}$) two gaps of about 6.5 and 17 meV were obtained by PCAR [4]. The theoretical modelling which leads to these gap values was based on our BTK model with lifetime extension [5] assuming two independent gaps and a simple superposition of the calculated conductance-voltage dependencies.

The first observations of Josephson effects were published but for only the 122-material. Zhang et al. [6] fabricated hybrid Josephson junctions with a conventional s-wave counter electrode (lead) and $\text{Ba}_{1-x}\text{K}_x\text{Fe}_2\text{As}_2$ (122) single crystals (T_c about 20 K) in c-direction. The Pb electrode

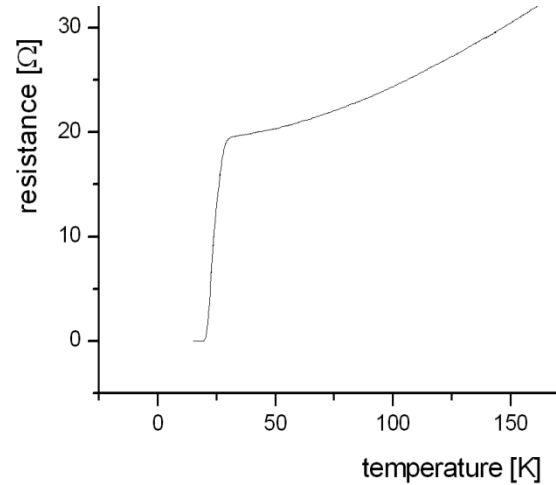


Fig.1: $R(T)$ of the patterned La-1111 basis electrode.

was used in two geometries, point contact tip and planar thin film of PbIn, respectively. This group just demonstrates an all pnictide Josephson junction produced by crossing two different doped 122 single crystals [7]. Another experiment on a hybrid junction was realized by Zhou et al. [8] where a $\text{BaFe}_{1.8}\text{Co}_{0.2}\text{As}_2$ single crystal ($T_c = 22\text{K}$) was used. To test the order parameter symmetry a phase-sensitive corner junction coupling the a- and the b-direction via a conventional s-wave superconductor (Pb) was measured. For the 1111-material there exist first measurements of c-axis transport by the group of Paul Müller [9]. They prepared mesa structures from single crystals of $\text{LaO}_{0.9}\text{F}_{0.1}\text{FeAs}$ and observed I-V characteristics of overdamped Josephson junctions with $I_c R_n$ products of about $10 \mu\text{V}$.

Since there are no high quality superconducting single crystals of the $\text{LaFeAsO}_{1-x}\text{F}_x$ (1111) phase available so far, the deposition of thin films opens the way

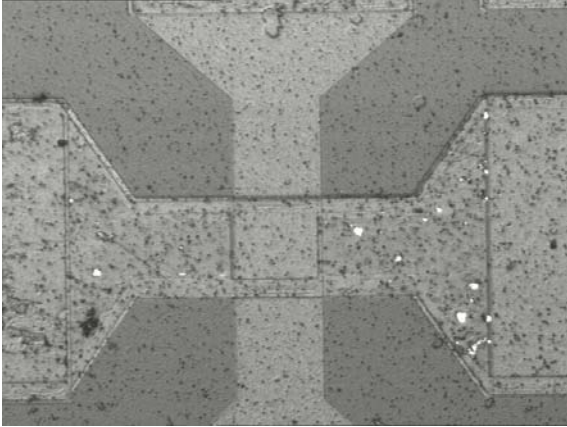


Fig.2: Microscope picture of a La-1111 bottom electrode crossed by a PbIn counter electrode.

for fundamental experiments on superconductivity in the iron pnictides. In co-operation with the IFW Dresden we prepared hybrid Josephson junctions with their La-1111 thin films prepared by PLD [10]. The pnictide film was covered by Au, than patterned by photolithography and etched with dry Argon. In the resulting base electrode a window for the junction was realized using sputtered SiO₂ insulation. The measurement of the resistive transition showed no depression of the T_c~20 K of the pnictide, Fig.1.

In the next step a PbIn counter-electrode (T_c~7K) was prepared by thermal evaporation through a mask in crossed geometry. A photograph of the junction is given in Fig.2. The electrical measurements of the junction are in progress and first results were reported at ISS'09 [11]. Fig.3 shows typical I-V characteristics at different temperatures close to T_c of the involved superconductors. We observed tunnel-like behaviour, but with no occurrence of a supercurrent through the junction. At this stage of experimental investigations the gold barrier is yet too thick to allow Josephson effects. Thinner and well-defined barriers, however, are only obtainable if surface roughness is reduced significantly.

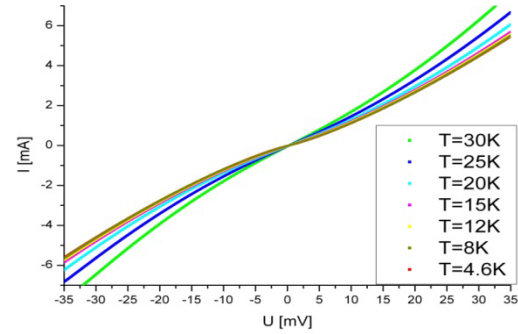


Fig.3: Current-voltage characteristics of a tunnel junction at different temperatures.

Therefore, further technological improvements on film growth and sample preparation are necessary.

References

- [1] Y. Kamihara, T. Watanabe, M. Hirano, H. Hosono, *J. Am. Chem. Soc.* 130 (2008) 3296
- [2] K. A. Yates et al., *Supercond. Sci. Technol.* 23 (2010) 022001
- [3] R. S. Gonelli et al., *Cent. Eur. J. Phys.* 7(2009) 251.
- [4] J. Karpinski et al., *Physica C* 469 (2009) 370.
- [5] Plecenik A, Grajcar M, Benacka S, Seidel P, Pfuch A, *Phys. Rev. B* 49 (1994) 10016.
- [6] X. H. Zhang et al., *Phys.Rev.Lett.* 102 (2009) 147002.
- [7] X. H. Zhang et al., *Appl. Phys. Lett.* 95 (2009) 062510
- [8] Y. R. Zhou et al., arXiv: 0812.3295 (2009).
- [9] P. Müller et al., *Verhandl. DPG TT 36.7* (2009)
- [10] M. Kidszun, S. Haindl, E. Reich, J. Hänisch, K. Iida, L. Schultz, B. Holzapfel, *Supercond. Sci. Technol.* 23 (2010) 022002.
- [11] M. Kidszun S. Haindl, A. Kauffmann, K. Nenkov, T. Thersleff, N. Kozlova, J. Freudenberger, J. Werner, E. Reich, L. Schultz, F. Schmidl, P. Seidel, B. Holzapfel, *Proc. of 22nd Internat. Symp. Supercond. ISS 2009*, Tskuba, Nov. 2-4, 2009.

Measurements of insulating structures for growth of carbon nanotubes

B. Voigt, P. Heisel, C. Katzer, F. Schmidl and P. Seidel

Introduction

Most important for measurements on electrical devices as well as carbon nanotubes is a working layer system. To separate and insulate the tubes from the substrate a silicon dioxide layer is included in the system. One also needs a catalyst in form of clusters for the growth of CNTs. To avoid that the clusters diffuse through the insulator and create a parallel current flowing over the substrate, we have done investigations on a simple layer system made of silica as substrate and silicon dioxide. Figure 1 shows a schematic setup. The SiO_2 layers have three different thicknesses. The smallest is 100nm, another one is 200nm thin and thickest layer consist of 300nm of SiO_2 . On the top are structured gold pads to contact the layer system to the measurement setup.

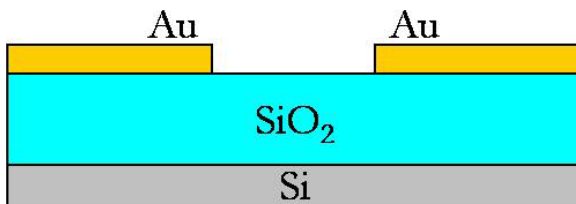


Fig. 1 Layer system of silicon dioxide on a silica substrate and gold on top as contacting material

The lowest resistance of a single-walled carbon nanotube theoretically is $6,5\text{k}\Omega$. If contacts are made by gold, the resistance of the whole device will be up to 100Ω . [1] So the resistance between two contact pads should be at least over $1\text{M}\Omega$, which means a potential parallel current through the layer system is suppressed to an insignificant minimum.

Measurements

All samples were characterized in a voltage range from -1V to $+1\text{V}$. Figure 2 shows an example of a current-voltage characteristic. If you change it into a voltage-current dependency and derivate it, you will get the differential resistance. Due to the expectedly high resistance and the

resolution of the digital measurement setup a jumping of the current occurs. Hence, a typical tunnel junction dependency is plotted, which easily can be derivated.

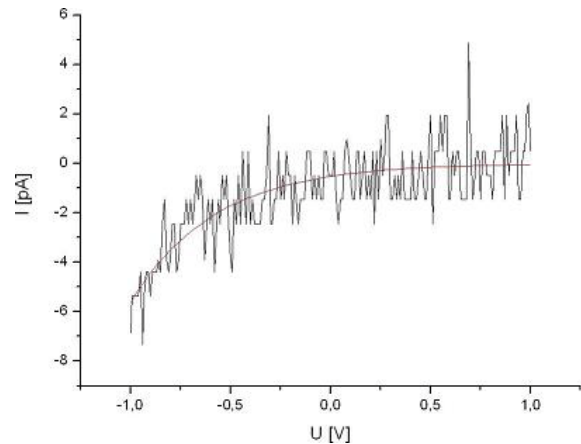


Fig. 2 Current-voltage characteristic of a sample with a fit of a tunnel junction

The measurements of almost all samples have shown that the minimum resistances of the layer systems were in the range from $1,5\text{M}\Omega$ to $75\text{G}\Omega$. Just two of the samples showed smaller values by Ω 340k respectively $91\text{k}\Omega$. This might result from worse conditions while processing the layers. The thickness of the SiO_2 layer has no bearing on the resistance.

Conclusion

We could prove that already 100nm of silicon dioxide satisfactory insulates in a voltage range from -1V to $+1\text{V}$. The next step will be putting cobalt on the SiO_2 layer. Cobalt provides us the catalyst. Due to the cluster form it more likely diffuses through the insulator. So we will build a sandwich system with SiO_2 at the bottom and the top over a titanium layer which shall stop diffusing clusters.

References

[1] B. Babic et al., Suitability of carbon nanotubes grown by chemical vapor deposition for electrical devices, Dissertation, University of Basel, 2004

Electronic Spectroscopy of Polycyclic Aromatic Hydrocarbons Isolated in Solid Neon

M. Steglich, C. Jäger, G. Rouillé, and F. Huisken

Absorption spectroscopy in the UV and visible wavelength ranges is used to probe the electronic structure of molecules, small clusters, or radicals. Often, one wants to study species under isolated conditions, i.e., the molecules to be investigated are separated from each other in order to avoid molecular interactions. For instance, this is important if one wants to compare laboratory spectra with absorption or emission features of astrophysical objects. In the interstellar medium, species of interest are free-flying molecules and clusters which do not interact with each other and which are often at very low temperature. Usually, molecular interactions lead to a broadening and red-shift of the absorption (or emission) bands. To avoid such effects, species have to be investigated in supersonic jets [1] or in inert rare-gas matrices at low temperature. The latter technique is referred to as matrix isolation spectroscopy (MIS, Fig. 1).

An important advantage of MIS is that species whose vapor pressure is too low to carry out absorption measurements in supersonic jets, e.g., large polycyclic aromatic hydrocarbons (PAHs, see Fig. 2), may be studied since they can be accumulated. Moreover, as the molecules are trapped in the matrix, time-consuming measurements such as those involving scans over broad wavelength ranges can be performed without consuming much sample. This is an important point because the available amount of sample is often limited. Due to the cryogenic temperature, only the lowest-energy levels of the molecules are populated, resulting in spectra typical for cold molecules.

Our main interest in PAHs arises from their presumably high abundance in the interstellar medium. Especially in the visible and near-UV, astronomers observed a few absorption and emission features that still lack a proper identification, and PAHs are discussed as possible carriers. Furthermore, related aromatic molecules have a substantial relevance in opto-electronics, e.g., in organic light-emitting diodes or in the newly

drocarbons (PAHs, see Fig. 2), may be studied since they can be accumulated. Moreover, as the molecules are trapped in the matrix, time-consuming measurements such as those involving scans over broad wavelength ranges can be performed without consuming much sample. This is an important point because the available amount of sample is often limited. Due to the cryogenic temperature, only the lowest-energy levels of the molecules are populated, resulting in spectra typical for cold molecules.

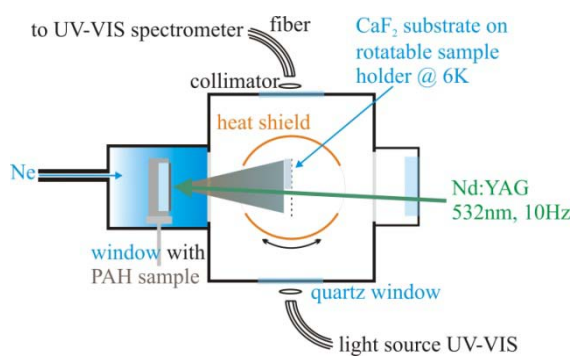


Fig. 1: Schematic view of the setup for matrix isolation spectroscopy. The vaporization of the species to be studied can be performed with a laser as shown here or by thermal evaporation in a small oven.

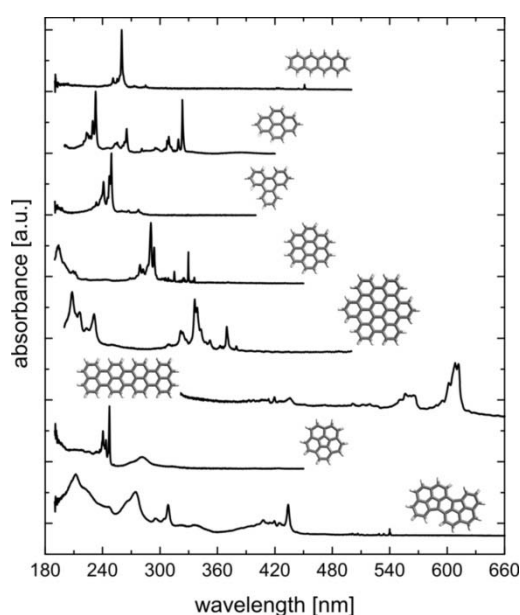


Fig. 2: Electronic absorption spectra of selected PAHs isolated in neon at 6 K [2,3,4].

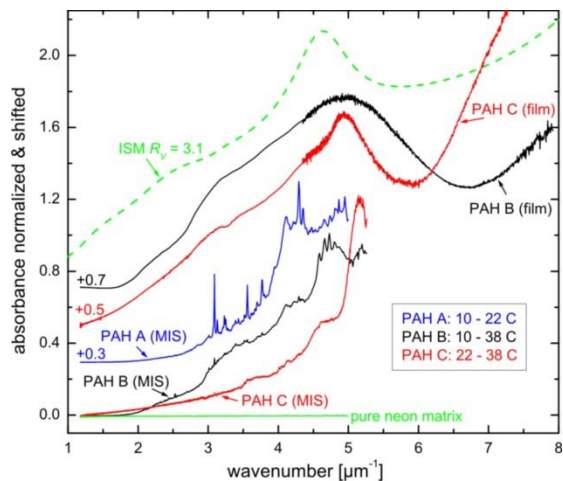


Fig. 3: Measured spectra of PAH mixtures with different size distributions. Molecules have been deposited as films or were isolated in neon (MIS), respectively [5].

emerging field of graphene research.

Recently, we have measured spectra of different mixtures of mainly medium-sized PAHs [5], i.e., PAHs containing about 10 to 38 carbon atoms (mixtures A, B, C in Fig. 3). These PAH mixtures have been produced with laser pyrolysis. This technique produces condensation products which are very similar to primary cosmic carbonaceous matter, condensing in the envelopes of asymptotic giant branch stars [6]. We also measured spectra of film-like deposits characterized by strong molecular interactions similar to those expected in PAH clusters bonded by van der Waals forces. In the ISM, the presence of such clusters has been inferred from rather broad mid-IR emission features with a strong continuum [7]. Clusters of PAH mixtures exhibit spectral similarities to nano-sized carbonaceous particles showing a pronounced UV bump. Its width and shape for PAH films containing more than 22 C atoms are nearly comparable to the interstellar extinction curve. However, its position is mainly determined by the mean size of the comprising PAHs. Based on calculations (Fig. 4), we expect a red shift of the experimental bump position for larger PAHs and we propose that a distribu-

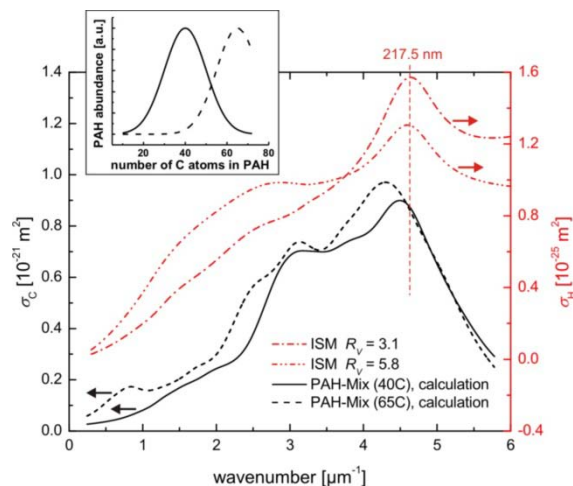


Fig. 4: Simulated spectra of films of PAH mixtures with different size distributions compared with the mean interstellar extinction for two different reddening parameters. For the calculation, a semi-empirical approach was used [5].

tion of molecules with a mean size of 50 to 60 carbon atoms can produce a bump close to 217.5 nm, the position of the bump in the interstellar extinction curve. This would be consistent with the expected size of interstellar PAHs obtained from the mid-IR emission bands [7]. Smaller molecules, which are formed in large quantities in condensation processes in the laboratory and, probably, in astrophysical environments, are believed to be destroyed by interstellar radiation.

References

- [1] M. Arold, G. Rouillé, Th. Henning, F. Huisken, Annual Report 2008.
- [2] G. Rouillé, M. Steglich, F. Huisken, Th. Henning, K. Müllen, J. Chem. Phys. 131 (2009) 204311.
- [3] G. Rouillé, C. Jäger, M. Steglich, F. Huisken, Th. Henning, G. Theumer, J. Bauer, H.-J. Knölker, Chem. Phys. Chem. 9 (2008) 2085.
- [4] G. Rouillé, M. Steglich, F. Huisken, H.-J. Knölker, in preparation.
- [5] M. Steglich, C. Jäger, G. Rouillé, F. Huisken, H. Mutschke, Th. Henning, Astrophys. J. Lett. in press.
- [6] C. Jäger, I. Llamas, H. Mutschke, F. Huisken, Annual Report 2007.
- [7] A. G. G. M. Tielens, Ann. Rev. Astron. Astrophys. 46 (2008) 289.

Oxidation Reactions in Helium Droplets at $T = 0.37$ K

Serge Krasnokutski and Friedrich Huisken

Despite the low temperatures encountered in the ISM and in interstellar clouds, there is strong evidence of a rich gas-phase chemistry taking place in these environments. It has been shown that, in general, the extrapolation of high-temperature reaction rates to low-temperature values yields incorrect results. Therefore, it is actually necessary to study the reaction kinetics at low temperatures in the laboratory. This data is urgently needed to explain astronomical observations and to provide input data for astrochemical models.

The most widely used technique to cool gase-phase molecules to temperatures in the order of 10 K is the molecular beam technique based on supersonic jet expansions. However, this method has the disadvantage that the temperature is not unique for all degrees of freedom. Another method to provide cryogenic temperatures but to keep all degrees of freedom in equilibrium is the matrix isolation technique. Here, the disadvantage is that the reactants are locked in the solid matrix and cannot move freely. A third method combining the advantages of both methods is the helium droplet technique which has been explored and developed only very recently [1].

Incorporating two different species A and B into the helium droplet, it is possible to study the reaction between A and B at the ultralow temperature of 370 mK. The simplest way to monitor the reaction is the de-

tection of the products in a mass spectrometer. Another possibility is to detect electronically excited products by measuring the chemiluminescence (CL) light emitted by the hot products. We have used these techniques to study the oxidation reactions of a number of period 3 elements of significant universal abundance (Mg, Si, and Al) with O_2 .

Experiment

A schematic view of the experimental setup is shown in Fig. 1. The helium droplet beam enters the reaction chamber through the skimmer. Mg (or Si or Al) atoms are incorporated by passing the helium droplets just above a crucible where the respective material is evaporated. The second reactant (O_2) is incorporated further downstream by crossing the helium droplet beam with an effusive beam of O_2 . The CL photons generated from electronically excited product molecules are collected by a fiber that can be moved in x- and y-direction and that is coupled to a photomultiplier. Alternatively, the product molecules remaining in the helium droplets or being expelled in forward direction can be detected with a mass spectrometer.

Results

A two-dimensional image of the CL light generated upon the reaction of Mg complexes with O_2 molecules is shown in Fig. 2. The x-coordinate refers to the direction of the helium droplet beam while y indicates the direction perpendicular to it. The interaction with O_2 molecules occurs at $x = 0$ mm. When O_2 is replaced by Ne or N_2O no chemiluminescent light is observed. The observation of CL in general and the emission pattern in particular prove that (i) the

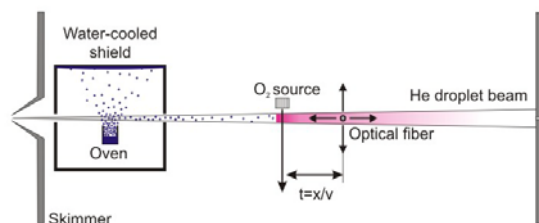


Fig. 1: Schematic view of the experimental setup.

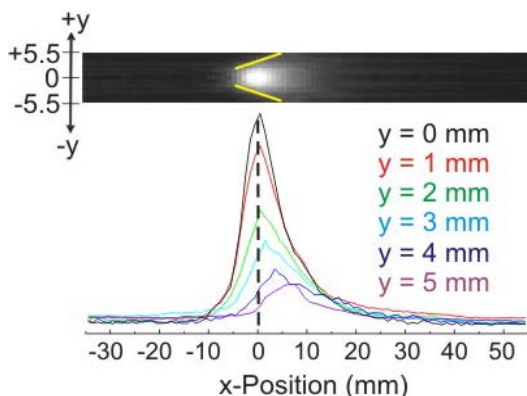


Fig. 2: Two-dimensionally resolved CL signal produced in the reaction between Mg complexes and O_2 molecules.

chemical reaction takes place with O_2 , (ii) up to 3.1 eV are released by the photons (as revealed by measuring the emission spectrum), (iii) the products are expelled from the helium droplets, and (iv) the CL rate is much slower than the reaction rate (as evidenced by the diverging CL pattern). The CL study allows an evaluation yielding an upper limit for the reaction time constant. It is found that the reaction between Mg complexes and O_2 molecules is completed within the first 100 μ s after the incorporation of O_2 . Thus, we conclude that this reaction may be relevant for the ISM.

Filling the empty p-orbital of the Mg atom with one or two electrons results in the formation of Al or Si atoms, respectively. It will be interesting to see how this change in the electronic configuration will affect the chemical properties of the elements at low temperatures. The mass spectrometric studies of the reactions $Mg + O_2$ and $Si + O_2$ yield similar mass spectra. At low metal vapor pressure, no products are seen in the mass spectra. We only observe the depletion of the reactant's mass peaks indicating that the products are expelled from the beam. Only if the metal vapor pressure is increased such that metal clusters are formed, we do see products of the form M_xO_y (see Fig. 3). In contrast, the incorporation of Al atoms and O_2 molecules does

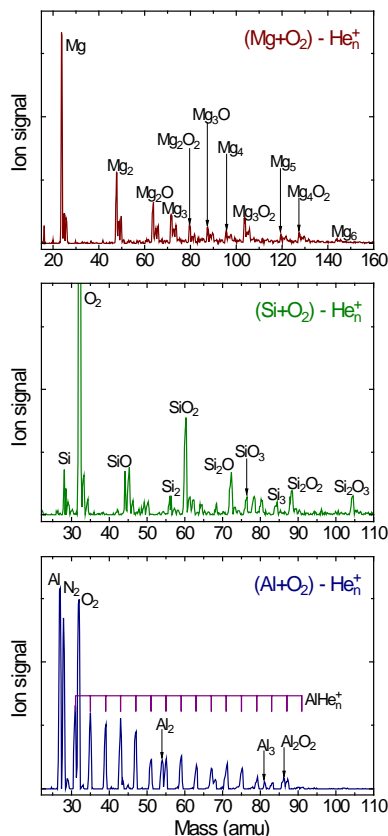


Fig. 3: Mass spectra resulting from the reactions of Mg, Si, and Al atoms with O_2 .

not yield any chemical reaction. The only peak related to an oxide, Al_2O_2 , should be attributed to the formation of a van der Waals complex. At the same time, the Al^+ cation produced in the ionizer easily forms complexes with He atoms yielding $AlHe_n^+$ with n up to 16. The present studies allow us to conclude that the reactions of O_2 with Mg and Si atoms or clusters proceed rather fast at 370 mK [2]. On the other hand, Al atoms or clusters do not react with O_2 at this temperature. These findings are confirmed by monitoring the evaporation of He atoms from the droplets, thus providing information on the energy released during the chemical reaction.

References

- [1] C. Jäger et al., *Astrophys. J. Suppl. Ser.* 166 (2006) 557.
- [2] S. Krasnokutski, F. Huisken, *J. Am. Chem. Soc.* (2010) in preparation.

X-ray photoelectron diffraction: A tool for the structure analysis of ultra-thin epitaxial layers

Bernd Schröter and Aimo Winkelmann*

* *Max-Planck-Institut für Mikrostrukturphysik, Weinberg 2, 06120 Halle*

Electron diffraction methods are well suited to analyse the atomic structure of ultrathin films because of the short information depth attainable with low and medium energy electrons. To be sensitive to a unit-cell size of common crystals the electron diffraction effects have to extend to a depth of a few nanometers. This corresponds to electron energies near 1 keV. One can use elastically scattered electrons from an external source or electrons which are excited inside the thin film to be analysed. For instance, low-energy electron diffraction (LEED) and diffraction of photoelectrons excited by x-rays (XPD) as well as the analysis of back-scattered electrons (electron channeling patterns and electron backscatter diffraction (EBSD)) can be used. In MBE growth experiments, reflected high-energy electron diffraction (RHEED) is applied. Especially, X-ray excited photoelectron spectroscopy (XPS) has proven sensitive to the crystal structure and the polarity of attractive materials like silicon carbide poly-

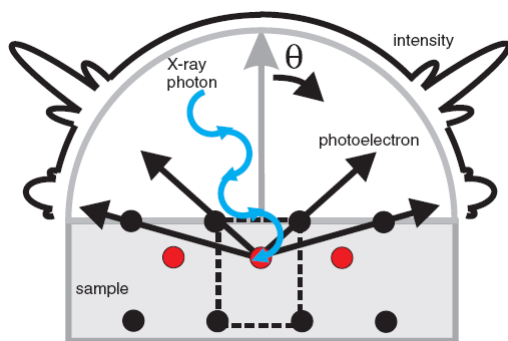


Figure 1: Principle of photoelectron diffraction

types or group-III nitrides [1-3]. A photoelectron which has been emitted by an atom can be scattered by the neighboring crystal atoms (figure 1). This causes variation of the photoelectron current depending on the emission angle and provides a possibility to analyze the crystal structure near the emitting atom. As a first approximation,

the emitted photoelectrons are scattered in the forward direction. Hence, emitter-to-scatterer directions show up as maxima in the angular photoemission intensity distribution, which offers a relatively easy interpretation of the resulting angular photoelectron distribution.

Our experimental set-up consists of an x-ray source with an Al/Mg twin anode (1486eV and 1254 eV; respectively) and a concentric hemispherical electron analyser. The sample can be rotated in polar and azimuth directions to acquire a number of angular-resolved photoelectron spectra. The signal intensities are plotted either as a 1D polar plot or a 2D stereographic projection (figure 2).

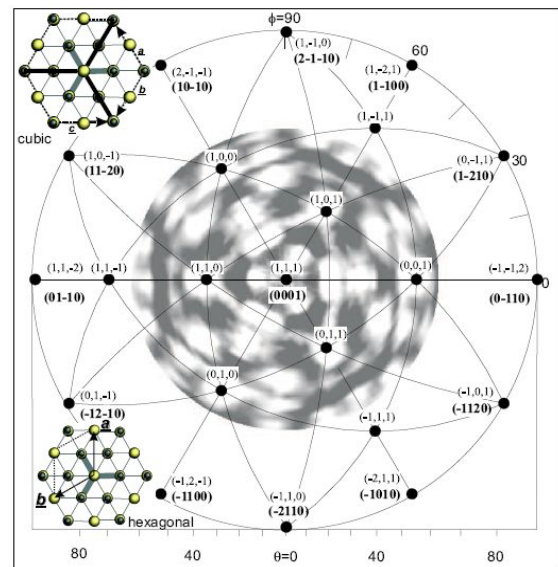


Figure 2: Stereographic projection of Si 2p photoelectron intensities of 3C SiC(111)

XPD has been extensively used to determine the polytype structure and polarity of ultra-thin SiC and AlN films grown by molecular beam epitaxy (MBE) [1-3]. A medium-energy XPD pattern is sensitive to the atomic stacking of more than 10 monolayers and hardly affected by surface reconstruction or contamination. Thus, a clear

fingerprint-like identification of the structure and polarity is possible for a film only few nanometers thick. The diffraction patterns are well described by single-scattering cluster (SSC) theory and dynamical theory which allows the simulation of XPD patterns on any stacking sequences [3].

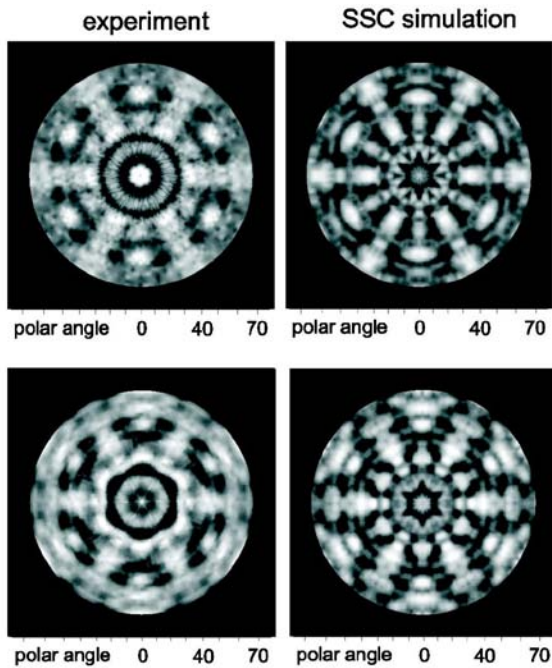


Figure 3: Al 2p ($E = 1413\text{eV}$) XPD patterns of AlN {0001}, N face (top) and Al face (bottom) [3]

The nondestructive identification of the polarity of epitaxial layers is a useful application of XPD [1-3]. Compound semiconductors exhibit different polar surfaces in certain growth directions, e.g., AlN or SiC grown on Si(111) substrates. In a recent paper by Pezoldt et al. [4], XPD has been used to demonstrate the controlled formation of different crystallographic polarities of 3C-SiC on Si(111) (figure 3). A carbonization by depositing elemental carbon under ultra-high vacuum conditions (SSMBE) or alternatively at atmospheric pressure in a rapid thermal chemical vapor deposition (RTCVD) reactor results in different polar surfaces of the cubic SiC{111} film. In figure 4 the Si 2p to C 1s intensity ratios determined from the experimental polar angle scans in (2-1-1) azimuth direction reveal the forward scattering intensities typical for the Si and C face of cubic SiC, respectively.

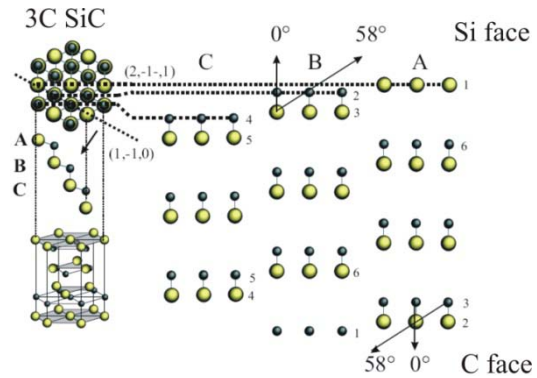


Figure 4: Photoelectron forward-scattering directions allow an identification of the polar faces of thin SiC films

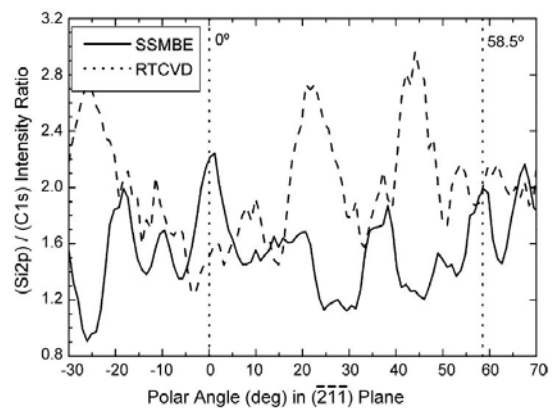


Figure 5: XPD Si 2p to C 1s intensity ratios determined from the experimental polar scans on SiC films grown by two different carbonization techniques on Si(111) [4]

References

- [1] B. Schröter, A. Winkelmann, W. Richter „X-ray photoelectron diffraction on SiC and AlN epitaxial films: polytype structure and polarity” *Journal of Electron Spectroscopy and Related Phenomena* 114-116 (2001) 443.
- [2] A. Winkelmann, B. Schröter, W. Richter „Electron diffraction methods for the analysis of silicon carbide surfaces and the controlled growth of polytype heterostructures“ *J. Phys.: Condens Matter* 16 (2004) S1555.
- [3] A. Winkelmann, B. Schröter, W. Richter „Simulation of high energy photoelectron diffraction using many-beam dynamical kichu-band theory” *Physical Review B* 69 (2004) 245417.
- [4] J. Petzoldt, T. Kups, T. Stauden, B. Schröter „Polarity determination and control of SiC grown on Si“ *Materials Science and Engineering B* 165 (2009) 28.

Optical differential reflectance spectroscopy of ultrathin epitaxial organic films

Roman Forker* and Torsten Fritz

* *Institut für Angewandte Photophysik, Technische Universität Dresden, 01062 Dresden*

Research carried out in the field of organic thin films is essentially stimulated by their potential applications in molecular electronics. A few nanometers thick layers piled up in sequential structures are especially interesting since light-emitting diodes (OLED) and photovoltaic devices (OPVD) based on this architecture have already been realized and are expected to rapidly gain market share.

The examples named above for up-to-date devices convert light into free charge carriers or vice versa. The interplay of organic semiconductors and their electronic and optical properties is therefore of accentuated importance. While the lowest unoccupied molecular orbital (LUMO) and the highest occupied molecular orbital (HOMO) of the respective molecular solids can be examined using photoelectron spectroscopies, only optical spectroscopy can clarify the light absorption and emission behavior, as electronic gap (electronic gap = LUMO – HOMO) and optical gap differ by the exciton binding energy which can be as large as 1 eV.

Quite fortunately, the special properties of ultrathin molecular layers make those a very good object for optical spectroscopy studies: First, organic molecules tend to have very high absorption coefficients offering outstanding sensitivity even for small amounts of material. Second, the light absorption depends sensitively on the morphology of the analyzed sample. Caused by the non-spherical shape of most molecules, the lateral packing of a deposited layer usually differs drastically from the vertical packing. This fact opens up a path to follow

the film growth with excellent thickness-precision, as the set-in of the vertical π - π -interaction upon completion of the very first monolayer (ML) will manifest itself in a characteristic alteration of the optical spectra. Third, the optical response is sensitive to the arrangement of molecules in the film. Finally, optical spectroscopy is non-destructive and can therefore be employed during film growth without noticeable impact on the latter.

The method of choice is the differential reflectance spectroscopy (DRS) which we will briefly discuss here. DRS arises from common reflectivity measurements. It is simply defined as:

$$\text{DRS} \equiv \frac{\Delta R}{R}(E, d) := \frac{R(E, d) - R(E, 0)}{R(E, 0)}, \quad (1)$$

utilizing the change in reflectance between a sample with ($R(E, d)$, d = film thickness) and without ($R(E, 0)$) adsorbate, normalized by $R(E, 0)$ [1]. By convention, we consider the spectral dependence as a function of photon energy $E = \hbar\omega$. One can continuously record the reflectance starting from a clean substrate and going on while depositing the material on the surface. This is what makes real-time *in situ* growth studies feasible.

Our apparatus (Fig. 1) consists of three separately pumped ultrahigh vacuum (UHV) chambers. A fast load-lock and an analysis chamber equipped with a scanning tunneling microscope (STM) are mounted to the main chamber, which itself contains all necessary components for film growth and *in situ* optical spectroscopy.

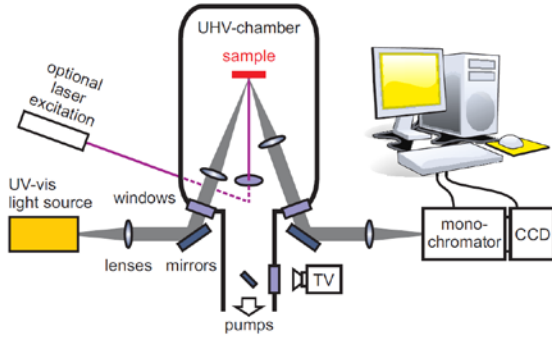


Fig. 1 Sketch of the experimental setup realized in our laboratory. Details are described in [2].

The definition of the DRS (eq. (1)) given above can not self-explanatorily be attributed to any optical quantity characterizing the adsorbate, since it contains both the reflectance of the bare substrate $R(E,0)$ and that of the substrate covered with the adsorbate $R(E,d)$. Several publications have shown that the DRS can easily be linearized in the case of an ultrathin ($d \ll \lambda$, λ being the wavelength of the incident light) film on a semi-infinite substrate, i.e., the reflection of the substrate's backside is not detected. For normal incidence of light (nearly fulfilled in our setup) one arrives at the following expression:

$$\text{DRS} \equiv \frac{\Delta R}{R} \approx -\frac{8\pi d}{\lambda} [A \times \varepsilon''_{\text{film}} + B \times (\varepsilon'_{\text{film}} - 1)] \quad (2)$$

We define the complex dielectric function as $\hat{\varepsilon} = \varepsilon' - i\varepsilon'' \equiv \hat{n}^2 = (n - ik)^2$. As a first important statement we see the proportionality of the DRS to the film thickness d , provided that the dielectric function of the film $\hat{\varepsilon}_{\text{film}}$ remains unchanged with increasing layer thickness. The exclusively substrate-dependent functions A and B can easily be computed from n - and k -values for the respective substrates. Under the condition that $|A| \gg |B|$ one can further simplify eq. (2) as:

$$\text{DRS} \equiv \frac{\Delta R}{R} \approx -\frac{8\pi d}{\lambda} \times A \times \varepsilon''_{\text{film}} \quad (3)$$

Thus, the DRS is proportional to the imaginary part $\varepsilon''_{\text{film}}$ of adsorbate film in this special case. $|A| \gg |B|$ holds for transparent substrates. Hence, the DRS is actually a variant of absorption spectroscopy rather than a pure reflection measurement.

For the overwhelming part of opaque substrates, one can not draw such an effortless conclusion as both A and B contribute non-negligibly to the DRS. In this case one has to calculate the complex dielectric function of the film from the DR spectra using a numerical algorithm which allows to extract the two optical functions n and k of the film via exploitation of the Kramers-Kronig transformation from only one spectral measurement [3].

Meanwhile this method has been applied successfully to numerous cases from organic-inorganic heteroepitaxy on insulators and conductors to organic-organic heteroepitaxy. For an overview see [4], and references therein.

The authors acknowledge financial support from the Deutsche Forschungsgemeinschaft (grants No. FR 875/6, FR 875/9, FR 875/11). R.F. was supported by the Studienstiftung des deutschen Volkes.

References

- [1] J. D. E. McIntyre and D. E. Aspnes, Surf. Sci. **24** (1971) 417-434.
- [2] H. Proehl, R. Nitsche, T. Diemel, K. Leo and T. Fritz, Phys. Rev. B **71** (2005) 165207.
- [3] R. Nitsche and T. Fritz, Phys. Rev. B **70** (2004) 195432.
- [4] R. Forker and T. Fritz, Phys. Chem. Chem. Phys. **11** (2009) 2142-2155.

Line-on-line organic-organic heteroepitaxy of QT on HBC on Au(111)

Daniel Kasemann*, Christian Wagner*, Roman Forker*, Thomas Diemel*, Klaus Müllen**, and Torsten Fritz

* *Institut für Angewandte Photophysik, Technische Universität Dresden, 01062 Dresden*

** *Max-Planck-Institut für Polymerforschung, Ackermannweg 10, 55128 Mainz*

The last years have witnessed huge interest in organic thin films, for both single molecular electronics and, more generally, organic-based devices consisting of several layers [1-3]. The investigation of highly ordered layers grown by organic molecular beam epitaxy (OMBE) represents a rewarding approach to achieve a better understanding of the physics at organic-organic and organic-inorganic interfaces. OMBE does not only provide well-defined and reproducible layer systems but also allows to prepare atomically thin organic films so that the processes occurring directly at the interface(s) can be studied in detail. Despite the fact that all *state-of-the-art* (opto-) electronic devices contain inorganic quantum wells (or at least epitaxial heterostructures), only little is known about true organic-organic heteroepitaxy, comprising subsequently grown epitaxial layers of two different organic species on a single crystalline substrate.

Only recently, a new type of epitaxy (line-on-line epitaxy, *lol*) has been discovered which explains the molecular arrangement in organic heteroepitaxial systems encompassing flat aromatic hydrocarbons [4,5]. It is important to note that this type of epitaxy can not be readily identified by the epitaxial matrix. To determine whether the overlayer is arranged according to *lol* epitaxy, the analysis of the reciprocal lattice vectors is required instead. For *lol*, one *arbitrary* reciprocal substrate lattice vector has to end on a reciprocal adsorbate lattice point. In real space *lol* epitaxy can be visualized by the coincidence of two higher indexed lattice lines (hence the name line-on-line).

Here we present the structural investigation of a new organic double layer system consisting of a highly ordered monolayer of quaterylene (QT) on an epitaxially grown monolayer of hexa-peri-hexabenzocoronene (HBC) on a Au(111) surface. The full report is in [6]. In a recent paper we have already discussed the optical properties of such a heterostructure [7].

HBC molecules grow flat-lying and in an almost hexagonal arrangement on the Au(111) substrate. They form large highly ordered domains at room temperature. Figure 1 shows an STM image with molecular resolution of one monolayer of HBC on the reconstructed Au(111) surface.

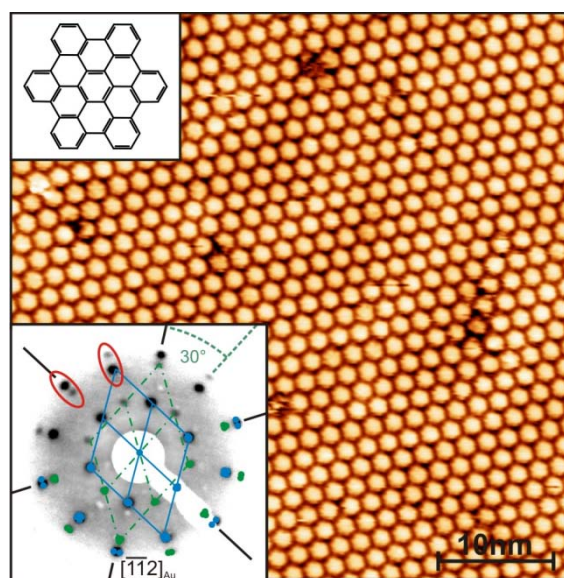


Fig. 1 STM image of an ordered monolayer of HBC on Au(111) ($50 \times 50 \text{ nm}^2$, 1 V, 50 pA). *Upper left corner*: skeletal formula of HBC. *Inset*: LEED pattern of a monolayer of HBC on Au(111) ($E_{\text{kin}} = 12.0 \text{ eV}$). The unit cells of the two domains are sketched (solid blue: “ 0° -structure”, dash-dotted green: “ 30° -structure”). The red circles highlight the $(1, \bar{1})_{0^\circ}$ and $(2, 0)_{30^\circ}$ spots and vice versa.

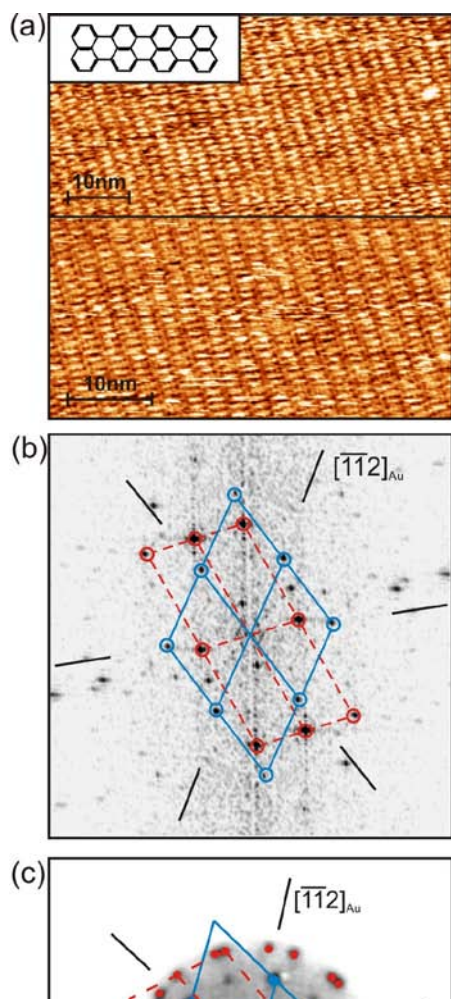


Fig. 2 (a) Two different STM images of an ordered monolayer of QT (the skeletal formula of QT is sketched in the upper left corner) on a monolayer of HBC on Au(111) ($66 \times 33 \text{ nm}^2$, 1.0 V, 75 pA and $48 \times 24 \text{ nm}^2$, 1.0 V, 55 pA, respectively). It clearly shows the molecular rows of QT similar to ref 22. (b) The FFT of the STM images (depicted here for the lower STM image in (a)) shows contributions of both the QT molecular lattice (red, dashed) and the hexagonal HBC lattice (blue, solid) to the STM image. This proves that the STM image indeed shows a double layer structure. (c) LEED pattern of such a double layer at an electron energy of $E_{\text{kin}} = 8.0 \text{ eV}$ with the unit cells of QT and HBC (blue solid: 0° -HBC phase, red dashed: QT). The spots between the blue HBC spots stem from the 30° -HBC structure (compare Fig. 1).

Next, this densely packed HBC monolayer on Au(111) was utilized as substrate, and one monolayer of QT molecules was deposited on top. Figure 2a shows STM images of the double layer system QT on HBC on Au(111). One can immediately identify the QT molecules grown densely packed in molecular rows similar to the structure known from the first QT monolayer on Au(111) [8]. The underlying HBC molecules are not evident at first glance. To identify the periodic structures contributing to the image one can employ fast Fourier transformation (FFT, Fig. 2b). The FFT reveals contributions of the ordered QT molecules (red, dashed), and the hexagonal structure of the HBC lattice (blue, solid). Figure 2c gives a typical LEED pattern of this double layer system.

In conclusion, we demonstrated the feasibility of growing well-ordered, truly heteroepitaxial layers with molecularly flat interfaces composed of structurally dissimilar organic molecules, namely QT and HBC.

The authors acknowledge financial support from the Deutsche Forschungsgemeinschaft (grants No. FR 875/6, FR 875/9, FR 875/11). R.F. was supported by the Studienstiftung des deutschen Volkes.

References

- [1] Forrest, S. R. *Nature* 2004, 428, 911-918.
- [2] Walzer, K.; Maennig, B.; Pfeiffer, M.; Leo, K. *Chem. Rev.* 2007, 107, 1233-1271.
- [3] Koch, N. *ChemPhysChem* 2007, 8, 1438-1455.
- [4] Mannsfeld, S. C. B.; Leo, K.; Fritz, T. *Phys. Rev. Lett.* 2005, 94, 056104.
- [5] Mannsfeld, S. C. B.; Fritz, T. *Mod. Phys. Lett. B* 2006, 20, 585-605..
- [6] Kasemann, D.; Wagner, C.; Forker, R.; Dienel, T.; Müllen, K.; Fritz, T. *Langmuir* 2009, 25(21), 12569-12573.
- [7] Forker, R.; Kasemann, D.; Dienel, T.; Wagner, C.; Franke, R.; Müllen, K.; Fritz, T. *Adv. Mater.* 2008, 20, 4450-4454.
- [8] Franke, R.; Franke, S.; Wagner, C.; Dienel, T.; Fritz, T.; Mannsfeld, S. C. B. *Appl. Phys. Lett.* 2006, 88, 161907.

3. Technical reports and equipment

Operation of the Ion-accelerator JULIA and the Ion-implanter ROMEO

U. Barth, F. Jehn, G. Lenk, W. Wesch, C. Ronning

The 3 MV high current tandetron accelerator **JULIA** (Jena University Laboratory for Ion Acceleration) went in operation end of 1996. Since the beginning of the routine-operation in 1997 it has been used for different types of experiments requiring a broad spectrum of ion-beams. With the exception of helium, where the duoplasmatron ion-source followed by a lithium exchange channel was used, all ions were extracted from a sputter-type ion-source. The beam-on-target-time of 1528 h was about 20% higher than in 2008. The 400 kV ion-accelerator **ROMEO** is in routine operation since 1998, here the beam-on-target-time of 1230 h was in the same order of magnitude as in the preceding years.

Both accelerators can be operated separately or in combination. The ion-beams produced until 2009 are summarized in table 1. The ion-beam currents quoted are typical values of the ion source currents used for the experiments, the maximum currents available are significantly higher for most ions.

In 2009 some components of the 3 MV-Tandetron accelerator „JULIA” and of the 400 kV Ion-Implanter „ROMEO” were further developed:

1. The +30° beam line of the ion accelerator „JULIA” as well as the chamber for PIXE-analysis were equipped with a computer-controlled beam-position steering system. New hard- and software, specifically developed, allows to adjust the angle and position of the ion beam.

2. The implantation chamber of the ion accelerator Julia was equipped with a radiation monitor. This allows performing experiments in which neutrons and gamma-rays are produced: an automatic shutdown of the terminal voltage ensures that maximum permissible radiation levels are not exceeded.

Table 1. Ion-beams accelerated during 2009. The currents given are measured at the Q-Snout-Faraday-cup after the low-energy mass separator (JULIA) and at the target position (ROMEO), respectively.

Period	Element	Julia	Romeo
1	Hydrogen (H)	5 μ A	4 μ A
	Helium (He)	0,2 μ A	4 μ A
2	Lithium (Li)	2 μ A	1 μ A
	Boron (B)	0,2 μ A	5 μ A
	Carbon (C)	9 μ A	1 μ A
	Nitrogen (N)	10 μ A	4 μ A
	Oxygen (O)	17 μ A	2 μ A
	Neon (Ne)	-	5 μ A
3	Sodium (Na)	-	6 μ A
	Magnesium (Mg)	-	5 μ A
	Aluminium (Al)	-	4 μ A
	Silicon (Si)	16 μ A	4 μ A
	Phosphorus (P)	-	4 μ A
	Argon (Ar)	-	20 μ A
4	Potassium (K)	-	3 μ A
	Calcium (Ca)	-	5 μ A
	Titanium (Ti)	0,7 μ A	-
	Vanadium (V)	0,2 μ A	1 μ A
	Manganese (Mn)	0,017 μ A	5 μ A
	Chromium (Cr)	0,2 μ A	3 μ A
	Iron (Fe)	0,8 μ A	2 μ A
	Cobalt (Co)	-	3 μ A
	Nickel (Ni)	-	6 μ A
	Zinc (Zn)	1 μ A	6 μ A
	Gallium (Ga)	1 μ A	3 μ A
	Germanium (Ge)	1,6 μ A	4 μ A
	Arsenic (As)	0,4 μ A	1 μ A
	Selenium (Se)	0,5 μ A	1,5 μ A
	Bromine (Br)	19 μ A	8 μ A
Krypton (Kr)	-	10 μ A	
5	Rubidium (Rb)	0,075 μ A	1 μ A
	Strontium (Sr)	-	3 μ A
	Yttrium (Y)	-	4 μ A
	Zirconium (Zr)	0,3 μ A	1,5 μ A
	Rhodium (Rh)	0,2 μ A	-
	Palladium (Pd)	0,095 μ A	1 μ A
	Silver (Ag)	-	10 μ A
	Cadmium (Cd)	-	0,8 μ A
	Indium (In)	5 μ A	8 μ A
	Tin (Sn)	-	3 μ A
	Antimony (Sb)	-	4 μ A
	Tellurium (Te)	-	2 μ A
	Iodine (I)	3 μ A	-
Xenon (Xe)	-	10 μ A	
6	Praseodymium (Pr)	-	1 μ A
	Neodymium (Nd)	-	0,5 μ A
	Samarium (Sm)	0,01 μ A	1,5 μ A
	Europium (Eu)	0,035 μ A	2 μ A
	Gadolinium (Gd)	0,03 μ A	-
	Erbium (Er)	0,04 μ A	2 μ A
	Tantalum (Ta)	0,2 μ A	2 μ A
	Tungsten (W)	0,3 μ A	0,01 μ A
	Osmium (Os)	0,05 μ A	-
	Iridium (Ir)	0,3 μ A	6 μ A
	Platinum (Pt)	0,2 μ A	-
	Gold (Au)	24 μ A	20 μ A
	Lead (Pb)	0,035 μ A	15 μ A
	Bismuth (Bi)	-	3 μ A

As in the preceding years the ion-beam facility was used by external research groups:

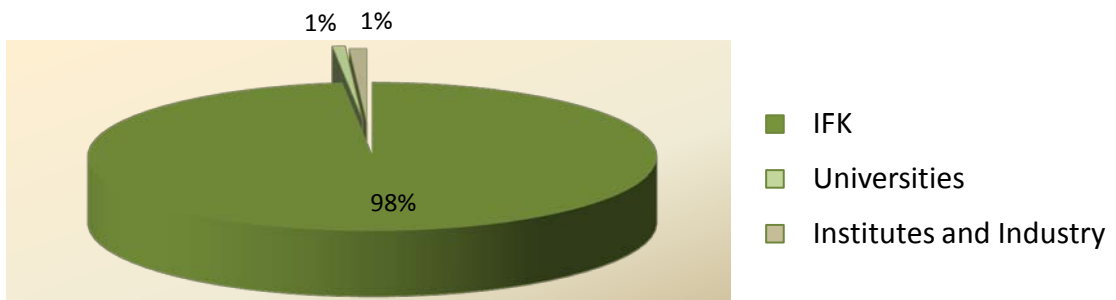
3MV-Tandetron „JULIA”

University Jena
University Freiberg (Dr. Bollmann)
IPHT Jena (Dr. Diegel)
Firma Layertec (Herr Heyer)

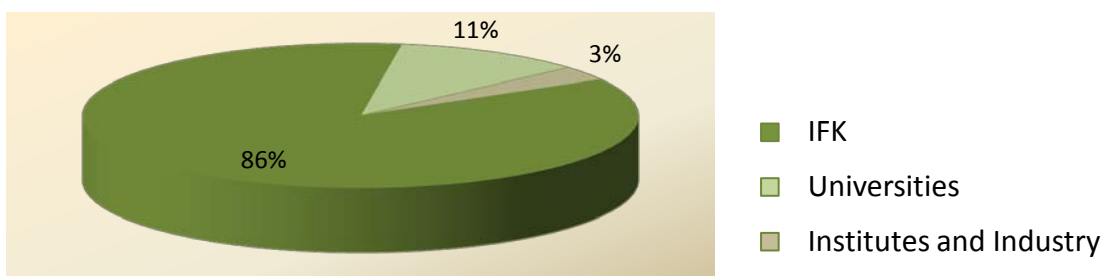
400kV Implanter „ROMEO“

University Jena
University of Pretoria (Prof. Malherbe)
University of Pretoria (Prof. Friedland)
IHP Jena (Herr Hartung)

3 MeV-Tandetron "JULIA"



400 kV Implanter "ROMEO"



Cryogenic Services 2009

All in-house customers of cryogenic liquids, which are all faculties of natural sciences, the medical division of the university, including several hospitals, and other external scientific institutes (e.g. Institute for Photonic Technology Jena, Leibnitz Institute Hans-Knöll Jena) as well as some private customers like the Innovent e.V. Jena or some medical practices were provided with liquid helium (LHe), high purity gases (He, N₂) and with liquid nitrogen (LN₂) by the Cryogenic Services. Nearly 87.000 litres of LN₂ were delivered by the cryogenic services this year.

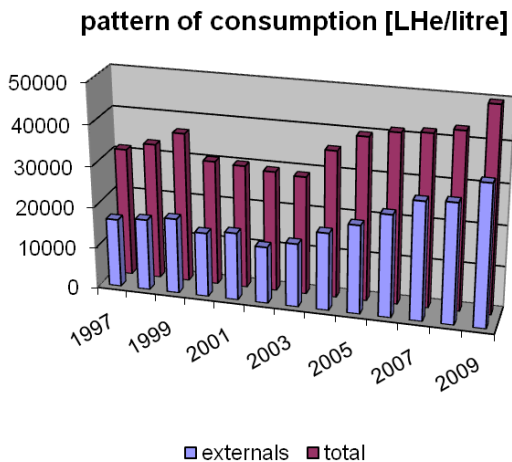


Fig. 1: Consumption of liquid helium

As illustrated in Figure 1, the production of LHe has increased in 2009 again. The high growth rate in 2009 was caused especially by the rising LHe- demands of the clinical users. In addition we were faced with LHe demands of a new NMR instrument in the Pharmaceutical Institute.

Roughly 49.500 litres of LHe were delivered which is by far the highest amount ever produced in the history of the Cryogenic Services Department. These results were achieved by the staff in spite of expanded reconstruction periods which were finished by the end of April 2009.

In the period under report our focus was on rebuilding the main helium liquefier and to stabilize the ongoing operations. The following sub-steps of the reconstruction were all accomplished on time:

- reconstruction of the water supply facility
- rebuilding of the electrical installation of the whole property
- workings on the building structure
- insertion of the 3.000 litre LHe-dewar
- mounting of a more powerful cycle compressor

- adjustment of the automatic process-oriented sequential control to implement the new components
- placement of the L70 cold-box, helium-purifier system, and plant control system
- pipe installation
- extension of the high-pressure storage capacity
- reconstruction of the refuel-area according to the legal requirements of the German Technical Inspection Authority

During the whole reconstruction period the stuff managed ongoing refrigeration operations without any breakdown of the LHe –delivery.

The commissioning of the instrument was proved successfully by the contractor in April 2009. All scheduled performance parameters of the instruments were accomplished by the LINDE AG. The most important value of the instrument, the liquefaction-rate, was projected with 26 litre/h. According to an announcement of the supplier we have increased this value by 3 litres/h. We acknowledge gratefully the financial backing of the reconstruction by the administration of the Free State of Thuringia with an amount of more than 1.2 mill €. The scheduled amount of money was realised according to the financial scheme at any time.

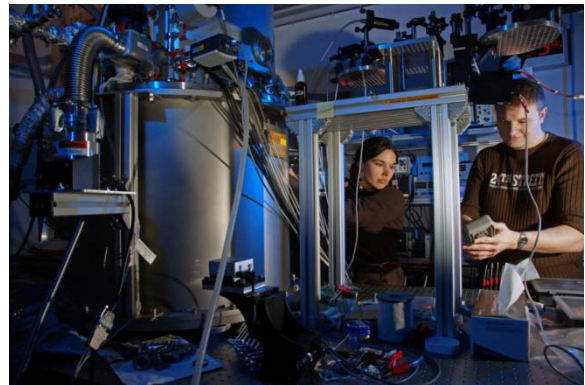


Fig.2: LHe – to be used in the scientific field



Fig.3: New LR70-Liquefier operations

Equipment

Preparation of thin films and devices

- HV evaporation facilities for thermal evaporation and rf-sputtering with oxidation system
- UHV evaporation facilities, including electron gun and in situ RHEED system
- Equipment for laser deposition of thin films and material systems, especially high temperature superconductors (KrF excimer laser, $\lambda = 248$ nm)
- Molecular Beam Epitaxy (MBE) facilities:
- MBE for silicon carbide (RIBER EVA 32 R&D)
- dc and ac sputtering systems for thin films and multilayers
- Ion beam etching with Ar ions at sample temperatures down to 80 K
- Reactive ion beam etching with sample diameters up to 6 cm
- Ultrasonic wire bonder
- Equipment for photolithographic patterning

Surface analysis systems

- AUGER electron spectrometer
- Surface analysis system UNISPEC with XPS, UPS, AES, LEED, STM
- Atomic force microscopes (AFM and Microstructure Measuring Device VERITEKT 3 with needle sensor)
- Surface profilometer DEKTAK 100
- Scanning electron microscopes

Electrical and optical measurement techniques

- Electrical transport measurements (resistance, critical current density, point contact and tunneling spectroscopy)
- Hall-effect and Four-point probe equipment
- Current-voltage characteristics ($2\text{ K} < T < 300\text{ K}$, $B \leq 5\text{ T}$)
- Current-voltage characteristics by microwave irradiation ($2\text{ GHz} < f < 300\text{ GHz}$)
- Noise measurements (frequency range $60\ \mu\text{Hz} - 100\text{ kHz}$) at low temperatures
- LTS-SQUID characterization at 4.2 K (current-voltage, flux-voltage, noise, screening properties)
- HTS-SQUID characterization up to 100 K (current-voltage, flux-voltage, noise)
- 2 Deep level transient fourier spectrometers (temperature range 80 K - 690 K, 30 K - 330 K)
- 3 Admittance spectrometers (frequency range 40 Hz - 100 kHz, 20 Hz - 1 MHz and 75 kHz - 30 MHz, temperature range 30 K - 690 K)
- Optical microscopes
- Optical spectrometers, wavelength region 200 nm to 20 μm
- Low temperature photoluminescence spectroscopy
- Microwave signal generator (frequency range 1 - 20 GHz, resolution: 1 kHz)
- Electrical and optical characterization of high power diode laser arrays

Equipment for thermal treatment

- Furnace for conventional thermal treatment in inert gas atmosphere or vacuum (temperatures up to 2050 K)
- RTA apparatus (double graphite strip heater) for short time annealing

(annealing time in the order of seconds, temperature range 1000 K to 1950 K, temperature rise rate 100 K s^{-1})

Ion beam techniques

3 MV Tandatron accelerator "JULIA", equipped with

- Sputter ion source and Duoplasmatron source
- Universal beam line for ion implantation and ion beam analysis
- Second beam line for ion beam analysis, combined with implantation chamber of 400 kV implanter
- Irradiation chamber with cooled and heated sample holder and four axis goniometer

Applications:

- Ion implantation: energy range 500 keV - 12 MeV, temperature range 15 K - 1500 K
- Ion beam analysis: RBS and PIXE in combination with channeling, ERDA

400 kV implanter "ROMEO", equipped with

- Hot filament, hollow cathode ion source
- Irradiation chamber with cooled and heated sample holder and four axis goniometer, combined with beam line of 3 MV Tandatron accelerator

Applications:

- Ion implantation: energy range 20 keV - 400 keV, temperature range 15 K - 1500 K
- Ion implantation at low temperatures and subsequent RBS analysis using H- or He-ions from 3 MV Tandatron accelerator

Low Energy Implanter "Mr. JIM Stringer", equipped with

- Sputter source, hollow cathode ion source
- Deposition and irradiation with 100 eV – 30 keV ions

Applications:

- Deposition of diamond-like materials
- Surface modification of materials

Low Energy implanter "LEILA", equipped with

- Colutron Ion source 100-Q
- Colutron Ion Gun System G-2-D
- Irradiation chamber with heated sample holder

Application:

- Implantation of Hydrogen: energy range sub-keV, temperature range 300 K - 750 K

Nuclear probe technique

- 2 HP Ge-spectrometers

Low temperature measuring equipment

- He-4 cryostats for temperatures down to 4.2 K
- He-4 refrigerator for the temperature range 1.3 K - 4.2 K
- He-3 cryostat for temperatures down to 300 mK
- He-3/He-4 dilution refrigerator with a base temperature of 35 mK
- He-3/He-4 dilution refrigerator with a base temperature of 7 mK
- Electronic equipment for characterization of cryoelectronic devices
- SQUID sensor systems for magnetic measurements under unshielded conditions

- SQUID sensor system for spatially resolved magnetorelaxometry
- Cryostats ($2\text{ K} < T < 300\text{ K}$; optical window; magnetic field)
- Cryocoolers (Gifford-McMahon and Stirling)
- Pulse tube refrigerators (for sensor cooling)

CIS-LAB

- MBE system NEBULA for Cu(In,Ga)S_2 layers on 4'' substrates including RHEED setup
- Two HV systems for closed-space sublimation (CSS)
- Solar simulator (AM 1.5) with Current-Voltage measurement
- RF reactive sputtering system for transparent conducting oxides (TCO's) and molybdenum
- DC sputtering system for copper and indium
- UHV system ULS400 for Cu(In,Ga)(Se,S)_2 on $(100 \times 100)\text{ mm}^2$ substrates
- Scanning electron microscope JEOL JSM-6490 with LaB_6 -cathode equipped with EDX and CL
- Quantum efficiency measurements of solar cells
- Wet chemical processing and chemical bath deposition of photoactive layers

SQUID application laboratories

- Measurement system for non-destructive evaluation in unshielded environment based on high- T_C -SQUID gradiometers
- Heart monitoring system for biomagnetic investigation in unshielded environment based on high- T_C -SQUID gradiometers
- High precision position detection system based on low- T_C -SQUIDS
- Magnet-Relaxation-Measuring System in unshielded environment based on low- T_C SQUID gradiometers

Clean room (number of particles/cu/t < 100)

- Foto lithography
- Wet chemical etching
- minimum lateral resolution: few micrometers

Shielded rooms

- Faraday room and Magnetic shielded room

Radionuclide laboratory

- for handling of radioactive substances

Laboratory for cryogenic measurement of mechanical quality factors of gravitational wave detector components

- room temperature stability of $\pm 0.2\text{ K}$ at best
- vibration isolation (decoupled foundation)
- acoustic isolation
- remote controlled operation of the measurement equipment
- separated room for disturbing machines (e.g. pumps)
- full supply of technical media to perform cryogenic measurements

4. Current research projects

(A) Supported by the Bundesministerium für Bildung und Forschung (BMBF), Bundesministerium für Wirtschaft und Technologie (BMWi), and Bundesministerium für Umwelt, Naturschutz und Reaktorsicherheit (BMU)

Ioneninduzierte Strukturumbildungs- und Ausheilprozesse in Halbleitern

Teilprojekt 4 im Verbund Hochauflösende in-situ-Charakterisierung der Strukturumbildungsprozesse in Halbleitern

Verbund Forschung mit Sonden und Ionenstrahlen im Gesamtverbund Erforschung der kondensierten Materie mit Großgeräten

Prof. Dr. W. Wesch 05KK7SJ1 07/07 – 12/10

Computational Materials Science gestützte Optimierung des Wirkungsgrades von CIGS-Dünnschichtsolarzellen

Prof. Dr. W. Wesch 0327665E 06/07 – 05/11

CdTe-CdS-Solarzellen hoher Effizienz für eine verbesserte Modul-Produktionstechnologie

Prof. Dr. W. Wesch 0329881A 09/08 – 08/11

Strahlenschädenbildung und Diffusion energetischer Teilchen in SiC

PD Dr. E. Wendler SUA 08/028 04/09 – 12/11

Spitzenforschung und Innovation in den Neuen Ländern – Phona: Photonische Nanomaterialien

Prof. Dr. C. Ronning 03/S210/A 12/09 – 11/14

Forschungsprämie

Prof. Dr. W. Wesch 03FPB00112 09/08 – 08/09

(B) Supported by the Deutsche Forschungsgemeinschaft (DFG)

Strukturierungsverfahren für mikro- und nanooptische Elemente in Lithiumniobat

Dr. E.-B. Kley, Dr. F. Schrepel KL 1199/2-1 05/07 – 04/09

Gas phase studies of astrophysically relevant biomolecules

Prof. Dr. Fr. Huysken HU 474/18-1 01/09 – 12/09

Characterization of structural and optical properties of $Si_{1-x}Ge_x$ nanocrystals produced by laser-induced pyrolysis and by ion implantation

Prof. Dr. Fr. Huysken, Prof. Dr. W. Wesch HU 474/19-1 01/09 – 03/09

Gas-phase synthesis and spectroscopic characterization of astrophysically relevant PAHs

Prof. Dr. Fr. Huysken, Dr. H. Mutschke HU 474/21-1 01/09 – 03/09

Untersuchung astrophysikalischer Reaktionen in flüssigen Helium-Tröpfchen

Prof. Dr. Fr. Huysken HU 474/22-1 01/09 – 03/10

Gütemessungen bei kryogenen Temperaturen
 (Teilprojekt C 4 im SFB/TR 7 „Gravitationswellenastronomie“)
 Prof. Dr. P. Seidel, Dr. W. Vodel, Prof. A. Tünnermann DFG–SFB/TR7 01/03 – 12/10

Ion beam doping of semiconductor nanowires
 Fortsetzung des DFG-Projektes im Rahmen des Schwerpunktprogramms 1165: Nanodrähte
 und Nanoröhren: Von kontrollierter Synthese zur Funktion
 Prof. Dr. C. Ronning Ro1198/7-3 07/06 – 06/10

Rastertunnelspektroskopie an einzelnen Molekülen in epitaktischen Nanoschichten
 Prof. Dr. T. Fritz FR 875/11 10/09 – 12/10

(C) Supported by the Thüringer Ministerium für Bildung, Wissenschaft und Kultur (TKBWK)

Ionenstrahlmodifikation und -analyse von Titanoberflächen
 Prof. Dr. W. Wesch 02/9125 IBA Heiligenstadt 05/02 – 12/10

Dünnschicht Solarzellen der dritten Generation: transparente Dünnschicht Solarzellen/Tandem-Solarzellen
 Prof. Dr. W. Wesch B 514-09001 12/08 – 05/10

Heliumverflüssigungsanlage
 Prof. Dr. P. Seidel TKM 10/07 – 03/09

Ortsaufgelöste Kathodenlumineszenz-Untersuchungen an Halbleitern
 Prof. Dr. C. Ronning B 715-08010 06/08 – 09/09

(D) Supported by other institutions

Experimente zur Labor-Astrophysik
 Prof. Dr. Fr. Huisken MPI Heidelberg 01/02 – 05/12

Luminescent Nano-Objects (NanoLum) (GDRE)
 Prof. Dr. Fr. Huisken European Research Network 01/07 – 06/09

Bio-Imaging with Smart Functional Nanoparticles (BONSAI)
 6th Framework Programme: Specific Targeted Research Projects (STREP)
 Prof. Dr. Fr. Huisken European Commission 01/07 – 02/10

Kryostromkomperator für DESY Hamburg
 Dr. W. Vodel DESY Hamburg 01/01 – 12/09

Zerstörungsfreie Strahldiagnose für Linear- und Ringbeschleuniger
 Dr. W. Vodel GSI Darmstadt 01/07 – 06/10

Physical properties of a system of Josephson junctions
 Prof. Dr. P. Seidel, Dr. Yu. M. Shukrinov Heisenberg-Landau Programm 01/09 – 12/09

<i>Anwendung von höchstempfindlichen LTS SQUIDs zur rückwirkungsfreien absoluten Messung von Strömen im nA-Bereich</i>	Prof. Dr. P. Seidel	GSI Darmstadt	09/09– 12/09
<i>Untersuchungen von CIGS-Photovoltaikzellen, hergestellt im Non-Vakuumverfahren</i>	Prof. Dr. W. Wesch	KF0314502DA6	09/06 – 06/10
<i>Projektbezogener Personenaustausch USA (DAAD)</i>	Prof. Dr. C. Ronning	D/08/11051	01/09 – 12/10
<i>Projektbezogener Personenaustausch Australien (DAAD)</i>	Prof. Dr. W. Wesch	D/07/15034	01/08 – 12/09

5. Publications

5.1 Publications in scientific journals

Z.S. Hussian, E. Wendler, W. Wesch, G.J. Foran, C.S. Schnohr, D.J. Llewellyn, M.C. Ridgway
Rapid ion-implantation amorphization of $In_xGa_{1-x}As$ relative to $InAs$ and $GaAs$
 Physical Review B 79 (2009) 085202

M. Steinert, W. Wesch, A. Undisz, M. Rettenmayr, W.C. Nunes, R.P. Borges, M. Godinko,
 R.M. Rubinger, M.C. Carmo, N.A. Sobolev
Ion beam synthesis of Mn/Sb clusters in silicon
 J. Phys. D: Appl. Phys. 42 (2009) 035406

C. Borschel, C. Ronning, H. Hofsäss, A. Giussani, P. Zaumseil, Ch. Wenger, P. Storck, T.
 Schroeder
Structure and defects of epitaxial $Si(111)$ layers on $Y_2O_3(111)/Si(111)$
 J. Vac. Sci. Technol. B27(1), 2009, 305

M. Hädrich, C. Kraft, C. Löffler, H. Metzner, U. Reislöhner, W. Witthuhn
Pathways to thin absorbers in CdTe solar cells
 Thin Solid Films 517 (2009) 2282-2285

J. Eberhardt, J. Cieslak, H. Metzner, Th. Hahn, R. Goldhahn, F. Hudert, J. Kräußlich,
 U. Kaiser, A. Chuvilin, U. Reislöhner, W. Witthuhn
Epitaxial and polycrystalline $CuInS_2$ layers: Structural metastability and its influence on the photoluminescence
 Thin Solid Films 517 (2009) 2248-2251

T. Voss, G.T. Svacha, E. Mazur, S. Müller, C. Ronning
The influence of local heating by nonlinear pulsed laser excitation on the transmission characteristics of a ZnO nanowire waveguide
 Nanotechnology 20 (2009) 095702

- S. Müller, M. Zhou, Q. Li, C. Ronning
Intra-shell luminescence of transition-metal-implanted zinc oxide nanowires
 Nanotechnology **20** (2009) 135704
- S. Hoffmann, J. Bauer, C. Ronning, Th. Stelzner, J. Michler, C. Ballif, V. Sivakov, S.H. Christiansen
Axial p-n Junctions Realized in Silicon Nanowires by Ion Implantation
 Nano Letters Vol. 9, No. 4, (2009) 1341-1344
- M. Schumm, M. Koerdel, S. Müller, C. Ronning, E. Dynowska, Z. Golacki, W. Szuszkiewicz, J. Geurts
Secondary phase segregation in heavily transition metal implanted ZnO
 Journal of Applied Physics **105** (2009) 083525
- C. Borschel, M. Schnell, C. Ronning, H. Hofsäss
Simulation and fitting of high resolution Rutherford backscattering spectra
 Nucl. Instr. and Methods B 267 (2009) 1737-1739
- H. Zutz, D. Lyzwa, C. Ronning, M. Seibt, H. Hofsäss
Self-organized formation of layered carbon-copper nanocomposite films by ion deposition
 Nucl. Instr. and Methods B 267 (2009) 1356-1359
- K. Zhang, H. Hofsäss, F. Rotter, M. Uhrmacher, C. Ronning, J. Krauser
Morphology of Si surface sputtered-eroded by low-energy Xe-ions at glancing incident angle
 Surface & Coating Technology 203 (2009) 2395-2398
- J. Cieslak, Th. Hahn, J. Kräußlich, H. Metzner, J. Eberhardt, W. Witthuhn
Twinning in Cu(In,Ga)S₂
 Phys. Status Solidi C6, No. 5 (2009) 1023-1026
- W. Wesch, C.S. Schnorr, P. Kluth, Z.S.Hussain, L.L. Araujo, R. Giulian, D.J. Sprouster, A.P. Byrne, M.C. Ridgway
Structural modification of swift heavy ion irradiated amorphous Ge layers
 J. Phys. D: Appl. Phys. 42 (2009) 115402
- W. Wesch, O. Picht, M. Steinert, A. Undisz, M. Rettenmayr, U. Kaiser, J. Biskupek, N.A. Sobolev
Ion beam synthesis of transition metal nanoclusters in Silicon
 AIP Conference Series vol. 1099 (2009) 369
- H. Hartung, R. Geiss, Th. Gischkat, F. Schrempel, R. Iliew, Th. Pertsch, F. Lederer, W. Wesch, E.B. Kley, A. Tünnermann
Photonic crystals in lithium niobate by ion-beam enhanced etching
 IEEE/LEOS Winter Topical Meeting Series (2009) 64
- A. Undisz, F. Schrempel, W. Wesch, M. Rettenmayr
In Situ observation of surface oxide layers on medical grade Ni-Ti alloy during straining
 Journal of Biomedical Materials Research 88A (2009) 1000-1009

- Th. Gischkat, F. Schrempel, Th. Höche, W. Wesch
Annealing behaviour of lithium niobate irradiated with He-ions at 100K
 Nucl. Instr. and Methods B 267 (2009) 1492
- F. Komarov, L. Vlasukova, O. Milchanin, A. Komarov, W. Wesch, A.K. Togambayeva
Effect of implantation and annealing regimes on ion-beam synthesis of InAs nanocrystals
 Lithuanian Journal of Physics, Vol. 49, No. 1, (2009) 105-110
- F. Schrempel, Th. Gischkat, H. Hartung, Th. Höche, E.B. Kley, A. Tünnermann, W. Wesch
Ultrathin membranes in x-cut lithium niobate
 Optics Letters Vol. 34, No. 9 (2009) 1426
- M.A. Zimmler, T. Voss, C. Ronning, F. Capasso
Exciton-related electroluminescence from ZnO nanowire light-emitting diodes
 Applied Physics Letters 94 (2009) 241120
- Th. Gischkat, H. Hartung, F. Schrempel, E.B. Kley, A. Tünnermann, W. Wesch
Patterning of LiNbO₃ by means of ion irradiation using the electronic energy deposition and wet etching
 Microelectronic Engineering 86 (2009) 910-912
- J.-P. Richters, A. Dev, S. Müller, R. Niepelt, C. Borschel, C. Ronning, T. Voss
Influence of metallic coatings on the photoluminescence properties on ZnO nanowires
 Phys. Stat. Solidi RRL 3, No. 5 (2009) 166-168
- E. Wendler, O. Bilani, K. Gärtner, W. Wesch, M. Hayes, F.D. Auret, K. Lorenz, E. Alves
Radiation damage in ZnO ion implanted at 15K
 Nucl. Instr. and Methods B 267 (2009) 2708
- E. Wendler
Mechanisms of damage formation in semiconductors
 Nucl. Instr. and Methods B 267 (2009) 2680
- Z.H. Zhang, Xuefeng Wang, J.B. Xu, S. Muller, C. Ronning, Quan Li
Evidence of intrinsic ferromagnetism in individual dilute magnetic semiconducting nanostructures
 Nature Nanotechnology 4 (2009) 523
- M. Oertel, T. Hahn, H. Metzner, W. Witthuhn
CuInSe₂ solar cells by sequential absorber layer processing
 Phys. Status Solidi C6 No. 5, (2009) 1253-1256
- M. Hädrich, C. Kraft, H. Metzner, U. Reislöhner, C. Löffler, W. Witthuhn
Formation of CdS_xTe_{1-x} at the p-n junction of CdS-CdTe solar cells
 Phys. Status Solidi C6 No. 5, (2009) 1257-1260
- C. Borschel, R. Niepelt, S. Geburt, C. Gutsche, I. Regolin, W. Prost, F.-J. Tegude, D. Stichtenoth, D. Schwen, C. Ronning
Alignment of semiconductor nanowires using ion beams
 Small 2009, 5, No. 22, 2576-2580

- A. Schüller, M. Busch, J. Seifert, S. Wethekam, H. Winter, K. Gärtner
Superstructures of oxygen and sulphur on a Fe(110) surface via fast atom diffraction
Physical Review B 79, (2009) 235425
- M. Hayes, A. Schroeter, E. Wendler, W. Wesch, F.D. Auret, J.M. Nel
Damage formation in Ge during Ar⁺ and He⁺ implantation at 15 K
Physica B-Condensed Matter 404 (2009) 4382.
- M. Katsikini, F. Pinakidou, E.C. Paloura, E. Wendler, W. Wesch, R. Manzke
N-K edge NEXAFS study of the defects induced by indium implantation in GaN
J. Phys.: Conf. Series 190 (2009) 012065
- J. Pezoldt, T. Kups, T. Stauden, B. Schröter
Polarity determination and control of SiC grown on Si
Material Science and Engineering B **165** (2009) 28-33
- A. Grib, P. Seidel
Wide-band phase locking of Josephson junctions in a resonator
Phys. Status Solidi RRL **3**, (2009), 302-304
- I.W. Martin, E.Chalkley, R. Nawrodt, H. Armandula, R. Bassiri, C. Comtet, M.M. Fejer, A. Gretarsson, G. Harry, D. Heinert, J. Hough, I. MacLaren, C. Michel, J.-L. Montorio, N. Morgado, S. Penn, S. Reid, R. Route, S. Rowan, C.Schwarz, P. Seidel, W. Vodel, A.L. Woodcraft
Comparison of the temperature dependence of the mechanical dissipation in thin film of Ta₂O₅ and Ta₂O₅ doped with TiO₂
Class. Quantum Grav. **26**, (2009), 155012 (11pp.)
- A. Steppke, R. Geithner, S. Hechler, R. Nawrodt, R. Neubert, W. Vodel, M. Schwickert, H. Reeg, P. Seidel
Application of LTS-SQUIDS in Nuclear Measurement Techniques
IEEE Trans. Appl. Supercond. **19**, (2009), 768-771
- P. Seidel, C. Becker, A. Steppke, U. Schinkel, K. Hofer, V. Grosse, S. Engmann, F. Schmidl, L. Redlich
Higher Order HTSC Gradiometer for Measurements in Unshielded Environment
IEEE Trans. Appl. Supercond. **19**, (2009), 218-221
- P. Seidel
Leben und Werk von Leonhard Sohncke (1842-1897), einem Mitbegründer des Oberrheinischen Geologischen Vereins
Jber. Mitt. oberrhein. geol. Ver., N.F. **91**, (2009), 101-112
- P. Seidel, C. Becker, K. Hofer, U. Schinkel, R. Hähle, A. Steppke
Study of a four Josephson junction system made of high temperature superconductor on a bi-crystal
Ext. Abstr. ISEC'09, June 16-19, Fukuoka, Japan, SQ-P31 (2 pp).
- Yu. M. Shukrinov, A. Irie, G.-I. Oya, M. Suzuki, N. F. Pedersen, P. Seidel
Return current in current-voltage characteristics of intrinsic Josephson junctions
Ext. Abstr. ISEC'09, June 16-19, Fukuoka, Japan, TD-02 (2 pp).

- T. Koettig, F. Richter, C. Schwarz, R. Nawrodt, M. Thürk, P. Seidel
Cold-Head Vibrations of a Coaxial Pulse Tube Refrigerator
Cryocoolers **15**, (2009), 687-693
- C. Schwarz, R. Nawrodt, D. Heinert, M. Thürk, W. Vodel, A. Tünnermann, P. Seidel
Cryogenic setup for Q-factor measurements on bulk materials for future gravitational wave detectors
Proceedings of ICEC 22-ICMC 2008, edited by Ho-Myung Chang et al., The Korean Institute of Applied Superconductivity and Cryogenics, (2009), 519-524
- F. Huisken, C. Jäger, H. Mutschke, Th. Henning
Gas-phase condensation of nanometer- and subnanometer-sized carbon grains and polycyclic aromatic hydrocarbons
Diamond and Related Materials **18**, 392-395 (2009)
- C. Jäger, F. Huisken, H. Mutschke, I. Llamas-Jansa, Th. Henning
Formation of PAHs and carbonaceous solids in gas-phase condensation experiments
Astrophys. J. **696**, 706-712 (2009)
- G. Rouillé, M. Arold, A. Staicu, Th. Henning, and F. Huisken
Cavity ring-down laser absorption spectroscopy of jet-cooled L-tryptophan
J. Phys. Chem. A **113**, 8187-8194 (2009)
- A. C. Brieva, C. Jäger, F. Huisken, L. Šiller, Y. V. Butenko
A sensible route to covalent functionalization of carbon nanoparticles with aromatic compounds
Carbon **47**, 2812-2820 (2009)
- F. Voigt, G. Bauer, F. Huisken
Layer growth and connectivity calculations based on a stick-ball model: Application to silicon nanocrystals
J. Appl. Phys. **106**, 034308 (2009)
- A.M. Chizhik, A.I. Chizhik, R. Gutbrod, A.J. Meixner, T. Schmidt, J. Sommerfeld, F. Huisken
Imaging and spectroscopy of defect luminescence and electron-phonon coupling in single SiO₂ nanoparticles
Nano Letters **9**, 3239–3244 (2009)
- L. B. Ma, T. Schmidt, O. Guillois, F. Huisken
Evolution of photoluminescence properties of Si_xGe_{1-x} nanocrystals synthesized by laser-induced pyrolysis
Appl. Phys. Lett. **95**, 013115-1-3 (2009)
- G. Rouillé, M. Steglich, F. Huisken, Th. Henning, K. Müllen
UV/Vis spectroscopy of matrix-isolated hexa-peri-hexabenzocoronene: Interacting electronic states and astrophysical context
J. Chem. Phys. **131**, 204311-1-7 (2009)

F. Huisken, G. Rouillé, M. Arold, A. Staicu, Th. Henning
Electronic Spectroscopy of Biological Molecules in Supersonic Jets: The Amino Acid Tryptophan

In: *Rarified Gas Dynamics, 26th International Symposium on Rarefied Gas Dynamics, RGD26*, edited by T. Abe, AIP Conference Proceedings Vol. 1084, American Institute of Physics (2009) pp. 539-544

A. M. Chizhik, T. Schmidt, A. I. Chizhik, F. Huisken, A. Meixner
Confocal microscopy and spectroscopy of defect photoluminescence in single SiO₂ nanoparticles

In: *Nanophotonic Materials VI*, edited by **S. Cabrini and T. Mokari**, Proc. SPIE **7393**, 739305 (2009)

C. Jäger, H. Mutschke, Th. Henning, F. Huisken

Analogs of cosmic dust

in: *Cosmic Dust – Near and Far*, ed. by Th. Henning, E. Grün, and J. Steinacker, Astronomical Society of the Pacific Conference Series, Vol. CS 414, in press (2009)

5.2 Invited talks and colloquia

C. Ronning

Halbleiternanodrähte: Eigenschaften und Dotierung

TU Ilmenau, Kolloquium Werkstofftechnik, 15.01.2009

C. Ronning

Ionenimplantation in ZnO: Volumenkristalle und Nanodrähte

Helmholtz Zentrum Berlin, Photovoltaik Seminar Adlershof, 26.02.2009

C. Ronning

Halbleiternanodrähte: Eigenschaften und Dotierung

Fraunhofer Institut IST Braunschweig, Seminar Oberflächentechnik, 17.03.2009

F. Huisken

Staub und Moleküle im All: Laborexperimente zu astrophysikalischen Fragestellungen

Photonik-Kolloquium, Math.-Nat. Fakultät, Universität Potsdam, 05.05.2009

C. Jäger

Cosmic dust analogs from the laboratory

Seminarvortrag am Max-Planck-Institut für Chemie, Mainz, 27.05.2009

C. Ronning

Ion beam doping of semiconductor nanowires

IOM Leipzig, Institutsseminar, 28.05.2009

C. Ronning

Halbleiternanodrähte: Eigenschaften und Dotierung

TU Chemnitz, Kolloquium der Fakultät Physik, 03.06.2009

C. Ronning

Ion beam doping of semiconductor nanowires

iThemba Labs, Cape Town, Seminar of Ion beam Facility, 25.09.2009

F. Huisken

Photoluminescence properties of size-selected and individual silicon quantum dots

European Silicon Days, Vienna, Austria, September 20 – 22, 2009

Thomas Bierschenk

Temperature dependence of damage formation in Ag ion irradiated 4H-SiC

Physics Colloquium, University of Pretoria, October 8, 2009

F. Huisken

Leuchteigenschaften von gröÙenselektierten und individuellen Silicium- und Germanium-Quantenpunkten

Clustertreffen, Herzogenhorn, 04. – 09.10.2009

W. Vodel

SQUID - an extreme sensitive sensor with a wide range of applications in natural science

6th German-Vietnamese Summer School on Modern Topics in Natural Sciences - Environmental Research and Technology, Ho Chi Minh City Vietnam, September 17-18, 2009

W. Vodel

The SQUID based Cryogenic Current Comparator - an useful tool for beam diagnostics

Internat. Workshop on Low Current, Low Energy Beam Diagnostics, Hirschberg-GroÙsachsen, 23.-25.11.2009

5.3 Conference and workshop contributions

Nanowire Symposium am IPHT Jena, Germany, January 13, 2009

R. Niepelt

Alternative contacting methods for nanowires

C. Borschel

Ion Beam Induced Alignment of Semiconductor Nanowires

S. Geburt

Rare earth doping of ZnO nanowires

17. Jahrestagung der Deutschen Gesellschaft für Kristallographie, Hannover, Germany, March 09 – 12, 2009

L. Kienle, V. Duppel, R. Adelung, E. Quandt, S. Müller, C. Ronning, A. Simon

Verzwilligung und Verwachsung in ZnO Nanostrukturen, Twinning and Intergrowth in ZnO nanostructures

Frühjahrstagung der DPG, Dresden, Germany, March 23 – 27, 2009

F. Szillat, H. Kleemann, P. Zeigermann, M. Steglich, M. Blech, B. Schröter
Growth of horizontally aligned carbon nanotubes on single crystalline surfaces

M. Bohrisch, P. Zeigermann, H. Kleemann, B. Schröter
Mechanical and electrical characterization of individual single-walled carbon nanotubes by scanning probe microscopy

M. Trautmann, R. Hähle, J. Fischer, I. Sill, A. Bikowski, T. Schmidt, V. Grosse, F. Schmidl, P. Seidel
Klusterexperimente an dünnen Co-PLD-Schichten und Schichtsystemen

M. Teichmann, M. Pollithy, K. Höfer, S. Engmann, U. Schinkel, R. Hähle, V. Große, C. Becker, F. Schmidl, P. Seidel
Superconducting properties of YBCO thin film structures with gold nanoclusters

M. Pollithy, K. Höfer¹, U. Schinkel, P. Michalowski, V. Grosse, F. Schmidl, P. Seidel, D. Meier, T. Shapoval
Investigation of superconducting thin film structures prepared by nanoscale wedge polishing

S. Engmann, V. Grosse, R. Hähle, J. Fischer, P. Seidel
Strain and electric field effects on the dielectric permittivity of epitaxial SrTiO₃ thin films

U. Schinkel, C. Becker, A. Steppke, K. Höfer, M. Pollithy, V. Grosse, S. Engmann, F. Schmidl, P. Seidel
Two dimensional planar SQUID-Gradiometer on a SrTiO₃- bicrystal

C. Pansow, V. Grosse, A. Steppke, F. Schmidl, P. Seidel
Superconducting Properties of Niobium Thin Films grown by Pulsed Laser Deposition

D. Heinert, A. Gryb, C. Schwarz, S. Kroker, R. Nawrodt, W. Vodel, A. Tünnermann, S. Rowan, J. Hough, P. Seidel
Investigation of the loss mechanisms in crystalline solids at low temperatures for future gravitational wave detectors

C. Schwarz, S. Kroker, R. Nawrodt, D. Heinert, S. Reid, I. Martin, E. Chalkley, R. Neubert, W. Vodel, A. Tünnermann, S. Rowan, J. Hough, P. Seidel
Experimental setup for investigation of mechanical losses of thin dielectric films at low temperatures

C. Borschel, M. Schnell, C. Ronning, H. Hofsäss
A Computer Program for the Analysis of High Resolution RBS Spectra

C. Borschel, R. Niepelt, S. Geburt, I. Regolin, C. Gutsche, W. Prost, F.J. Tegude, D. Stichtenoth, D. Schwen, C. Ronning
Ion Beam Induced Alignment of Semiconductor Nanowires

H. Zutz, D. Lyzwa, C. Ronning, M. Seibt, and H. Hofsäss
Self-organization in metal containing amorphous carbon Nanocomposites

M.A. Zimmerler, J. Bao, K.A. Sunter, F. Capasso, S. Müller, C. Ronning
Laser oscillations thresholds in ZnO nanowires

Th. Gischkat, F. Schrempel, H. Hartung, E.-B. Kley, A. Tünnermann, W. Wesch
Micro- and nano-patterning of lithium niobate

T. Steinbach, F. Schrempel, Th. Gischkat, W. Wesch
Channelling irradiation of LiNbO₃: Influence of ion energy and ion species

W. Wesch, C.S. Schnohr, P. Kluth, Zohair S. Hussain, L.L. Araujo, R. Giulian, D.J. Sprouster, A.P. Byrne, M.C. Ridgway
Structural modification of swift heavy ion irradiated amorphous Ge layers

SPP 1165 Doktorandentreffen, Berlin, Germany, February 18, 2009

S. Geburt
Ion beam induced alignment of semiconductor nanowires

ET WP2 MEETING Roma, Italy, February 25 – 28, 2009

Ch. Schwarz, S. Kroker, D. Heinert¹, R. Nawrodt, A. Tünnermann, P. Seidel
Current status of the bulk and coating research in Jena

SFB-Halbjahrestreffen, Frühjahr 2009, Jena, Germany, March 17, 2009

D. Heinert, C. Schwarz, S. Kroker, R. Nawrodt, A. Grib, W. Vodel, A. Tuennermann
and P. Seidel
Current status of the loss measurement and loss analysis

Ion Beam Workshop, Jena, Germany, April 06 – 08, 2009

C. Borschel, R. Niepelt, S. Geburt, I. Regolin, C. Gutsche, W. Prost, F.J. Tegude,
D. Stichtenoth, D. Schwen, C. Ronning
Ion Beam Induced Alignment of Semiconductor Nanowires

Konrad Gärtner, Werner Wesch
MD-Simulationen zur Schädigung von AlxGal-xAs durch Ionenbestrahlung

Tobias Steinbach, Frank Schrempel, Werner Wesch
Channeling irradiation of LiNbO₃

MRS spring meeting, San Francisco, USA, April 13 – 17, 2009

H. Zutz, D. Lyzwa, C. Ronning, M. Seibt, H. Hofsäss
Self-organization of Multilayer Structures in Metal Containing Amorphous Carbon Nanocomposites

S. Hoffmann, V. Sivakov, C. Ronning, Ch. Niederberger, J. Michler, S.H. Christiansen
Axial p-n junctions in silicon nanowires by ion implantation

IAEA Topical Meeting on Nuclear Research Applications and Utilization of Accelerators, Vienna, Austria, May 04 – 08, 2009

K. Bharuth-Ram, T.B. Doyle, H. Hofsäss, S. Müller and C. Ronning
Search for the formation of magnetic nanoclusters by ion implantation into suitable insulators

Gravitational Wave Advanced Detector Workshop – Fort Lauderdale/Florida, USA, May 08 – 19, 2009,

Ch. Schwarz, R. Nawrodt, S. Kroker, D. Heinert, S. Reid, I. Martin, E. Chalkley, R. Neubert, W. Vodel, A. Tünnermann, S. Rowan, J. Hough, P. Seidel
Mechanical loss measurements at low temperatures of coating and bulk materials

E-MRS Spring meeting, Strassburg, France, June 08 – 12, 2009

C. Baristiran-Kaynak, M. Lukosius, I. Costina, C. Wenger, C. Borschel, C. Ronning
Characterization of Sr-Ta-O films based on spectroscopic techniques

3. Jahrestreffen des DFG Schwerpunktprogramms 1165 "Nanodrähte und Nanoröhren: von kontrollierter Synthese zur Funktion", Fulda, Germany, June 24 – 26, 2009

R. Niepelt, C. Borschel, S. Geburt, C. Ronning
Ion beam doping of semiconductor nanowires

SPIE conference on Nanophotonic Materials VI, San Diego, California, USA, August 02 - 06, 2009

A. M. Chizhik, T. Schmidt, A. I. Chizhik, F. Huisken, A. Meixner
Confocal microscopy and spectroscopy of defect photoluminescence in single SiO₂ nanoparticles

**Internat. Summerschool: Nanoscaled Oxides - Big Opportunities in Small Structures
WE Heraeus Physics School Bad Honnef, Germany, August 02 – 07, 2009**

R. Niepelt, M. Fravventura, C. Ronning
Surface evolution of metal oxides induced by medium energy sputtering

S. Geburt
Cathodoluminescence of single doped ZnO nanowires

**XVIII International Materials Research Congress, Cancun, Mexico, August 16 – 21,
2009**

C. Borschel, R. Niepelt, S. Geburt, C. Gutsche, I. Regolin, W. Prost, F.-J. Tegude, D. Stichtenoth, D. Schwen, and C. Ronning,
Ion Beam Induced Alignment of Semiconductor Nanowires

**14th International Conference on II-VI compounds, St. Petersburg, Russia, August 23 to
28, 2009**

M. Schumm, M. Koerdel, C. Ziereis, J. Geurts, S. Müller, C. Ronning, E. Dynowska, Z. Gołacki, W. Szuszkiewicz
Annealing effects and generation of secondary phases in ZnO after high-dose transition metal implantation

**15th International Conference on Radiation Effects in Insulators (REI-15), Padova, Italy,
August 30 – September 04, 2009**

Th. Gischkat, P. Queitzsch, F. Schrepel, W. Wesch
Comparative study of damage formation in LiNbO₃ due to the nuclear and electronic energy loss

E. Friedland, Nic van der Berg, J. Malherbe, E. Wendler, W. Wesch
Diffusion of silver and iodine implants in silicon carbide

E. Wendler, Th. Bierschenk, W. Wesch, E. Friedland, J. Malherbe
Temperature dependence of damage formation in Ag ion irradiated 6H-SiC

ET WP2 Meeting Genoa, Italy, September, 14 – 16, 2009

Ch. Schwarz, S. Kroker, D. Heinert, A. Tünnermann, P. Seidel
Investigation of mechanical losses of 3rd generation gravitational wave detector materials

24. European Photovoltaic Solar Energy Conference and Exhibition, Hamburg, Germany, September 21 – 25, 2009

M. Blech, A. Laades, C. Ronning, B. Schröter, C. Borschel, D. Rzesanke, A. Lawrenz
Detailed study of PECVD silicon nitride and correlation of various characterization techniques

DFG-NSF Research Conference: Sustainable Use of Nanomaterials for Novel Engineering Solutions”, New York City, USA, October 14 – 17, 2009

C. Borschel, R. Niepelt, S. Geburt, C. Ronning, M.A. Zimmler, K.A. Sunter, F. Capasso
Doping of semiconductor nanowires for electronic and photonic devices

Clustertreffen, Herzogenhorn, Germany, Oktober 04 – 09, 2009

T. Schmidt, F. Huisken, A. M. Chizhik, A. I. Chizhik, A. Meixner
Confocal photoluminescence studies on single Si and SiO₂ nanoparticles

K. Potrick, L. B. Ma, T. Schmidt, O. Guillois, F. Huisken
Synthesis and characterization of light-emitting Si/Ge clusters

S. Krasnokutski and F. Huisken
Chemical reactions inside He droplets

Nanowire Growth Workshop, Paris, France, Oktober 26 – 27, 2009

S. Geburt, C. Borschel, M. Kozlik, A. McDonnell, K. Sunter, F. Capasso, C. Ronning
Growth and characterization of Lasing of cadmium sulfide nanostructures

International Conference on one-dimensional Nanomaterials (ICON3), Atlanta, USA, December 07 – 09, 2009

M.A. Zimmler, K.A. Sunter, J. Bao, S. Müller, C. Ronning, F. Capasso
Laser oscillations in ZnO nanowires

5.4 Theses

Diploma and Master Theses

Michael Kozlik *Synthese von Halbleiternanodrähten für die Photonik*

Christoph Heisler *Herstellung und Untersuchung dünner CdTe-Solarzellen*

Johannes Wagner *Influence of the n-hetero contact layer on the electro-optical properties of CIGS thin-film solar cells*

Stefan Götz	<i>Cu(In,Ga)Se₂-Solarzellen: flexible Substrate und Kontaktwiderstände</i>
Christian Wolf	<i>Herstellung von CuInSe₂-Solarzellen mit einem Zwei-Stufen-Prozess</i>
Maria Concetta Fravventura	<i>Ion-beam induced nanoscale ripples on Si, TiO₂ and Ti surfaces</i>
Gabriele Bulgarini	<i>Luminescence of single ZnS nanowires implanted with Mn and rare earths</i>
Peter Kossebau	<i>Herstellung und Charakterisierung von Bauelementen auf Basis von Kohlenstoff-Nanoröhren</i>
Uwe Schinkel	<i>Herstellung und Charakterisierung planarer HTSL-DC-SQUID Gradiometer 2. Ordnung</i>
Pascal Macha	<i>Hochfrequentes Auslesen von Flussqubits</i>
Robert Hähle	<i>Untersuchungen zur Abhängigkeit der elektrischen Eigenschaften dünner SrTiO₃ Schichten vom Kontaktmaterial</i>
Michael Schneider	<i>Untersuchungen zur physikalischen Analyse geomagnetischer SQUID-Signale</i>
Stefanie Kroker	<i>Charakterisierung mechanischer Verluste dielektrischer Schichten bei kryogenen Temperaturen</i>
Andreas Siebert	<i>Optimierung der Abscheideprozesse bei der Pulsed Laser Deposition von oxidischen Schichten und Schichtsystemen (FH)</i>
Sebastian Wolf	<i>Demonstrationsmodelle zu Problemen des experimentellen Nachweises von Gravitationswellen (Staatsexamen)</i>
Tolou Sabri	<i>Photoluminescence properties of silicon-based oxide nanoparticles upon thermal annealing</i>
Mario Gerhard	<i>Texturierte Substrate für LLC-Si-Dünnschichtsolarzellen (IPHT)</i>
Christian Lehmann	<i>Optimierung von laserkristallisierten Dünnschichtsolarzellen auf Siliziumbasis (IPHT)</i>
Peter Queitzsch	<i>Defektbildung durch elektronische und nukleare Energiedeposition auf die Formierung von defekten in Lithiumniobat</i>
Henrik Grundmann	<i>Klassische und quantenmechanische Regenbögen bei der streifenden Streuung schneller Atome und Moleküle an der sauberen und sauerstoffbedeckten Ni(110)-Oberfläche (Humboldt-Universität Berlin)</i>

Christoph Lösche *Numerische Berechnung von Kristallisationsprozessen in Silizium (IPHT)*

Florian Szillat *Orientiertes Wachstum von Kohlenstoffnanoröhren mittels chemischer Gasphasenabscheidung*

Studies and Bachelor Thesis

Aaron Reupert *Spannungsaufbau in Germanium durch Ionenbestrahlung*

Martin Steglich *Untersuchung zur Defektformierung in Germanium unter Ionenbestrahlung bei Raumtemperatur*

Jura Rensberg *Untersuchungen zur Schädigung von LiNbO_3 durch energiereiche Sauerstoffionen*

Anne Nathanael *Synthese von Mangansulfid-Nanostrukturen*

Julian Kühnel *Growth and Characterization of metallic nanoparticles on solid surfaces*

Amanda McDonnell *Synthesis and Characterisation of CdS nanowires*

Sven Schönherr *Untersuchungen von CNTs – elektrische Messung, Herstellung und Messung von „Dummies“*

Marc Teichmann *Herstellung und Untersuchungen von Au - Klustern auf YBCO-Schichten*

Markus Schiffler *Elektrische Untersuchungen an STO – Tunnelnichten*

PhD-Theses

Sven Müller *Structural and optical impact of transition metal implantation into zinc oxide single crystals and nanowires (extern Universität Göttingen)*

Mathias Hädrich *Materialwissenschaftliche Untersuchungen an CdTe-CdS-Heterosolarzellen*

Marco Arold *UV-Absorptionsspektroskopie astrophysikalisch relevanter Moleküle im Düsenstrahl*

Habilitation

Dr. Joachim Albrecht *Grenzflächenkontrollierte Eigenschaften dünner Supraleiterfilme*

6. Cooperations, guests and colloquia at IFK

The Institute of Solid State Physics collaborates with a large number of Institutes and Universities in Germany and around the world and has also close connections with several companies. In the framework of these wide spread contacts in 2009 a number of scientists from various countries visited our Institute to perform experiments, discuss scientific results obtained within joint projects and to give talks in the colloquium of the Institute of Solid State Physics.

6.1 Visiting scientists

Dr. L.L. Araujo	Australian National University, Canberra, Australien
Gabriele Bulgarini	Politecnico di Milano, Italien
Dr. Janyce Franc	LMA Lyon, Frankreich
Maria Concetta Fravventura	Politecnico di Milano, Italien
Prof. Dr. E. Friedland	University of Pretoria, Pretoria, Süd-Afrika
Dr. R. Giulian	Australian National University, Canberra, Australien
Dr. Alexander Grib	Kharkov National University, Physics Department, Ukraine
Dr. Olivier Guillois	CEA Saclay, Paris, France
Prof. Dr. R. Gupta	University of Calcutta, Indien
R. Joseph Kuhudzai	University of Pretoria, Pretoria, Süd-Afrika
Prof. Dr. J. G. Lu	University of Southern California, Los Angeles, USA
Prof. Dr. Johan Malherbe	University of Pretoria, Pretoria, Süd-Afrika
Dr. Iain Martin	Universität Glasgow, UK
Amanda McDonnell	University of Leeds, UK
Prof. Dr. E. McGlynn	Dublin City University, Irland
Dr. Ronny Nawrodt	Universität Glasgow, UK
Dr. Yury Shukrinov	Bogoliubov Laboratory of Theoretical Physics, Joint Institute for Nuclear Research Dubna, Russland
Prof. Dr. N.A. Sobolev	Universität Aveiro, Aveiro, Portugal
D. Sprouster	Australian National University, Canberra, Australien
Dr. Angela Staicu	National Institute for Laser, Plasma and Radiation Physics, Bukarest, Romania
Kristen Sunter	Harvard University, Boston, USA

6.2 Colloquia at the Institute of Solid State Physics

Dr. Enrico Trave (Università di Venezia "Cà Foscari"), 16.01.2009
Erbium-doped glasses for optical amplification: Enhancement of erbium fluorescence through the interaction with metal and silicon nanostructures

Dr. Werner Prost (Universität Duisburg-Essen), 30.01.2009
III/V-Nanodrähte für die Nanoelektronik und die Licht/Strom-Wandlung

Prof. Dr. Wolfram Heimbrod (Universität Marburg), 13.02.2009
Metastabile, verdünnte III-V-Nitrid Halbleitersysteme - interessante Physik und vielversprechendes Anwendungspotenzial

Prof. Dr. P. Schaaf (Technische Universität Ilmenau), 17.04.2009
Micro- and Nanostructured Thin Films and Coatings for challenging applications

Dr. W. Vodel (Institut für Festkörperphysik, Jena), 16.05.2009
Anwendungen von LTS SQUIDs in der Präzisionsmesstechnik

Dr. Kevin Lauer (Solarzentrum Erfurt), 15.05.2009
Ladungsträgerlebensdauer in kristallinem Silizium für Solarzellen

Dr. Andreas Wolf (MPI Heidelberg), 29.05.2009
Kalte Chemie mit schnellen Ionenstrahlen

Prof. Dr. R. Adelung (Universität Kiel), 12.06.2009
Integration of self organized nanostructures into devices

Prof. Dr. Paul Müller (Universität Nürnberg-Erlangen), 10.07.2009
C-Achsen-Transport von Pniktid-Supraleitern

Prof. Dr. Enda McGlynn (Dublin City University, Ireland), 21.07.2009
ZnO Nanostructures: Synthesis, Characterization and Possible Uses

Dr. Claudia Schnohr (Institut für Festkörperphysik, Jena), 30.10.2009
Anisotropie atomarer Schwingungen in kristallinem InP

Prof. Dr. Torsten Fritz (Institut für Festkörperphysik, Jena), 13.11.2009
Organische Halbleiterschichten: Struktur und physikalische Eigenschaften

Prof. Dr. Jia Grace Lu (University of Southern California, Los Angeles), 27.11.2009
Charge transport in ZnO-based nanowires

Prof. Dr. Norbert Nickel (Helmholtz-Zentrum Berlin), 11.12.2009
Road to p-type ZnO – why nitrogen doping is difficult

7. Teaching activities

7.1 Lectures

Physik der Materie I	Prof. Dr. W. Wesch
Physik der Materie II	Prof. Dr. C. Ronning
Nukleare Festkörperphysik	Prof. Dr. C. Ronning
Physik für Nebenfach-Studenten (Biologie, Ernährungswissenschaften, Pharmazie, Biogeowissenschaften, Chemie, Biochemie)	Prof. Dr. W. Wesch
Experimentalphysik für Mediziner, Zahnmediziner	PD Dr. F. Schmidl
Festkörperphysik	Prof. Dr. P. Seidel
Ergänzende Kapitel der Festkörperphysik	Prof. Dr. P. Seidel PD Dr. F. Schmidl
Ergänzende Kapitel der Festkörperphysik Materialwissenschaftler 5. Semester	Prof. Dr. P. Seidel
Elektronik	PD Dr. F. Schmidl, Dr. W. Vodel, Dr. R. Nawrodt
Experimentalphysik IV: Struktur der Materie 2 (Physik-Diplom, Physik-Lehramt)	Prof. Dr. P. Seidel
Experimentalphysik für Biochemiker II	PD Dr. F. Schmidl
Optoelektronik	PD Dr. F. Schmidl
Master of Photonics 3. Semester	
Supraleitung	Prof. Dr. P. Seidel, Dr. J. Albrecht, (MPI Stuttgart)
Festkörperanalyse mit energiereichen Teilchen	Dr. F. Schrepel
Cluster und Nanoteilchen I + II	Prof. Dr. F. Huisken
Kernphysik für Lehramt	Prof. Dr. C. Ronning
Photovoltaik I + II	PD Dr. H. Metzner

7.2 Seminars

Kernphysik für Lehramt	Prof. Dr. C. Ronning, Dipl.-Phys. R. Niepelt
Physik für Biogeowissenschaftler	PD Dr. E. Wendler
Experimentalphysik II für Physiker	PD Dr. E. Wendler
Physik der Materie I	PD Dr. E. Wendler, PD Dr. K. Gärtner

Kerne und Elementarteilchen	PD Dr. K. Gärtner
Nukleare Festkörperphysik	Prof. Dr. C. Ronning, Dipl.-Phys. R. Niepelt
Elektronik (Physik-Diplom und Informatik)	Dr. W. Vodel, PD Dr. F. Schmidl, Dr. R. Nawrodt, Dipl.-Phys. D. Heinert
Elektronik (Lehramtsstudenten)	Dr. W. Vodel, Dr. R. Nawrodt
Elektronikpraktikum Lehramtskandidaten 5. Semester Physik-Bachelor, Nebenfächler Einführung in die Festkörperphysik	Dr. W. Vodel Dipl.-Phys. R. Neubert
Tiefemperaturphysik und Supraleitung	PD Dr. F. Schmidl D. Heinert
Ergänzende Kapitel der Festkörperphysik Materialwissenschaftler 5. Semester	Prof. Dr. P. Seidel, PD Dr. F. Schmidl
Grundkurs Physik der Materie II	PD Dr. F. Schmidl, Dipl.-Ing. M. Büttner
Proseminar zum Fortgeschrittenenpraktikum WS 2008/2009, SoSe 2009 Institutsseminar	Prof. Dr. C. Ronning, Dipl.-Phys. C. Borschel
Festkörperphysik	Dr. B. Schröter
Oberseminar Festkörperphysik/ Materialwissenschaften	Prof. Dr. P. Seidel, Prof. Dr. C. Ronning
	Prof. Dr. C. Ronning
	Prof. Dr. P. Seidel
7.3 Practica	
Physikalisches Praktikum für Biologen	Prof. Dr. W. Wesch (Leitung)
Fortgeschrittenen-Praktikum	Dr. B. Schröter (Leitung) Dipl.-Phys. R. Nawrodt Dipl.-Ing. M. Thürk Dipl.-Phys. Ch. Schwarz
F-Praktikum (Kernphysik)	Dr. U. Reislöhner, Dr. F. Schrempel, J. Haarstrich, Dipl.-Phys. S. Geburt
Grundpraktikum	Prof. Dr. W. Wesch, Dipl.-Phys. J. Sommerfeld, Dipl.-Phys. M. Oertel, Dipl.-Phys. C. Kraft
Messtechnik	PD Dr. F. Schmidl, Dipl.-Ing. H. Mühlig, Dipl.-Phys. V. Große, Dipl.-Phys. Ch. Becker, Dipl.-Phys. R. Geithner
Tutorium Messtechnik	PD Dr. F. Schmidl

Elektronik

PD Dr. F. Schmidl(Leitung),
Dr. W. Vodel (to 05/09)
Dipl.-Ing. R. Neubert
Dipl.-Ing. H. Mühlig

8. Personnel

Professors

Prof. Dr. habil. Carsten Ronning (director since 10/09)
Prof. Dr. habil. Torsten Fritz
Prof. Dr. habil. Paul Seidel (director to 09/09)
Prof. Dr. habil. Werner Wesch
Prof. Dr. habil. Friedrich Huisken

Scientific Staff

PD Dr. habil. Konrad Gärtner	Dr. Libo Ma (to 03/09)
PD Dr. habil. Heinrich Metzner	Dr. Ronny Nawrodt
PD Dr. habil. Frank Schmidl	Dr. Sandor Nietzsche
PD Dr. habil. Elke Wendler	Dr. Udo Reislöhner
Dr. Janko Cieslak	Dr. Gaël Rouillé (to 01/09)
Dr. Ernst Glaser	Dr. Frank Schrempel (to 04/09)
Dr. Cornelia Jäger	Dr. Bernd Schröter
Dr. Sergiy Krasnokutskiy	Dr. Wolfgang Vodel

PhD Students

Marco Arold	Christian Kraft
Christoph Becker (to 04/09)	Raphael Niepelt
Christian Borschel	Michael Oertel
Markus Büttner	Jakob Haarstrich
Sebastian Geburt	Torsten Schmidt
Rene Geithner	Christian Schwarz
Thomas Gischkat	Jana Sommerfeld
Veit Große	Tobias Steinbach
Mathias Hädrich	Mathias Steglich
Daniel Heinert	

Extern

Boris Ivanov	(IPHT Jena, Förderung DAAD)
Sascha Glathe	(IPHT Jena)
Thomas Schönau	(IPHT Jena)
Gregor Oelsner	(IPHT Jena)

Diploma Students

Thomas Bierschenk
Martin Bohrisch
Anika Brömel
Björn Burkhardt (IPHT, extern)
Sebastian Döring
Janine Fischer
Martin Gnauck
Stefan Goetz
Christoph Heilmann
Luise Hentschel
Christoph Heisler
Katharina Höfer
Carolin Jacobi
Robert Kockrick
Julius Jöhrens
Julian Kühnel
Michael Kozlik
Matthias Meissner

Steffen Milz
Martin Pollithy
Karsten Pottrick
Peter Queitzsch
Willen Rischau
Markus Schiffler
Stefan Schmidt
Ullrich Schröder
Susann Spindler
Florian Szillat
Marc Teichmann
Benjamin Voigt
Johannes Wagner
Franziska Walter (extern)
Jan Wernecke
Christian Wolf

Technical Staff

Ulrich Barth
Uta Bornkessel
Uwe Eberhardt
Tobias Eißmann
Lutz Föllmer
Silke Frunzke
Torsten Hilprecht
Kristina Garlipp
Frank Jehn

Gerald Lenk
Holger Mühlig
Anja Mittelstädt
Ralf Neubert
Stefan Prass
Helga Rudolph
Sylvia Stender
Matthias Thürk
Carmen Voigt